

**Monte Carlo Modelling of Peripheral Dose and Risk of Secondary Malignancy in Flattening-
Filter-Free and 10 MV Photon Beams for Paediatric Radiotherapy**

by

Youssef Ben Bouchta

B.Sc., University of Ottawa, 2014

A THESIS SUBMITTED IN PARTIAL FULFILLMENT OF
THE REQUIREMENTS FOR THE DEGREE OF

Doctor of Philosophy

in

THE FACULTY OF GRADUATE AND POSTDOCTORAL STUDIES
(Physics)

THE UNIVERSITY OF BRITISH COLUMBIA
(Vancouver)

July 2019

© Youssef Ben Bouchta, 2019

The following individuals certify that they have read, and recommend to the Faculty of Graduate and Postdoctoral Studies for acceptance, the dissertation entitled:

Monte Carlo Modelling of Peripheral Dose and Risk of Secondary Malignancy in Flattening-Filter-Free and 10 MV Photon Beams for Paediatric Radiotherapy

submitted by Youssef Ben Bouchta in partial fulfillment of the requirements for
the degree
of Doctor of Philosophy
in Physics

Examining Committee:

Dr. Alanah M. Bergman
Supervisor

Dr. Stefan Reinsberg
Supervisory Committee Member

Dr. Cheryl Duzenli
Supervisory Committee Member

Dr. Cornelia Laule
University Examiner

Dr. Arman Rahmim
University Examiner

Additional Supervisory Committee Members:

Dr. Alex Mackay
Supervisory Committee Member

Dr. Karen Goddard
Supervisory Committee Member

Abstract

One of the most serious late side effects of cancer treatments is the development of a second malignant neoplasm (SMN). While the risk of SMN is influenced by many factors, radiation therapy (RT) during childhood and adolescence has been shown to be one of the most significant factors associated with the development of a second cancer. The work presented in this thesis determines how to lower the risk of RT-induced SMN without affecting the quality and efficacy of RT treatments. To properly assess dose to the entire body in patients, a Monte Carlo and measurements based model was developed. This model was used to determine the dose delivered to a cohort of paediatric patients by three different photon radiotherapy treatment modes: 6MV flattened, 6MV flattening-filter-free (FFF) and 10MV FFF. To establish the clinical significance of the dose difference between the three modes, the risk of SMN as calculated by four different risk models was assessed for whole lung irradiation (WLI). The mixed Monte Carlo and measurements model was found to be accurate. The uncertainty in the dose was found to be below 9.4 % of the local dose. A comparison of the out-of-field dose delivered by the 6MV FFF and 10MV FFF beams relative to the 6MV flattened beam was presented. The data demonstrated dose reductions of 3.9% (95% CI[2.1, 5.7]) and 9.8% (95% CI[8.0, 11.6]) at 5 cm from the planning treatment volume (PTV) and 21.9% (95% CI[13.7, 30.1]) and 25.6% (95% CI[17.6, 33.6]) at 30 cm for 6MV FFF and 10 MV FFF beams respectively compared to the 6MV flattened beam. In paediatric patients who were treated with WLI, this dose reduction led to a reduction in the estimated risk of RT-induced thyroid cancers. This

reduction corresponds to risk ratio for radiation-induced thyroid cancer of <0.90 and <0.95 for 10 MV FFF and 6MV FFF respectively compared to the 6MV flattened beam. In conclusion, the work presented in this thesis provides evidence that FFF beams, specifically 10MV FFF beams, deliver lower out-of-field dose than 6MV flattened beams and lead to a lower risk of second malignancies.

Lay Summary

Radiation therapy is a type of cancer treatment that uses x-ray beams to kill cancer cells. It is used to treat almost half of all cancer patients. However, like all cancer treatments, radiation therapy can have dangerous side effects, including the development of an additional cancer many years after the treatment. Additional cancer can grow because during treatments, healthy tissues unavoidably get exposed to radiation from x-rays. For example, during treatment for lung cancer, the thyroid gland and breast tissues receive some radiation. My research examines how much radiation healthy tissues receive during radiation therapy. I compared different radiation therapy techniques and determined which one leads to the smallest amount of radiation in healthy tissues. My research shows that if the optimal radiation therapy technique is used, it is possible to reduce the risk of additional thyroid cancer caused by radiation therapy in some lung cancer treatments.

Preface

I was the only author of Chapter 1 and Chapter 2, which were written with the sole purpose of introducing the readers to various concepts necessary to the understanding of this thesis.

Figure 1-2, Figure 1-6, Figure 1-7 were first made for an assignment for the Radiation Dosimetry course taught by Drs. Tony Popescu and Cheryl Duzenli. Figure 1-10 was made with the permission of Dr. Tony Popescu using data provided by him in the context of the previously mentioned Radiation Dosimetry course. The measurement curves shown in Figure 2-3, Figure 2-4, Figure 2-5 and Figure 2-6 were made using data acquired by the medical physics team of BC Cancer – Vancouver during the commissioning of a Varian TrueBeam linear accelerator.

A version of the work presented in Chapter 3 and Chapter 4 was previously published as:

- Y. Ben Bouchta, K. Goddard, M. P. Petric and A. M. Bergman, "Effects of 10 MV and Flattening-Filter-Free Beams on Peripheral Dose in a Cohort of Pediatric Patients," *International Journal of Radiation Oncology • Biology • Physics*. Volume 102, Issue 5, 1560-1568 (2018)

I am the first author of this paper. I completed all of the analysis and the majority of the writing and data collection. Dr. Alanah M. Bergman provided guidance and helped during the data collection. Dr. M. Peter Petric provided guidance on neutron measurements and Dr. Karen Goddard provided guidance on clinical aspects. The work presented in Chapter 5 was done with the guidance of Dr Alanah Bergman. I completed all of the analysis, writing and data collection. Drs. Karen Goddard and Andrea Lo provided guidance on the clinical aspects of the work and Dr. Andrea Lo provided training and supervision for OAR contours.

The work presented in Chapter 3, Chapter 4 and Chapter 5 received approval from the UBC BCCA REB under the title: *Peripheral (out-of-field) Dose Reduction Strategies for Paediatric Radiation Therapy: A Planning Study* and certificate H13-01632.

Table of Contents

Abstract	iii
Lay Summary.....	v
Preface.....	vi
Table of Contents	viii
List of Tables	xii
List of Figures	xiv
List of Abbreviations.....	xix
Acknowledgements	xxi
Chapter 1 Introduction	1
1.1 Thesis Overview	1
1.2 The Interactions of Ionizing Radiation with Matter.....	3
1.2.1 Dosimetric Quantities and Dose Deposition.....	3
1.2.2 The Interaction of Charged Particles with Matter	5
1.2.3 The Interaction of Photons with Matter.....	6
1.2.3.1 Compton and Rayleigh Scattering	6
1.2.3.2 The Photoelectric Effect.....	9
1.2.3.3 Pair and Triplet Production	11
1.2.3.4 Photon Attenuation	13

1.3	Medical Linear Accelerators and X-Ray Generation	16
1.4	Radiotherapy Techniques	20
1.4.1	3-Dimensional Conformal Radiotherapy	20
1.4.2	Intensity Modulated Techniques	21
1.4.2.1	Treatment Planning	22
1.4.2.2	Intensity Modulated Radiation Therapy	25
1.4.2.3	Volumetric Modulated Arc Therapy	25
1.5	Radiation Biology	26
1.5.1	Linear Energy Transfer	28
1.5.2	Fractionation and the 4 “R” of Radiotherapy	28
1.6	Peripheral Dose.....	30
1.6.1	Peripheral Photon Dose	31
1.6.1.1	Effects of Flattening-Filter-Free Beams on Peripheral Photon Dose.....	32
1.6.1.2	Effects of Increasing Beam Energy on Peripheral Photon Doses	33
1.6.2	Neutron Doses	34
Chapter 2 Monte Carlo Simulations and Dose Modeling.....		36
2.1	The Monte Carlo Method	36
2.2	Monte Carlo for Radiation Transport	38
2.3	The BC Cancer – Vancouver’s EGSnrc Monte Carlo Model	42
2.3.1	Benchmarking of the Monte Carlo Code	44
Chapter 3 Combined Monte Carlo and Measurement Model for Peripheral Dose Calculation		49

3.1	Introduction	49
3.2	Methods and Materials.....	49
3.2.1	Measurement of the Head-Scatter and Leakage Correction.....	50
3.3	Results and Discussion	53
3.4	Conclusion.....	55

Chapter 4 Effects of 10 MV and Flattening-Filter-Free Beams on Peripheral Dose in Paediatric

Patients.....	56	
4.1	Introduction	56
4.2	Methods and Materials.....	57
4.2.1	Patient Selection and Planning	57
4.2.2	Dose Analysis	59
4.2.2.1	Creation of Isodistant Dose Shells	59
4.2.2.2	Integral Relative Dose	61
4.2.3	Neutron Measurements	62
4.3	Results.....	63
4.3.1	Relative Photon Peripheral doses for FFF beams	63
4.3.1.1	Dose-Distance Relationship	63
4.3.1.2	Clinical Factors affecting Integral Relative Dose.....	67
4.3.2	Neutron Doses	68
4.4	Discussion.....	69
4.5	Conclusion.....	72

Chapter 5 Reducing the Thyroid and Breast Dose during Whole Lung Irradiation Using

Flattening-Filter-Free Beams	73
5.1 Introduction	73
5.2 Methods and Materials.....	74
5.2.1 Treatment Planning and Dose Assessment	74
5.2.2 Secondary Cancer Risk	76
5.3 Results.....	78
5.3.1 Thyroid Dose and Risk of Secondary Malignancy	78
5.3.2 Breast Dose and Risk of Secondary Malignancy	81
5.4 Discussion.....	84
5.5 Conclusion.....	86
Chapter 6 Conclusion and Future Work	88
6.1 Conclusion.....	88
6.2 Future Work	91
References	93

List of Tables

Table 3-1 Longitudinal and lateral distance from isocenter of each measurement point shown in Figure 3-1	52
Table 4-1 Number of plans per treatment site, mean prescription dose, and PTV volume in paediatric cohort.....	58
Table 4-2 Significance of association between several clinical factors and IRD.....	67
Table 5-1 List of OAR and PTV dose constraints used for the VMAT optimization. All dose constraints are given in either percent of prescribed dose or in Gy. * The dose to the thyroid was lowered as much as possible without compromising other optimization objectives.....	75
Table 5-2 Values of parameters used for the breasts and thyroid second cancer model.	78
Table 5-3 List of various thyroid specific dosimetric quantities averaged over 10 patients for each beam modality. Red bolded quantities are significantly ($p < 0.05$) different than their 6 MV flattened equivalent.....	80
Table 5-4 Calculated thyroid OED in Gy for the full model (OED_F) (Eq. 5-1), bell shaped model (OED_BS) (Eq. 5-2) and plateau model (OED_P) (Eq. 5-3) for all patients and all modalities.....	80
Table 5-5 Calculated thyroid cancer risk ratios for all patients according to 4 risk models models: The linear model where $OED = D_{mean}$, the full model (Eq.5-1), the bell shaped model (Eq. 5-2) and the plateau model (Eq. 5-3). The error on the mean represents the 95% CI as calculated by a Student t-test.	81

Table 5-6 List of various breast-specific dosimetric quantities for all four female patients who were planned with WLI in this study. The mean doses are given in cGy and the volumes in % of total volume 83

Table 5-7 Calculated breast OED in Gy for the full model (Eq. 5-1), bell shaped model (Eq. 5-2) and plateau model (Eq. 5-3) for all patients and all modalities. 83

Table 5-8 Calculated breast cancer risk ratios for all patients according to 4 risk models models: The linear model where $OED = D_{mean}$, the full model (Eq.5-1), the bell shaped model (Eq. 5-2) and the plateau model (Eq. 5-3). 84

List of Figures

Figure 1-1 Diagram representing Compton scattering. The incident photon interacts with a bound electron. Part of the incident photon energy is given to the electron and the rest to the scattered photon. 7

Figure 1-2 Probability that a Compton photon will scatter at a certain angle as a function of energy of the incident photon. The data was obtained by doing a Monte Carlo sampling of the Klein-Nishina cross section. Each curve have been normalized to meet the normalization condition for probability distributions..... 8

Figure 1-3 Diagram representing the photoelectric effect. The incident photon interacts with an electron from an electronic shell. The electron is freed and given kinetic energy E_{elec} and a vacancy is left in the electron shell it just vacated. 9

Figure 1-4 Diagram representing how a vacancy can be filled with the extra energy released in the form of a) a characteristic photon or b) an Auger electron. 10

Figure 1-5 Diagram representing the pair production process. A photon annihilates in the vicinity of a nucleus which results in the creation of an electron (in blue) and a positron (red). 12

Figure 1-6 Graph of the absolute mass attenuation coefficient of water as a function energy. Interaction specific mass attenuation coefficient for Rayleigh scattering, Compton scattering, photoelectric interactions and pair production are also shown. 15

Figure 1-7: Graph of the interaction specific relative mass attenuation coefficient of water as a function of energy for Rayleigh scattering, Compton scattering, photoelectric interactions and pair production. 15

Figure 1-8 Photograph of a Varian TrueBeam linac at BC Cancer Vancouver. The couch, gantry and treatment head are marked. 16

Figure 1-9 Schematic of the principal beam shaping components of a Varian TrueBeam linac. The path of the electron beam is shown by an arrow from when they are emitted by the electron gun to when they hit the target and the photon beam is created. 17

Figure 1-10 6 MV photon spectrum from a linac normalized to set the integral of the curve shown above to 100%..... 18

Figure 1-11 Dose Profiles at 10 cm depth for a 6 MV photon beam with (a) and without (b) the flattening filter 19

Figure 1-12 Representation of the MLC (blue rectangles) shaping the beam opening to match the field size to the 2D projection of the tumor (in red). 21

Figure 1-13 Image of the target (left) and the corresponding dose distribution (right) that can be obtained using intensity modulation..... 21

Figure 1-14 Illustration of OAR and PTV contours on 1 axial slice (left) and a reconstruction of the contour in 3D (right) 22

Figure 1-15 Illustration of the three different level of target contours. The GTV is shown in green, the CTV in blue and the PTV in red..... 23

Figure 1-16 Ideal (a) DVH and realistic (b) DVH for a plan with a single PTV and OAR. The curve in green is the DVH for the OAR and the curve in red is for the PTV. It should be noted that the axes' origin are shifted from 0 to better show the curves in (a). 24

Figure 1-17 Cell survival curve for a fractionated treatment (red) and a single fraction treatment (black) illustrating the effect of repair on cell survival..... 29

Figure 1-18 Illustrations of a treatment head showing the origin or the different component of peripheral dose 32

Figure 2-1 Representation of a square inscribed inside a square. Each dot was found from a uniform 2D distribution and the ratio of the number of dot in the circle to the total number of dot can be used to determine the value of Pi. 38

Figure 2-2 Representation of a linac head showing the position of the two phase-spaces used during a MC simulation. The phase-space provided by Varian is shown in blue and the phase-space outputted by BEAMnrc is shown in red..... 43

Figure 2-3 Comparison between measured (red) and MC calculated (black) PDD curves for a 10x10 field..... 45

Figure 2-4 Crossline (a) and inline (b) profile of a 10x10 6 MV flattened beam at depth of 1.5 cm 45

Figure 2-5 Crossline (a) and inline (b) profile of a 10x10 6 MV FFF beam at depth of 1.5 cm 46

Figure 2-6 Crossline (a) and inline (b) profile of a 10x10 10 MV FFF beam at depth of 2.5 cm ... 46

Figure 2-7 Comparison of Eclipse Calculated DVH (solid line) with the MC calculated DVH (dashed line) for a paediatric patient. Three OARs (heart, liver and kidney) and a PTV are shown. 48

Figure 2-8 Axial slice comparing the Eclipse calculated dose distribution (left) with the MC calculated dose distribution (right)..... 48

Figure 3-1 Top-view coronal (a) and an end-on axial (b) plane of the phantom showing the points of measurements and the position of the isocenter. 51

Figure 3-2 Uncorrected (solid line) and corrected MC (dashed line) dose profile along the longitudinal axis of the patient relative to the measured dose for three validation plans (a), (b), (c). Uncertainty was <3% for all points MC calculated points. 53

Figure 4-1 Illustration of the first 5 shells expanded around the PTV. The legends indicate the distance from the PTV of voxel within each shells and identifies the PTV..... 60

Figure 4-2 Dose as a function of distance from the PTV edge for a patient receiving 6 MV-flattened thoracic irradiation. Angle positions relative to the patient’s body are shown in the diagram next to the legend. Uncertainty was <3% for all MC calculated points. 64

Figure 4-3 Uncorrected MC (a) and “leakage”-corrected MC (b) population mean peripheral dose as a function of radial distance from PTV edge determined by using concentric shells. 10 MV FFF (solid line) and 6 MV FFF (dotted line) beam relative to the 6 MV-flattened beam (horizontal dashed line) are shown. 65

Figure 4-4 “Leakage”-Corrected MC calculated absolute population mean peripheral dose in mGy per Gy of prescription dose from the 10 MV FFF (solid line), 6 MV FFF (dashed line) and 6

MV flattened (dotted line) dose as a function of distance from PTV edge. Uncertainty was 0.5% close to the PTV edge and reaching a maximum of 8% at 30 cm from the PTV edge. The error bars are too small to show..... 66

Figure 4-5 Uncorrected MC (a) and “leakage”-corrected MC (b) population mean peripheral dose profile as a function of longitudinal distance from PTV edge. 10 MV FFF (solid line) and 6 MV FFF (dotted line) beam relative to the 6 MV-flattened beam (horizontal dashed line) are shown..... 66

Figure 4-6 Percent difference in integral relative dose between the two flattening-filter-free beams and the flattened beam for all patients. 10 MV FFF is shown in red and 6 MV FFF is shown in black. Square, triangle and circle markers show treatments to the abdominal, thoracic and head & neck region respectively..... 68

Figure 5-1 Axial (left) and coronal (right) CT slice of a female patient showing patients showing the different contours : PTV (red), breast (light blue), heart (magenta) and thyroid (lavender) 75

Figure 5-2 MC calculated thyroid DVH averaged over 10 patients for 6 MV Flattened, 6 MV FFF and 10 MV FFF beam energies. The shaded area shows the spread of DVHs in our datasets from the 25th percentile to the 75th percentile. 79

Figure 5-3 Breast DVH for all four female patients. The green dashed curve shows the 6 MV flattened DVH, the blue dotted curve shows the 6 MV FFF DVH and the red solid curve shows the 10 MV FFF DVH. An axial CT slice is also shown for each patient. 82

List of Abbreviations

3DCRT	3-Dimensional Conformal Radiotherapy
AAA	Analytical Anisotropic Algorithm
AAPM	American Association of Physicists in Medicine
CI	Confidence Interval
CSDA	Continuously Slowing Down Approximation
CT	Computed Tomography
CTV	Clinical Target Volume
dmax	Depth of Maximum Dose
DVH	Dose Volume Histogram
EAR	Excess Absolute Risk
EGSnrc	Electron Gamma Shower- National Research Council
ERR	Excess Relative Risk
EW	Ewing Sarcoma
FF	Flattening Filter
FFF	Flattening-Filter-Free
GTV	Gross Tumor Volume
HDMLC	High Definition Multi-Leaf Collimator
IMRT	Intensity Modulated Radiation Therapy
IRD	Integral Relative Dose

Linac	Medical Linear Accelerator
MC	Monte Carlo
MLC	Multi-Leaf Collimator
MST	Multiple Scattering Theory
MU	Monitor Unit
NTCP	Normal Tissue Complication Probability
OAR	Organ-at-Risk
PDD	Percent Depth Dose
PTV	Planning Target Volume
RBE	Radiobiological Effectiveness
SMN	Secondary Malignant Neoplasm
TCP	Tumor Control Probability
TG	Task Group
VMAT	Volumetric Modulated Arc Therapy
WLI	Whole Lung Irradiation

Acknowledgements

I would like to express my gratitude to Dr. Alanah M. Bergman, my research supervisor, for her support and guidance throughout my PhD. I admire her research acumen and her understanding of clinical research and of medical physics and I feel honored to have had the opportunity to learn from her. Dr. Bergman's generosity and kindness have made the PhD process enjoyable and helped me grow as a researcher and as a person.

I would also like to thank the members of my committee, Dr. Stefan Reinsberg, Dr. Alex Mackay, Dr. Cheryl Duzenli and Dr. Karen Goddard, for their advice and support throughout my PhD. Furthermore, I would like to acknowledge the entire medical physics team of BC Cancer – Vancouver for being willing to listen and provide feedback on my ideas.

Finally, I would like to acknowledge the support of my friends and family. Specifically, I want to acknowledge and thank my partner, whose support and encouragements have allowed me to stay focused and positive throughout the PhD process.

Chapter 1

Introduction

1.1 Thesis Overview

In a world with an ever-growing number of people surviving cancer, it is increasingly important to minimize the cost, both human and societal, of treatment-related long-term toxicity.

Radiotherapy is a medical procedure in which a dose of ionizing radiation is given to a patient to cure or manage the symptoms of an illness. In modern times, the main use of radiotherapy is to treat cancer patients, 50% of whom benefit from receiving radiotherapy treatments [1] [2]. The advent of advanced beam shaping and intensity-modulated photon therapies has allowed for increased radiation dose conformity to the area of the disease, and lowered risk of complication in healthy organs-at-risk (OARs) which may be adjacent to the tumor.

These new modalities have also increased the amount of healthy tissues exposed to low doses of radiation [3]. While these low doses are not associated with acute toxicities, the long-term consequences can be life-threatening and need to be addressed. Cancer survivors and especially childhood cancer survivors are at an increased risk for cardiovascular diseases, thyroid dysfunction, and second malignant neoplasms (SMN) [4] [5]. These complications are an ongoing and serious threat to cancer survivors. An analysis of the cause of death in a cohort of childhood cancer survivor has shown that SMNs are the second cause of death in that population, surpassed only by recurrences of the primary [6]. It is estimated that 1400 cases of

radiation-induced secondary cancers were diagnosed in 2007 in the United-Kingdom [7].

Because radiation therapy is often given in conjunction with chemotherapy, it can be quite difficult to make this type of estimate. As such, an estimate of the number of radiation-induced second cancer has not been published in more recent years.

There is a body of evidence suggesting that it is possible to reduce the amount of tissue exposed to low doses of radiation during radiotherapy. However, there is a lack of data regarding the magnitude of the effect in a population of paediatric patients treated with modern radiotherapy techniques. One major reason for this lack of evidence is that it is very difficult to accurately determine peripheral doses, the dose received by a patient in the low-dose areas away from the primary radiation treatment site. Clinically used commercial dose calculation systems are accurate in calculating the dose received by tissues in the treatment field, but are limited when calculating the dose received by the rest of the body [8] [9]. One possible way to obtain dosimetric data for the entire body is to use Monte Carlo (MC) dose calculation techniques, which are considered to be the gold standard in dose calculation algorithms. However, MC models that can accurately measure dose far from the treated area are computationally intensive and require careful application.

The work presented in this thesis aims to determine which radiotherapy technique is associated with the lowest risk of late side effects by comparing patient-specific calculated and measured dosimetric data. In Chapter 3, a model combining MC with measured data is presented and

validated. This model uses measurements to correct the MC dose calculations in the far-field region in order to achieve accurate patient-specific dose distributions. Chapter 4 uses this model to calculate patient specific dose distributions for 26 paediatric patients. The dose distributions are then used to determine the effect of different radiotherapy techniques on the population mean peripheral dose.

Finally, Chapter 5 presents an in depth analysis of thyroid and breast doses and estimates the secondary cancer risk after whole lung irradiation (WLI). These risk factors are compared for the different treatment techniques studied in Chapter 4.

1.2 The Interactions of Ionizing Radiation with Matter

The main work of this thesis is the characterization of peripheral doses for various radiotherapy x-ray photon beams. A thorough understanding of how photon and particle radiation interacts with matter is helpful in understanding the work presented in this thesis. This section introduces various concepts regarding the interaction of radiation with matter that are referenced in subsequent chapters. Specifically, this section will cover how electrons and photons produced by medical linear accelerators (linacs) interact with matter.

1.2.1 Dosimetric Quantities and Dose Deposition

In radiotherapy, the physical quantity that is most commonly used to estimate the biological effects of radiation is absorbed dose – the amount of energy per unit of mass absorbed by a

medium. This section aims to provide the reader with an understanding of the physical process of dose deposition in radiotherapy.

Dose deposition is a two-step process. First, energy is transferred from incident particles to charged particles in the medium in the form of kinetic energy. The second step, in which energy is absorbed in the medium, occurs when charged particles exchange their kinetic energy to the medium in the form of heat or ionization. The physical quantity that measures the energy transferred during the first step is called the Kinetic Energy Released per unit Mass (KERMA) and is of little usefulness in estimating the biological effect of radiation. Energy absorption, which is the name given to the second step of the dose deposition process is of more interest to the study of the radiobiological effect of radiation. Energy absorption usually occurs over a series of events. On a microscopic level, energy absorption is measured by a quantity called the specific energy. The ICRU Report 85 [10] defines the specific energy z imparted in a volume V containing a mass m using Eq. 1-1 in which ε_i is the energy deposited in a single interaction and ε is the energy imparted. The specific energy can vary from irradiation to irradiation as it is a stochastic variable.

$$z = \frac{\varepsilon}{m}, \quad \varepsilon = \sum_i \varepsilon_i \quad 1-1$$

The more commonly used quantity to measure energy absorption is absorbed dose. It is defined for a volume dV containing a mass dm in equation Eq. 1-2 in which $d\bar{\varepsilon}$ is the mean energy imparted.

$$D = \frac{d\bar{\epsilon}}{dm}$$

1-2

The specifics of photons and charged particle interactions are discussed in further sections. However, it should be noted that photon interactions results in the deposition of KERMA and charged particle interactions results in the deposition of both KERMA and absorbed dose. For this reason, understanding how charged particles interact with matter is crucial to dose calculations.

1.2.2 The Interaction of Charged Particles with Matter

For simplicity, this section will focus on how electrons interact with matter, but the same principles can be generalized to most charged particle interactions. The main way in which electrons interact with matter is through the Coulomb force. Such interactions happen when an electron interacts with the electric field of an atom. While atoms are usually neutrally charged, they are made of a positively charged nucleus and negatively charged orbital electrons. As such, atoms are only neutral at sufficiently large distances. At closer distances, a non-zero electric field exists. An electron can interact with an atom in multiple ways. Some interactions take the form of a collision, either between traveling electron and nucleus or between traveling electron and orbital electrons. In others, energy is exchanged between the electric fields of travelling electrons and atoms.

Elastic collisions occur when the electron loses no energy. As a result of those collisions, the electron is deflected and the atom receives a negligible amount of energy in the form of recoil

kinetic energy. Inelastic collisions are of more interest to our understanding of energy deposition in matter. There are several types of inelastic collisions, but a common characteristic in all of them is that the travelling electron loses some of its energy. One such way is for electrons to impart energy to orbital electrons. If an orbital electron is given enough energy to break free of the atomic bond ($E > \text{binding energy}$) the atom will become ionized and the formerly bound electron will travel until all its energy has been deposited. These secondary electrons are called delta rays. It is also possible for primary electrons to interact with an atom's electric field and lose some of its energy. When this happens, a photon is emitted in the form of bremsstrahlung radiation (braking radiation).

1.2.3 The Interaction of Photons with Matter

In order to be able to predict dose distributions accurately with MC simulations, it is important to understand the intricacies of each individual type of photon interaction and how these processes affect a photon beam as it travels through a medium.

1.2.3.1 Compton and Rayleigh Scattering

Both Compton and Rayleigh scattering involve the scattering of an incident photon with an electron. The main difference between these two types of interactions is that in Compton scattering the incident photon transfers some of its energy to the electron whereas in Rayleigh scattering, the incident photon does not lose energy. Rayleigh scattering is a low probability interaction (for megavoltage energies) in which there is no energy transferred to electrons.

Since energy transfer and energy deposition are the main process of interest in understanding the biological effects of radiation, of this section will focus mainly on Compton scattering. Compton scattering is non-elastic scattering between a photon and an electron. The reason why the interaction is non-elastic is that some of the incident energy of the photon is lost. This energy loss comes from the transfer of energy from the incident photon to the electron. The remaining energy is carried by the scattered photon. The mechanics of Compton scattering can be seen in Figure 1-1. One of the main characteristics of the Compton interaction is that the binding energy of the electron is negligible compared to the energy of the incident photon. As such, the Compton interaction can be seen as occurring between a photon and a free electron (of mass m_e). The ratio between the scattered photon and incident photon's energy is derived by using the momentum and energy conservation laws and is shown in Eq. 1-3.

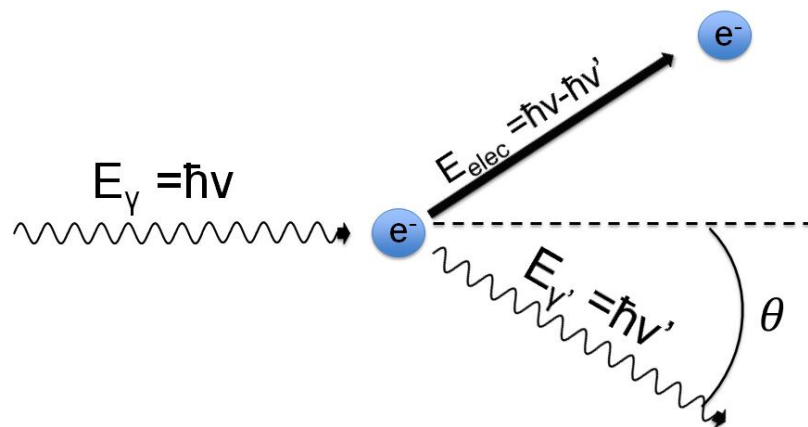


Figure 1-1 Diagram representing Compton scattering. The incident photon interacts with a bound electron. Part of the incident photon energy is given to the electron and the rest to the scattered photon.

$$E_{\gamma'} = \frac{E_{\gamma}}{1 + \left(\frac{E_{\gamma}}{m_e c^2}\right)(1 - \cos\theta)} \quad 1-3$$

Finally, the probability of interaction, and the energy and scattering angle of the scattered photon are given by the Klein-Nishina cross section $\left(\frac{d\sigma}{d\Omega}\right)$ shown in Eq. 1-4 in which r_e is the classical radius of the electron, E_{γ} is the energy of the incident photon and $E_{\gamma'}$ is the energy of the scattered photon. The probability of each scattering angle is shown in Figure 1-2 for incident photon energies ranging from 0 to 50 MeV.

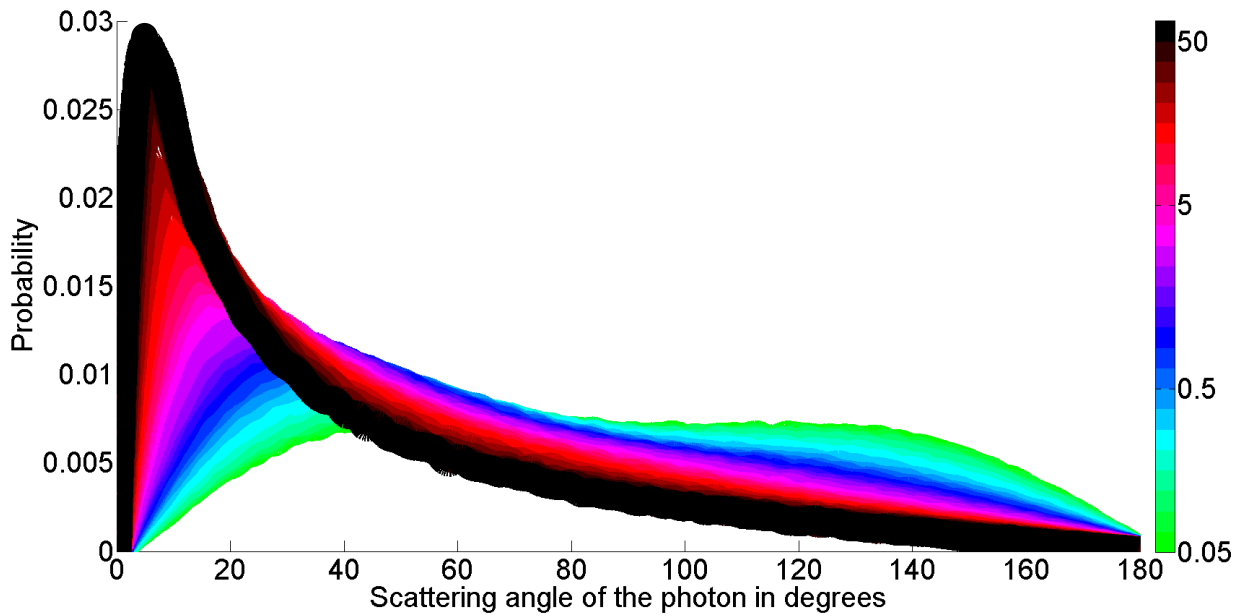


Figure 1-2 Probability that a Compton photon will scatter at a certain angle as a function of energy of the incident photon. The data was obtained by doing a Monte Carlo sampling of the Klein-Nishina cross section. Each curve have been normalized to meet the normalization condition for probability distributions.

$$\frac{d\sigma}{d\Omega} = \frac{r_e^2}{2} \left(\frac{E_{\gamma'}}{E_{\gamma}} \right)^2 \left(\frac{E_{\gamma'}}{E_{\gamma}} + \frac{E_{\gamma}}{E_{\gamma'}} - \sin^2 \theta \right) \quad 1-4$$

1.2.3.2 The Photoelectric Effect

The photoelectric effect is the name given to a phenomenon by which radiant energy (light) can free electrons from their atomic binding when shone on a material. The explanation for this phenomenon earned the 1921 Nobel Prize to a physicist now famous for his theory of gravitation, Albert Einstein. Like in all types of interactions, energy is conserved in the photoelectric effect. As a result, the initial kinetic energy of the freed electron is equal to that of the incident photon minus the electron atomic binding energy. A diagram of this initial interaction is shown in Figure 1-3.

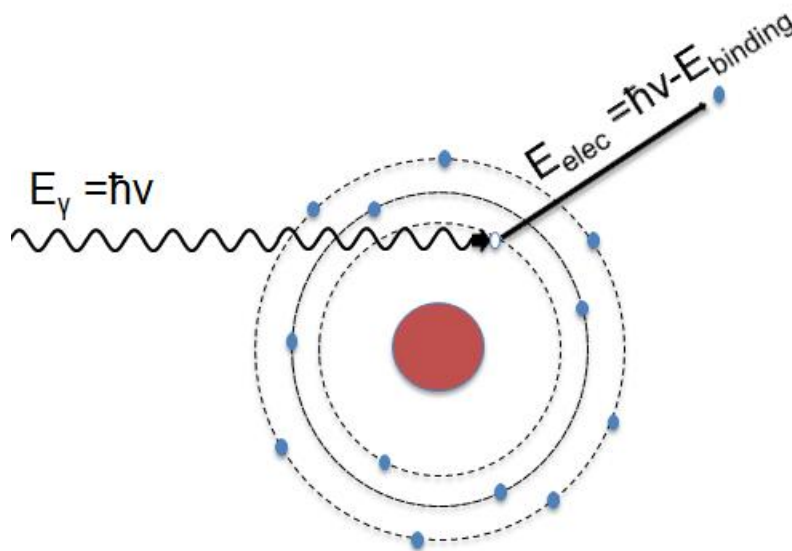


Figure 1-3 Diagram representing the photoelectric effect. The incident photon interacts with an electron from an electronic shell. The electron is freed and given kinetic energy E_{elec} and a vacancy is left in the electron shell it just vacated.

Because it is more energetically favorable to be in a lower energy shell, an electron from a higher energy shell will fill the vacancy left by the ejected electron. In order to do so, the electron filling the vacancies must release its extra energy. This occurs in one of two ways: A photon called a characteristic photon can be emitted or the energy can be given to an electron in which case that electron will also be ejected from the atom. Such electrons are called Auger electrons. It is also possible for the vacancy to be filled through a combination of both of these processes. A representation of each of these processes is shown in Figure 1-4.

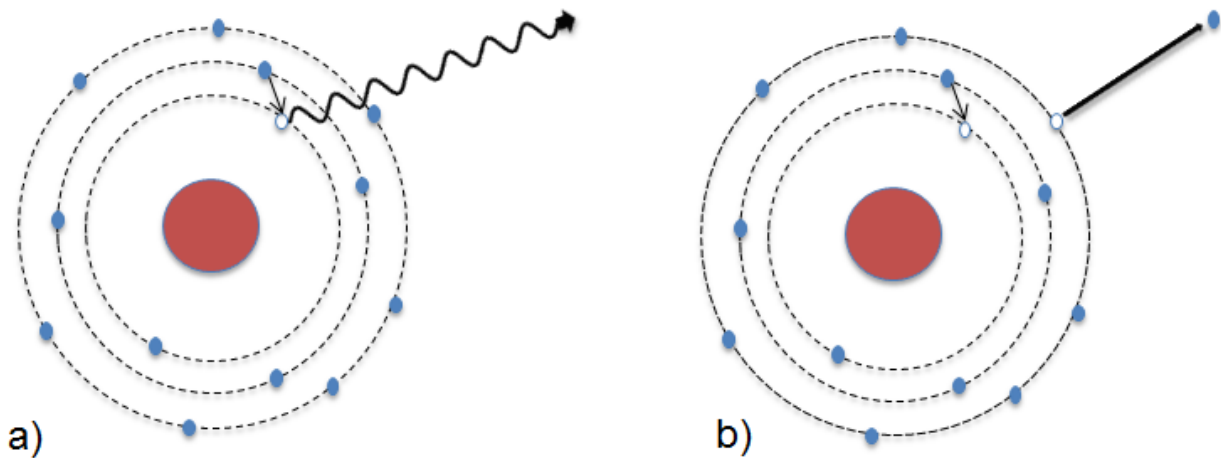


Figure 1-4 Diagram representing how a vacancy can be filled with the extra energy released in the form of a) a characteristic photon or b) an Auger electron.

The mean energy transferred to charged particles in photoelectric interactions can be expressed as the initial photon energy minus the energy lost to characteristic photons. This is shown in Eq. 1-5 where P_i is the probability that a photoelectric interaction occur in shell i , ω_i is

the yield of characteristic radiation emission and $\overline{(h\nu)}_i$ is the mean energy of the all possible characteristic radiation.

$$E_{tr} = h\nu - \sum P_i \omega_i \overline{(h\nu)}_i \quad 1-5$$

In x-ray beams produced by linear accelerators, the photoelectric effect is the primary endpoints of photons. In other words, the main factor causing a reduction in photon fluence when a photon beam travels through a patient is the number of photons lost through the photoelectric effect. While Compton scattering is the more common interaction in MV beams, it does not reduce the number of photons, just the mean photon energy. As a result, photons lose their energy through Compton interactions before ending their track by interacting through the photoelectric effect. This is showcased in Figure 1-7 where it can be seen that for photons in megavoltage beams, Compton scattering is the dominant process. However, as the photon energy decreases, the photoelectric effect starts competing with the Compton scattering and becomes the dominant interaction process as the incident photon's energy further decreases.

1.2.3.3 Pair and Triplet Production

Pair production occurs when an incident photon interacts with the electromagnetic field of an atomic nucleus and annihilates into a particle-antiparticle pair. For megavoltage beams used in photon radiotherapy, only electron-positron pairs are created due to the relatively low mean energy of these beams (1 – 18 MeV). This is due to the rest mass of the electron being 0.511

MeV, which is light compared to the rest mass of other common particles (the rest mass of a muon is in the order of 105.7 MeV and the rest mass of a proton is 938.3 MeV). In order for both the momentum and energy to be conserved simultaneously, this interaction can only occur in the vicinity of a 3rd particle that can carry some of the momentum. A representation of pair production is shown in Figure 1-5.

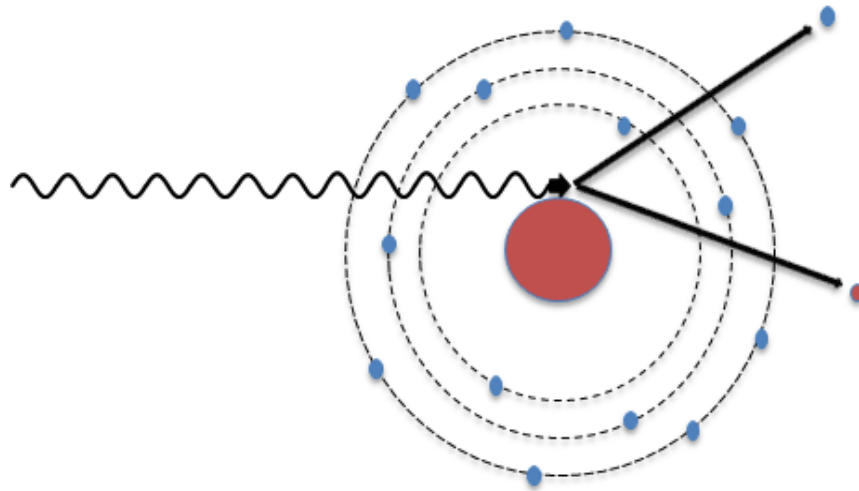


Figure 1-5 Diagram representing the pair production process. A photon annihilates in the vicinity of a nucleus which results in the creation of an electron (in blue) and a positron (red).

For energy to be conserved in pair production, the incident photon's energy must be slightly higher than twice the rest mass of an electron. The minimum energy necessary for a photon to interact through pair production is called the threshold energy and is given in Eq. 1-6, in which m_e is the rest mass of an electron/positron, M is the mass of the third particle mentioned above and c is the speed of light in vacuum.

$$E_{threshold} = \frac{2m_e c^2 (M + m_e)}{M} \quad 1-6$$

Triplet production, despite what its name implies, is not the creation an electron-positron triplet, as this would violate multiple conservation laws (charge conservation, lepton number conservation, etc.). Triplet production occurs when a photon interacts with the electromagnetic field of an electron and annihilates into a particle-antiparticle pair. When this occurs, a significant portion of the energy must be given to the perturbing electron in order to obey conservation law. That electron is freed from the atom it is bound to and ends up contributing to the dose deposition process. The threshold energy formula also holds true for triplet production. The main difference is that M , the variable representing the rest mass of the recoiled particle, is replaced by m_e , the rest mass of an electron. This allows the formula in Eq. 1-6 to be simplified to Eq. 1-7.

$$E_{threshold} = 4m_e c^2 \quad 1-7$$

1.2.3.4 Photon Attenuation

For any photon beam, the fraction of photons that will interact in an infinitesimal layer of matter is proportional to the thickness dx of the layer (Eq. 1-8). The coefficient of proportionality is called the total attenuation coefficient (μ). For larger layers, the proportion of photons interacting is given by Eq. 1-9 which is obtained by integrating Eq. 1-8. In both equations, N represents the number of photons, dN represents a change in the number of photon and N_0 represents the initial number of photons.

$$\frac{dN}{N} = -\mu dx \quad 1-8$$

$$\frac{N}{N_0} = e^{-\mu x} \quad 1-9$$

As a result of Eq. 1-9, it can be seen that the probability $P(x)$ that a photon travelling through a distance x in a medium will interact with that medium is given by Eq. 1-10 where ρ is the density of the medium and μ_p is the total mass attenuation coefficient, a characteristic property of the medium.

$$P(x) = 1 - e^{-\mu_p \rho x} \quad 1-10$$

The total mass attenuation coefficient is a sum of interaction-specific mass attenuation coefficients. This can be useful to determine the prevalence of a certain type of interactions. The interaction specific absolute mass attenuation coefficient of water as a function of photon energy is shown in absolute units in Figure 1-6. Figure 1-7 shows the proportion of interaction that are Compton scattering, Rayleigh scattering, photoelectric effect, and pair production as a function of photon energy. Photon beams used in linac-based radiotherapy have a mean energy of approximately 1.6 MeV for 6 MV and 2.6 MeV for 10 MV beams [11] [12]. As can be seen in Figure 1-7, Compton scattering is by far the dominant photon interaction at these energies.

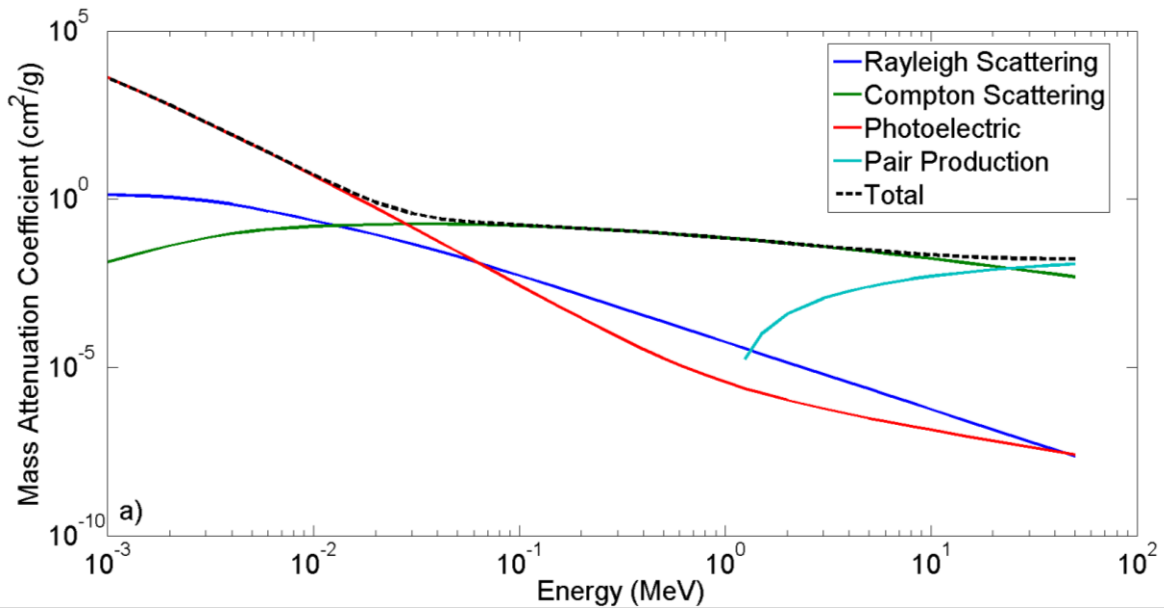


Figure 1-6 Graph of the absolute mass attenuation coefficient of water as a function energy. Interaction specific mass attenuation coefficient for Rayleigh scattering, Compton scattering, photoelectric interactions and pair production are also shown.

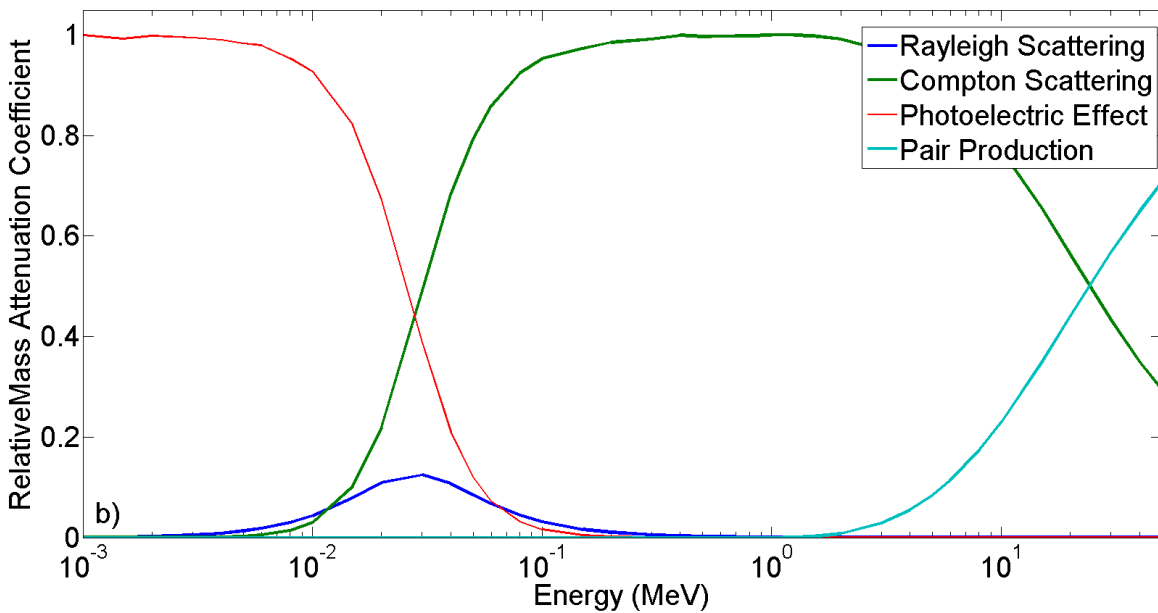


Figure 1-7: Graph of the interaction specific relative mass attenuation coefficient of water as a function of energy for Rayleigh scattering, Compton scattering, photoelectric interactions and pair production.

1.3 Medical Linear Accelerators and X-Ray Generation

The most commonly used instrument for delivering radiation in external beam radiotherapy is the linac, an example of which is shown in Figure 1-8. Linacs are small linear particle accelerators mounted on a rotating gantry. The purpose of the rotating gantry is to allow the linac to rotate in a full circle around the couch on which patients lie during treatment. There are two important axes for linear accelerators. The central beam axis runs parallel to the beam and perpendicular to the treatment head. This axis is also the axis of rotation of the secondary collimators and MLC. The second axis is the axis of rotation of the gantry. The point where both of these axes meet is called the isocenter. The treatment head, identified in Figure 1-8, contains attenuators and collimator which are used to shape the photon fluence produced by the linac. Figure 1-9 shows the schematic of the primary beam shaping components of a linac.

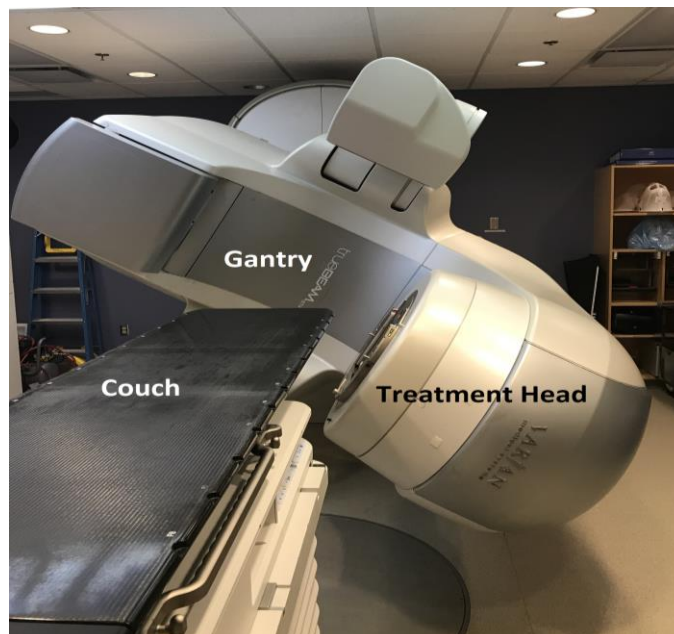


Figure 1-8 Photograph of a Varian TrueBeam linac at BC Cancer Vancouver. The couch, gantry and treatment head are marked.

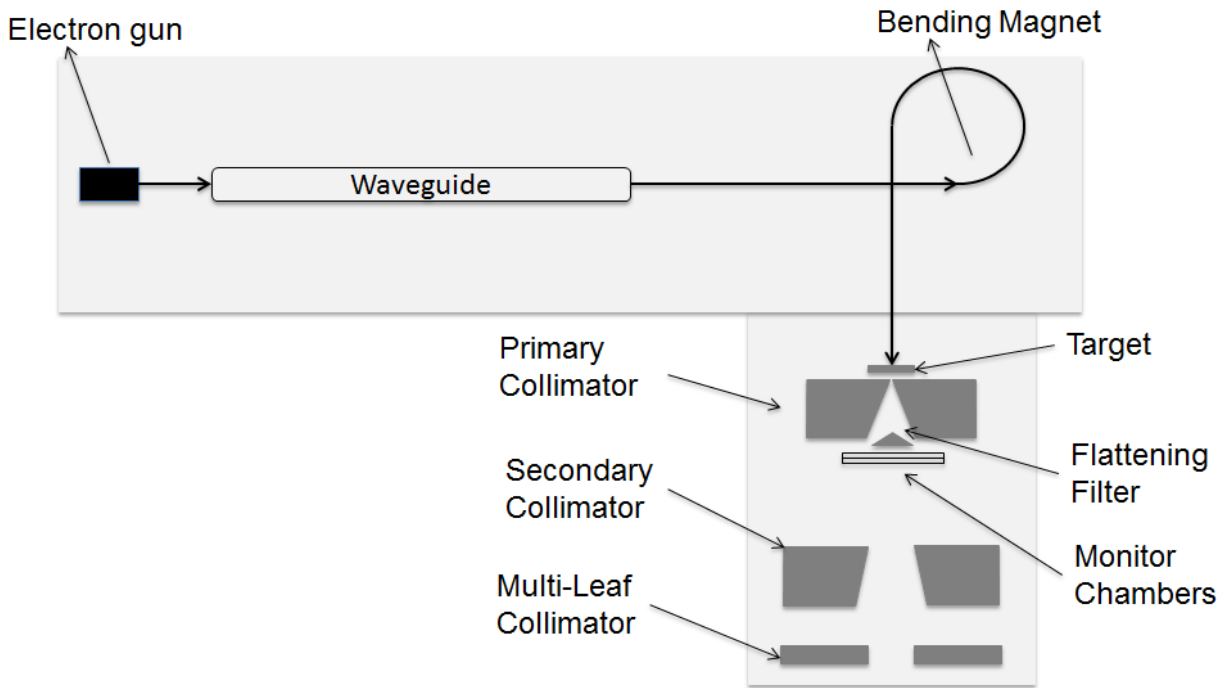


Figure 1-9 Schematic of the principal beam shaping components of a Varian TrueBeam linac. The path of the electron beam is shown by an arrow from when they are emitted by the electron gun to when they hit the target and the photon beam is created.

While linacs come in different shapes, they all operate in a similar fashion. Electrons are accelerated to the desired energy by a waveguide and then directed towards the gantry through the use of a bending magnet. The bending magnet also serves to further reduce the spread in electron energy. The most common accelerated electron energy used in radiotherapy is 6 MeV, but other energies can also be used (e.g. 4 MeV, 10 MeV, 18 MeV). When the electrons exit bending magnet, they collide with a target and megavoltage photons are emitted through bremsstrahlung radiation. Photon beams energies are often described in units of megavolts (MV). This refers to the magnitude of the electric potential accelerating the

electrons. This is more accurate than the term “MeV” which implies a mono-energetic beam. Photons beams generated through bremsstrahlung processes are not mono-energetic. The photon spectrum from a 6 MV photon beam is shown in Figure 1-10.

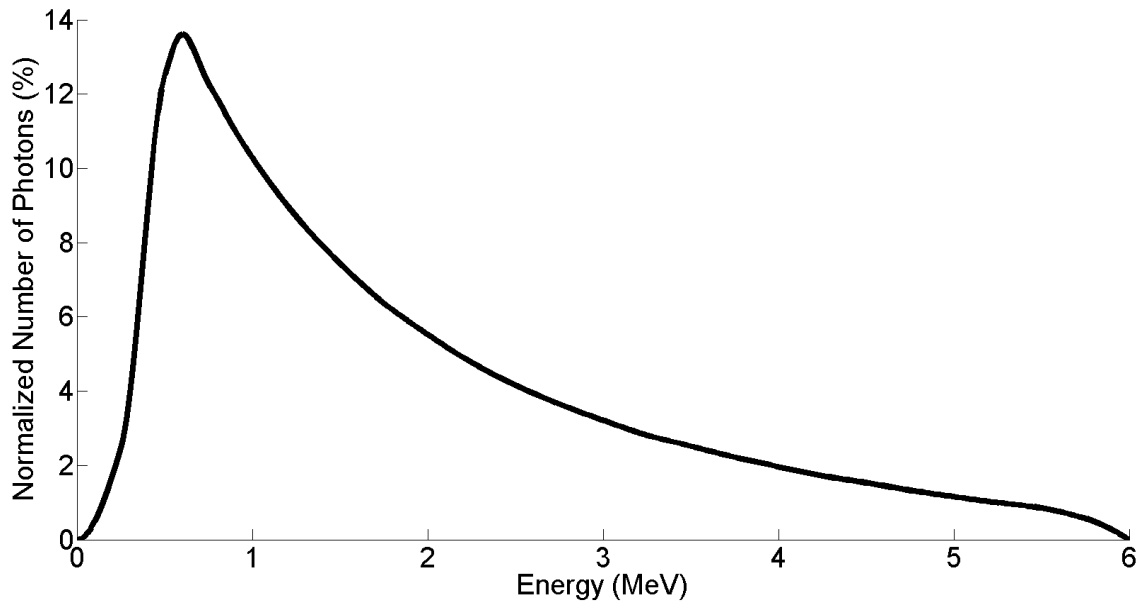


Figure 1-10 6 MV photon spectrum from a linac normalized to set the integral of the curve shown above to 100%

In medical linear accelerators, the photons are sent through a series of attenuators and collimators in order to shape the field and modulate the intensity for a specific treatment. The primary and secondary collimators are used to define size of the treatment field (Figure 1-9). The multi-leaf collimator (MLC) is used to shape the photon fluence inside the treatment field. Finally the flattening filter (FF) attenuates the middle of the beam to even out the fluence. This is needed to compensate for the forward-peaked fluence distribution coming off the target. The effect that the flattening filter has on the photon fluence (and therefore dose) is shown in Figure 1-11.

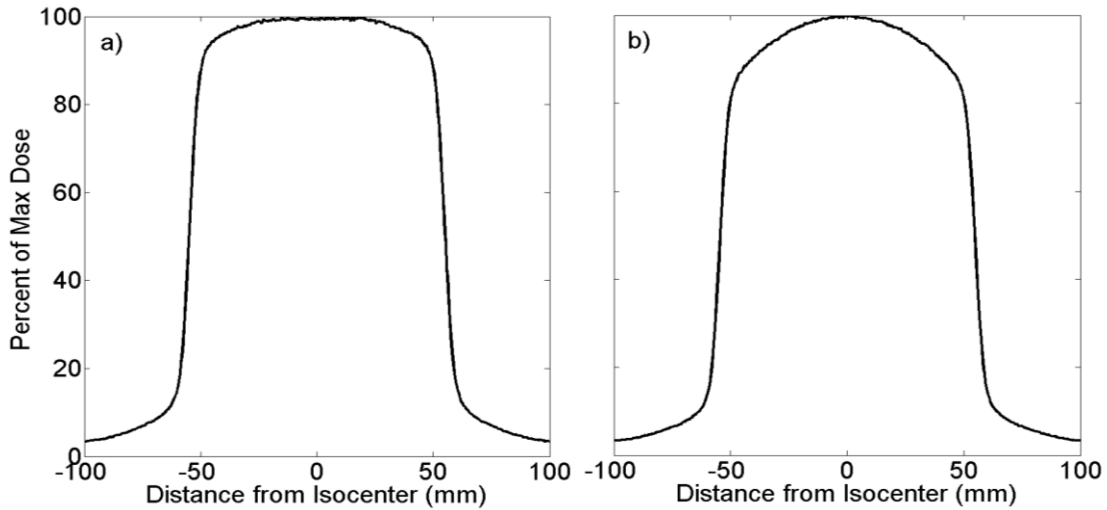


Figure 1-11 Dose Profiles at 10 cm depth for a 6 MV photon beam with (a) and without (b) the flattening filter

Dose monitor chambers are an important part of a linac. They are ion chambers that are used to measure the amount of radiation outputted by the linac. They are situated above the secondary collimator (Figure 1-9) and play a crucial role in controlling how much radiation the patient receives. They are responsible for shutting the beam off when the desired radiation output has been reached. Monitor chambers measure radiation in an arbitrary unit called the monitor unit (MU). To relate MU to dose in tissue, linacs are calibrated according to international radiotherapy protocols (for example, the protocols published by the American Association of Physicist in Medicine (AAPM) Task Group 51 (TG-51) [13]). The procedure established in the TG-51 report sets the calibration of linacs such that 1 MU is equal to 1 cGy at the calibration depth in medium and for the calibration field size. However, for real-life treatment situations, the radiotherapy process involves treatment geometries and additional attenuators that vary from the calibration condition such that $1\text{MU}=1\text{cGy}$ is not valid.

Correction factors are applied to the calibration condition to calculate the actual dose to patients. Dose at different depths and for different field sizes are found using factors that are measured during the linac commissioning process. Monitor units are correlated with the photon output of the x-ray target.

1.4 Radiotherapy Techniques

1.4.1 3-Dimensional Conformal Radiotherapy

In 3-dimensional Conformal Radiotherapy (3DCRT), an attenuator is used to shape the beam to the tumor. It is used to spare normal tissue that would otherwise be in the field defined by the secondary collimators. Figure 1-12 shows an example of a 3DCRT field for a spherically shaped tumor. The yellow square surrounding the tumor marks the edge of the field defined by the secondary collimators (or jaws) and the yellow circular shape marks the edge of the actual field, shaped to the tumor. In modern linacs, 3DCRT relies on the MLC to achieve this level of conformality. Most 3DCRT treatments make use of multiple beam angles to accumulate the required treatment dose to the tumor while sparing healthy tissues that would be exposed to high entry and exit dose if a single beam was used. The main advantage of static-field 3DCRT is its relative simplicity compared to more advanced techniques. However, its ability to spare healthy tissues adjacent to the tumor is limited for concave and irregularly shaped tumors.

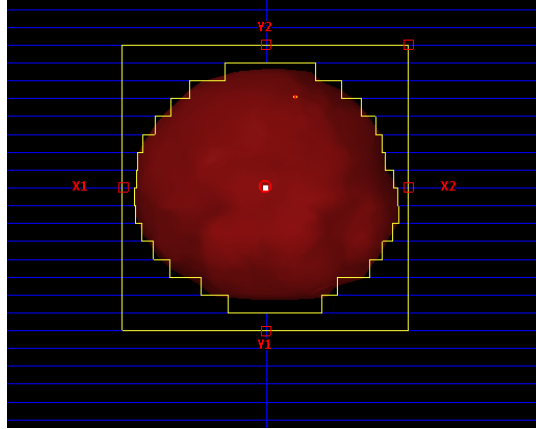


Figure 1-12 Representation of the MLC (blue rectangles) shaping the beam opening to match the field size to the 2D projection of the tumor (in red).

1.4.2 Intensity Modulated Techniques

What is meant by intensity modulation is the use of the MLC to preferentially attenuate the photon fluence to produce a non-uniform distribution across the treatment field. Intensity modulation in combination with the use of multiple beam angles allow for very conformal dose distributions. An example of a dose distribution from an intensity modulated technique is shown in Figure 1-13

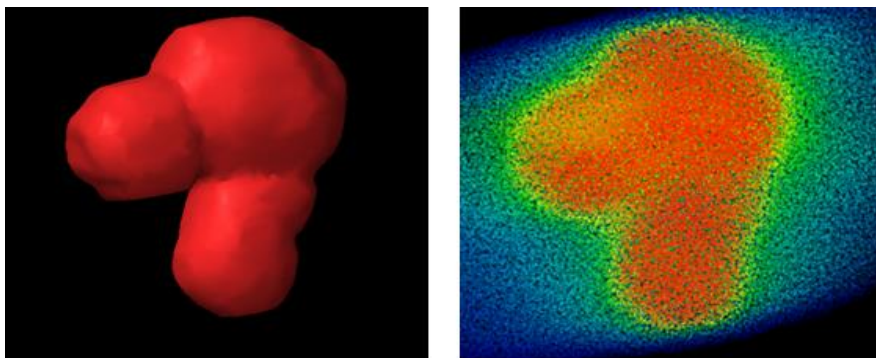


Figure 1-13 Image of the target (left) and the corresponding dose distribution (right) that can be obtained using intensity modulation.

1.4.2.1 Treatment Planning

In general, creating a radiotherapy treatment plan is done through a series of steps. First, the target and OARs are identified on a planning CT. This is done by a process called contouring or segmentation which consists of delineating each OAR and the Planning Target Volume (PTV) on every CT slice. Usually, only organs close to the target will be contoured as contouring is a time-consuming process. Figure 1-14 shows the OAR (all but red) and PTV (red) contours on one axial slice and a 3D reconstruction of those contours. The usual axial slice thickness is 2.5 mm which means that it isn't unusual for more than 50 slices to have to be contoured for a single patient. Contouring the target is usually done in several steps (Figure 1-15). First, the gross tumor volume (GTV) is defined. The GTV is the volume occupied by the tumor as can be determined by a physician through physical examination and diagnostic imaging.

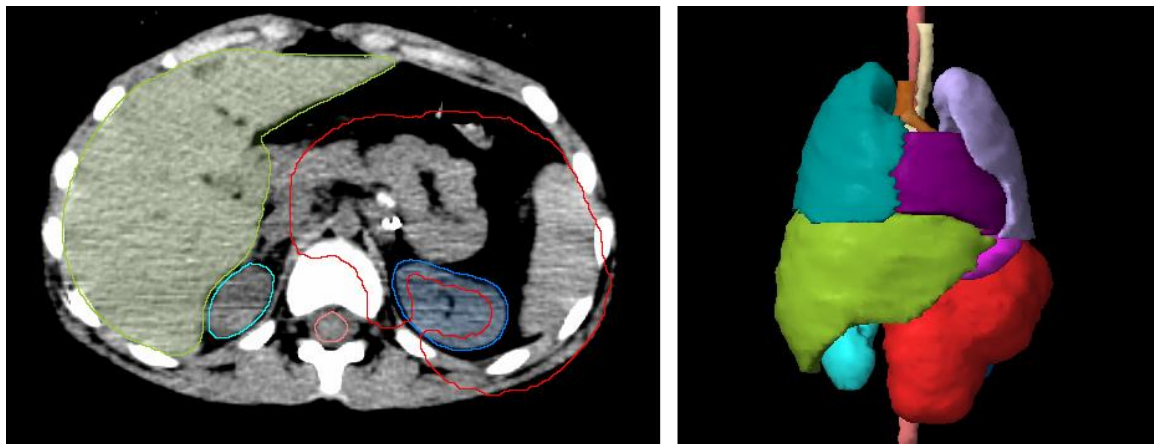


Figure 1-14 Illustration of OAR and PTV contours on 1 axial slice (left) and a reconstruction of the contour in 3D (right)

Once the GTV has been defined, an additional margin is added to it to account for microscopic growth (typically ~ 10 mm) that cannot be seen on scans or otherwise identified by a clinician. This secondary volume is called the clinical target volume (CTV). Finally, to account for uncertainty during the treatment planning and delivery (patient positioning, image registration, contouring, etc.), an additional margin is added to the CTV (typically, 3-7 mm). This final volume, which consists of the CTV plus that additional margin, is called the PTV [14]. The three different types of target contours are shown in Figure 1-15 on an axial slice.

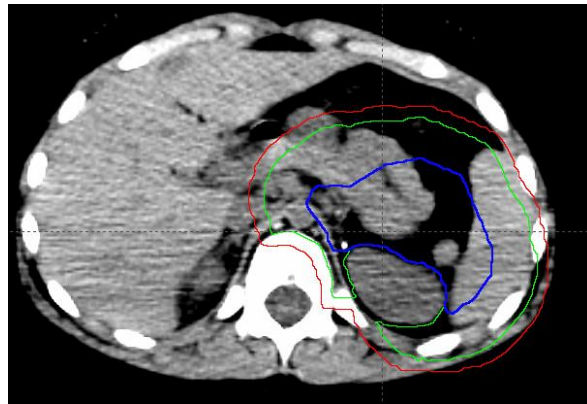


Figure 1-15 Illustration of the three different level of target contours. The GTV is shown in green, the CTV in blue and the PTV in red.

Once contouring is done, the treating physician will determine the clinical characteristics of the plan: prescribed radiation dose, fractionation schedule and OAR dose constraints or limits. These dose constraints are either given in the form of maximum doses, dose-volume constraints (e.g 30% of an organ must receive less than 20 Gy) or mean organ dose. Dose volume histograms (DVHs) are a type of graph useful to visually describe dose-volume data. The most common form of DVHs is cumulative DVHs, which plot the percentage of a structure

receiving at least a certain dose. An example of both an ideal and a realistic DVH with one OAR and one PTV is shown in Figure 1-16. Using these constraints a planner will then create a treatment plan that attempts to meet these planning goals.

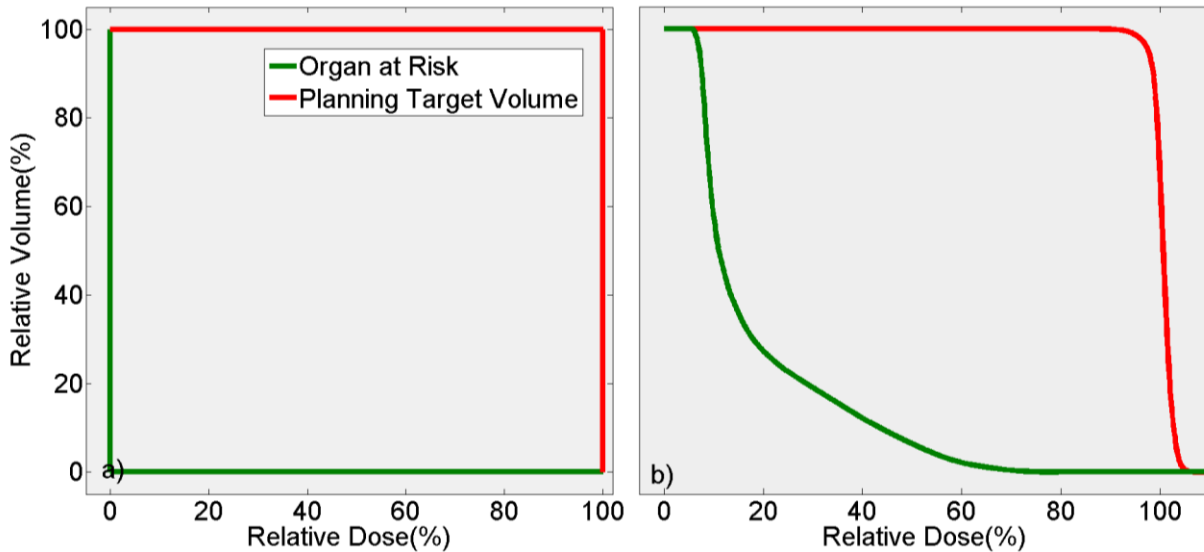


Figure 1-16 Ideal (a) DVH and realistic (b) DVH for a plan with a single PTV and OAR. The curve in green is the DVH for the OAR and the curve in red is for the PTV. It should be noted that the axes' origin are shifted from 0 to better show the curves in (a).

When treating with open fields or with 3DCRT, it is a lot easier for a planner to predict the dose distribution. This simplicity allows the planner to set up treatment fields first and then do small modifications of the fields until the dose distribution becomes acceptable. This process is called forward planning. In order to take full advantage of intensity modulation however, it becomes necessary to use inverse planning [15]. Inverse planning uses computer optimization strategies to create a non-intuitive and non-uniform photon beam fluence maps. When all the optimized fluence maps from all the treatment beams are combined together to form a dose distribution

in the patient, the plan should meet the physician prescribed dose constraints. The optimization process will iterate until all constraints are met or until no further improvement can be made.

1.4.2.2 Intensity Modulated Radiation Therapy

Static-field Intensity Modulated Radiation Therapy (IMRT) is the first modern intensity modulated technique. Like in 3DCRT, a few discrete gantry angles are selected (typically 5-7). However, instead of using the MLC to shape the photon beam around the tumor, the position of each leaf of the MLC is optimized in both time and space to deliver superbly conformal doses. While IMRT is much more conformal than 3DCRT [3], it can also require up to 3 times more MUs and therefore longer treatment times.

1.4.2.3 Volumetric Modulated Arc Therapy

Like static-field IMRT, Volumetric Modulated Arc Therapy (VMAT) is a type of intensity modulated technique. It is the intensity modulation technique that is currently used at BC Cancer – Vancouver, where the research presented in this thesis has been conducted. VMAT differs from IMRT in that instead of delivering radiation at static discrete gantry angles, it delivers the radiation while the gantry is moving in a continuous arc around the patient. VMAT uses a different optimization algorithm (direct aperture) compared to the static-field IMRT technique that is clinically available at BC Cancer – Vancouver. This allows for a reduction in the number of MUs used by a factor of 2 compared to static-field IMRT, but still requires more MUs than 3DCRT [3].

1.5 Radiation Biology

The effect of ionizing radiation on human tissues is an open field of research. At first glance, it can be tempting to assume that radiation damage is caused by the transfer of energy from the radiation beam to the tissues. However, the median lethal dose for humans is approximately 4.5 Gy (of x-ray dose to the entire body). This lethal dose converts into an absorbed energy of 4.5 J/kg, which is equivalent to an increase in temperature of approximately 0.001 Celsius. If you have ever been to a sauna, you know that the human body can easily absorb this amount of energy without complications. It is therefore evident that there must be an underlying mechanism making ionizing radiation into something dangerous to human tissues.

The reason for the lethality of ionizing radiation is its ability to damage the cells' deoxyribonucleic acids (DNA). This damage, if not repaired, prevents cells from reproducing. DNA damage from radiation comes in two ways: direct and indirect action. Direct action occurs when radiation causes damage by interacting directly with the molecules in the DNA structure. Indirect action occurs when radiation ionizes molecules in the cell (usually water) which leads to the creation of free radicals such as hydroxide (OH^-) and hydrogen (H^+) that have a damaging effect on the DNA. These free radicals can also impede the DNA repair processes, thus further increasing the lethality of ionizing radiation to human cells. There are three types of DNA damage that can result from exposure to ionizing radiation: base pair damage, single strand breaks (SSB) and double strand breaks (DSB). Base pair damage occurs when radiation damages

a DNA base pair, SSB occurs when radiation damages one strand of the phosphate backbone and DSB occurs when both sides of the phosphate backbone are damaged. Base pair damage and SSB are easily repaired by cells and do not usually lead to cell death or chromosomal aberrations. However, DSB can be hard to repair, especially if the two breaks are in close proximity. While it is possible for DSB to be repaired, lasting damage can occur even after successful repair. It is possible for cells to be viable even if an error in repair or a mutation occurs during the repair process. Such errors or mutations can evolve to become a cancer.

$$F(D) = e^{-(\alpha D + \beta D^2)} \quad 1-11$$

The fraction of cells in a given population that survive after receiving a dose D is given by Eq. 1-11. When plotted, the curve parameterised by Eq 1-11 is called a cell survival curve. Since cell survival curves depend on the specific cell population, tumors and normal tissues often respond differently to the same amount of radiation. This can sometimes be used to increase the therapeutic ratio of a treatment. The therapeutic ratio is the ratio between the tumor control probability (TCP) and the normal tissue complication probability (NTCP). A major goal in radiotherapy is to maximize the therapeutic ratio. Optimally, the NTCP would be 0 and the TCP would be 100. The main ways used in radiotherapy to keep the therapeutic ratio high is to deliver highly conformal doses to the tumour whilst sparing the nearby healthy OARs. A selective choice in radiotherapy dose fractionation schedule can also help.

1.5.1 Linear Energy Transfer

As mentioned previously, the mechanism that makes ionizing radiation lethal to human cells is not the transfer of energy but the ionizing potential of the radiation. The amount of damage caused by radiation depends on the type of radiation received. The linear energy transfer (LET) is a measure of transferred energy density along an ionizing particle's track. High LET radiation is more dangerous to cells than low LET radiation because the probability that several DSBs occur in a single cell is higher with high LET radiation. A factor called the radiobiological effectiveness (RBE) can be used to compare doses delivered by particles with different LET. Protons, alpha particles and neutrons are examples of high LET particles while photons and electrons are example of low LET particles.

1.5.2 Fractionation and the 4 "R" of Radiotherapy

Fractionation is the process of splitting a total dose of radiation into several smaller fractions. The four "R" of radiobiology [16] which are listed below explain the mechanism behind how fractionation affects radiotherapy treatments.

- Repair
- Redistribution
- Reoxygenation
- Repopulation

Repair is the mechanism by which cells repair. It can take up to a few hours for cells to repair non-lethal damage. If a cell receives a new dose of radiation before completing repairs, it will be more susceptible to radiation damage than when it was first irradiated. To allow for cell

repair in between fractions, radiotherapy treatments are usually scheduled so that patients receive at most one fraction per day. Figure 1-17 shows how repair and fractionation affect the cell survival curve.

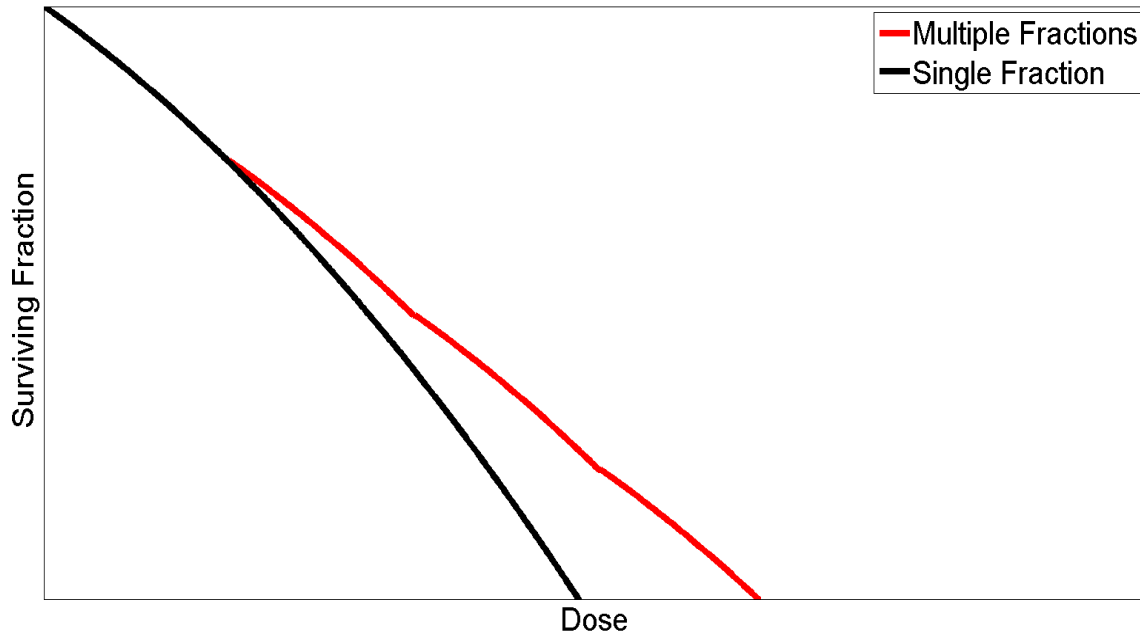


Figure 1-17 Cell survival curve for a fractionated treatment (red) and a single fraction treatment (black) illustrating the effect of repair on cell survival

Redistribution refers to the redistribution of cells along the cell cycle. There are several phases to the life cycle of a cell and its susceptibility to radiation damage varies depending on the phase. In particular, cells in the S phase of the cell cycle are very radioresistant to damage. In radiotherapy, it is crucial that all tumor cells be killed as even a single surviving cell has the ability to reproduce and can lead to recurrence of the cancer. Fractionating the dose allows cells that were in radioresistant phases to move to less radioresistant phases and therefore maximizes the probability that all tumor cells will die.

Reoxygenation is something that occurs after part of a tumor is killed. Tumors sometimes grow in a way such that parts of the tumor are not properly oxygenated by the blood supply. When this occurs, the parts of the tumor that are poorly oxygenated are called hypoxic. It has been shown that hypoxic cells are more radioresistant to damage than oxygenated cells [17]. When starting a fractionated radiotherapy schedule, the parts of the tumor that were well oxygenated will be preferentially killed. As the tumor shrinks, oxygen reaches cells that were previously hypoxic. These newly oxygenated regions of the tumor are then less likely to survive the next dose of radiation. Because it is rare for normal tissue to be hypoxic, reoxygenation is something that increases TCP and doesn't affect NTCP therefore increasing the therapeutic ratio.

The last "R" of radiobiology is repopulation. It refers to an effect that occurs when a large number of cells die. When this occurs, the rate of cell reproduction increases in order to replenish the lost population. For radiotherapy to be effective, it is important that all radiation be given before cancer cells start to repopulate. Repopulation puts a hard limit of about 6 to 8 weeks to finish a course of radiotherapy.

1.6 Peripheral Dose

Peripheral dose is the dose delivered outside of the treatment volume. Describing how different radiotherapy delivery methods affect peripheral doses is a complex subject as each change in delivery technique can sometimes create opposing changes in different components

of the peripheral doses. This section aims at providing a brief background on work done to characterize peripheral dose prior to the work presented in this thesis. For simplicity, peripheral photon doses and peripheral neutron doses will be discussed in separate sections.

1.6.1 Peripheral Photon Dose

Peripheral photon dose can be divided into 3 components: Head leakage, collimator scatter and patient scatter. Head leakage is defined as any photons that exit the linac without passing through the opening of the MLC (which defines the primary treatment beam). While this definition technically encompasses MLC leakage, it is more accurately treated as contributing to both the primary beam and collimator scatter component. Collimator scatter is defined as any photons that pass through the opening of the MLC but do not strike the target within the primary field. Patient scatter is defined as all scattered photons originating from the interaction of primary photons with the patient. A major benefit of using the above classification is that it allows for better understanding of the effects a change in treatment method can have on peripheral dose. .

A reduction in the overall number of photons produced would reduce the peripheral dose from head leakage and collimator scatter. This can be done by reducing the number of MUs delivered. A reduction in the fraction of photons scattered in the treatment head would also lead to a lower leakage and scatter dose. This can be done by reducing the amount of attenuating material present in the treatment head. Finally, it is possible to reduce patient

scatter by minimizing the distance travelled by photons in the patient. This can be done by modifying the quality of the emitted radiation. This section will present how these changes can be implemented in practice and their effects on peripheral photon dose.

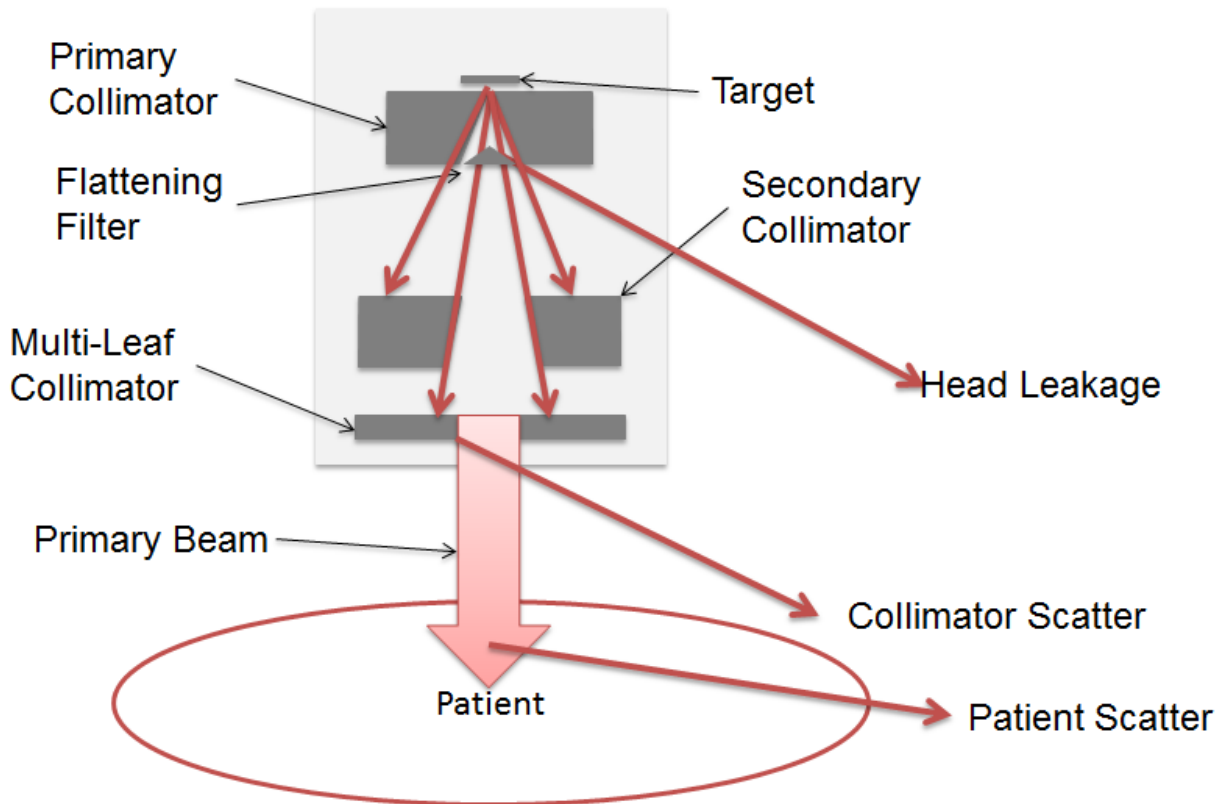


Figure 1-18 Illustrations of a treatment head showing the origin or the different component of peripheral dose

1.6.1.1 Effects of Flattening-Filter-Free Beams on Peripheral Photon Dose

The flattening filter was historically used to flatten the dose distribution at depth for non-modulated, conventional treatment fields (Figure 1-11). In the context of modern optimized fluence and dose modulation techniques, a flattened dose distribution at depth becomes less

important [18]. As such, the flattening filter can safely be removed during intensity modulated treatment. In flattening-filter-free (FFF) beams, the photons must go through one less attenuator before reaching the patient (the flattening filter is removed). This decreases the probability that a photon will be scattered before reaching the patient. In addition, because fewer photons are attenuated in the treatment head, FFF beams need to produce less photons to deliver doses similar to flattened beam. Both of these effects contribute to an overall reduction in the number of photons scattered in the treatment head, which results in a reduction in head leakage and collimator scatter. The result of the removal of the FF on peripheral photon dose was observed in phantom using both measurements [19] [20] and Monte Carlo (MC) dose calculation algorithm [21] [22]. A dose reduction of up to 70% in was found in 6 MV FFF beams compared to their 6 MV flattened equivalent [19].

1.6.1.2 Effects of Increasing Beam Energy on Peripheral Photon Doses

Patient scatter originates from the scattering of photons inside the patient. More specifically, it comes primarily from scattered photons resulting from Compton interactions. When looking at the angular distribution of Compton photons as a function of energy shown in Figure 1-2, it becomes apparent that scattered Compton photons are more forward directed (i.e. lower scattering angle) in higher energy beams compared to those from lower energy beams. A quick calculation using the information shown in Figure 1-2 and typical 6 and 10 MV spectra shows that the number of Compton photons scattered at Compton angles ranging from 70° to 110° is reduced by 20% in 10 MV beams compared to 6 MV beams. In terms of reducing patient

scatter, forward directed photons are ideal as they deposit their energy in the primary treatment area before exiting the patient instead of scattering to out-of-field tissues. The effect of beam energy on peripheral photon dose has been studied and results show that increased beam energy is associated with lower peripheral photon doses [23] [24].

1.6.2 Neutron Doses

The main source of neutron production during radiotherapy is photo-activation. This occurs when photons interact with nuclei thereby moving the nucleus to an excited state. Neutrons can be emitted (as well as other particles) when excited nuclei decay into a lower energy state [25]. In 6 and 10 MV linac beams, neutrons are mainly produced in the treatment head although some can be produced in the patient. In the treatment head, photo-activation mainly occurs in heavier nuclei such as isotopes of tungsten and lead. In patients, most photo-activation events occur with deuterium. For most other elements commonly found in the treatment room, the probability of photo-activation from 6 and 10 MV photon beams is negligible. Most of the neutron dose data in the literature reports neutron fluence or neutron dose in air, which is not an accurate measure of neutron dose at depth in humans. The main use of neutron fluence and neutron dose in air is to compare different modalities as these quantities are proportional to dose at depth and therefore can be used to determine relative neutron dose differences. Neutron dose in air can also be used as an upper limit to neutron dose at depth.

Because all neutrons come from photo-activation, there are fewer options to reduce neutron doses than for photon doses. The only way to reduce neutron doses is to reduce the number of photo-activation events. This can be done by reducing the distance photons travel inside high Z materials (thus reducing probability of an interaction), reducing the number of photons produced, or decreasing the photon energy. As for peripheral photon doses, FFF beams reduce neutron doses compared to flattened beams. This occurs because the removal of the flattening filter lowers the number of photons that needs to be produced by FFF beams to deliver an equivalent dose using flattened beams. Both of these factors lead to a decrease in the number of photo-activation events. This effect was observed by Kry *et al.* [26] using neutron fluence measurements of 18 MV beams and independently verified by Najem *et al.* [27] for 10, 15 and 18 MV. These studies found that the use of FFF beams reduced neutron fluences compared to flattened beams by up to 70% for energies of 15 and 18 MV and up to 50% for 10 MV beams. Interestingly, decreasing the photon energy has an opposite effect on peripheral neutron doses than it does on peripheral photon doses. This exemplifies why it is important to do a comprehensive assessment of all components of the source of peripheral dose before making recommendations on how to lower it. This effect was observed in a study published by Howell *et al.* [28] that showed that neutron fluence increases with energy.

Chapter 2

Monte Carlo Simulations and Dose Modeling

2.1 The Monte Carlo Method

The Monte Carlo (MC) simulation method is a technique that uses random sampling of probability functions to solve mathematical problems. Its main use is to predict a macroscopic outcome caused by series of microscopic events with a known probability distribution. By sampling the probability distribution to find the probability of an event occurring and knowing how each event influences the macroscopic outcome, this outcome becomes possible to predict. The outcome can be determined with an arbitrarily small uncertainty as long as a sufficient number of events are sampled. In practice, the number of events that needs to be sampled is often very large and as such the MC method is very computationally intensive. With the introduction of modern computers, this method has now become practical in a radiotherapy setting.

The following example illustrates how the MC method can be used to find the solution to a very complex problem if one doesn't have a calculator: the numerical value of π . Finding the numerical value of π is a complex problem, one that would puzzle most people without knowledge of university level mathematics. To solve this problem using the Monte Carlo

methods, one only needs knowledge of how to calculate the area of a square and the area of a circle (Eq. 2-1)

$$A_{circle} = \pi r^2, A_{square} = s^2 \quad 2-1$$

To find the numerical value of π , one can randomly distribute points on a circle inscribed inside of a square. If the points have been sampled from a uniform distribution, then the ratio of the number of points inside the circle and the total number of points will be equal to the ratio of the areas of the circle and the square. If f is the ratio between the length of a side of the square and the radius of the inscribed circle, n is the number of points inside the circle and N is the total number of points, then Pi will be given by Eq. 2-2.

$$\pi = \lim_{N \rightarrow \infty} f^2 * \frac{n}{N} \quad 2-2$$

Figure 2-1 shows this exact situation with a circle of radius 1 inscribed in a square with sides of length 4. A hundred points were sampled from a 2-dimensional uniform distribution. The number of points inside the circle is 19 out of a 100, which gives an approximation for pi of 3.04 which is about 3% off of the correct answer.

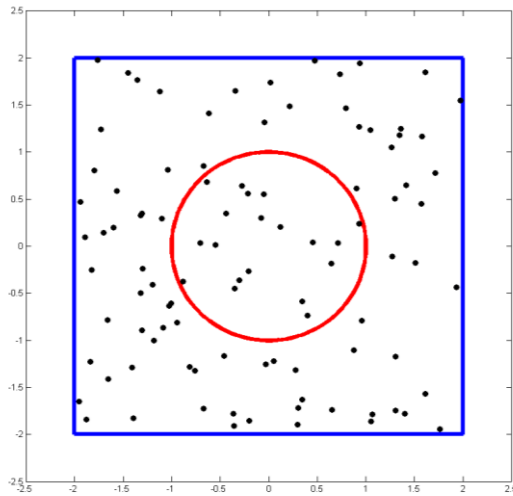


Figure 2-1 Representation of a square inscribed inside a square. Each dot was found from a uniform 2D distribution and the ratio of the number of dot in the circle to the total number of dot can be used to determine the value of Pi.

Another aspect of the MC methods that is illustrated by this example is that the usefulness of MC depends on the rate of convergence. To illustrate this, the example above was repeated with 100 million points. The value of Pi found in with this number of sampled points was 3.14214. This is only accurate to the second decimal place and has an error of about 0.01% of the value of Pi.

2.2 Monte Carlo for Radiation Transport

Calculating the amount of dose delivered by a given radiation beam is quite difficult and no purely analytical solution has been found. Dose calculations rely on the use of various measured factors (percent depth dose, peak scatter factors, tissue air ratios, etc.) that relate

how dose changes with beam arrangement and target location. While determining the dose delivered by a photon beam from first principles is difficult, determining the dose delivered by a single particle is not, if every interaction the particle goes through is known. Since the total dose is the sum of the dose given by every particle, the MC method is well suited to solve the dose calculation problem. In fact, MC is considered the gold standard and new dose calculation algorithms are often compared with MC to quantify how well they perform [29].

To illustrate how MC solves the problem of radiation transport and dose calculation, it is useful to follow the path of a single photon. Let us assume that a photon of energy E is perpendicularly incident on a rectangular water phantom of total depth d . The way MC determines every interaction between the photon and the water phantom is explained below. The first step taken by MC is to determine if the photon interacts and if so at what depth. As mentioned in section 1.2.3.4, the probability that a photon interacts while travelling a distance d through a medium is given by Eq. 1-10. The probability of interaction $P(x)$ takes values from 0 when the depth is 0 and 1 when the depth is infinite. If a value r between 0 and 1 is randomly assigned to $P(x)$, the corresponding depth can be found by inverting Eq. 1-10. The inverse of $P(x)$ is given in Eq. 2-3. It can be shown that if r is randomly sampled from a uniform distribution, the corresponding values of d will follow the exponential distribution found in Eq. 1-10. This method of sampling a probability distribution is called the transformation method.

$$d = -\frac{1}{\mu_p \rho} \ln(1 - r) \quad 2-3$$

Going back to our example, the depth of interaction between photon and water is found by the MC simulation by sampling $P(x)$ using the transformation method. Once the depth of interaction has been found, the next step is to determine the type of interaction that will occur. The main possible interactions are listed below and a detailed explanation of each interaction type is found in section 1.2.3.

- Rayleigh scattering
- Compton scattering
- Pair production
- Triplet production
- Photoelectric effect

The probability that a specific type of interaction will occur is given by Eq. 2-4, where c_i is the interaction specific attenuation coefficient and μ is the total attenuation coefficient. Figure 1-7 shows the probability of each interaction type as a function of incident photon energy in water.

$$P(i) = \frac{c_i}{\mu} \quad 2-4$$

To determine the type of interaction that will occur in the above example, a random number in the interval $[0, \mu]$ is chosen. If there are n possible interactions (l_1, l_2, \dots, l_n), the dependence between the selected random number r and the type of interaction is given by Eq. 2-5

$$I(r) = \begin{cases} I_1, & r \in [0, c_1] \\ I_2, & r \in (c_1, c_1 + c_2] \\ \vdots & \vdots \\ I_j, & r \in \left(\sum_{k=1}^{j-1} c_k, \sum_{k=1}^j c_k \right] \\ \vdots & \vdots \\ I_n, & r \in \left(\sum_{j=1}^{n-1} c_k, \mu \right] \end{cases} \quad 2-5$$

Once the interaction type has been decided, secondary particles are created and simulated. Their initial momentum and energy are chosen by sampling the appropriate distribution. The following is an example of how this might be done. For a Compton interaction, the probability distribution for scattering angle is given by the Klein-Nishina cross section given in Eq. 2-6.

$$\frac{d\sigma}{d\Omega} = \frac{r_e^2}{2} \left(\frac{E_{\gamma'}}{E_\gamma} \right)^2 \left(\frac{E_{\gamma'}}{E_\gamma} + \frac{E_\gamma}{E_{\gamma'}} - \sin^2 \theta \right) \quad 2-6$$

Because the Klein-Nishina formula is not invertible, the transformation method cannot be used to sample it. Sampling a distribution like the Klein-Nishina cross section can be done in a two-step process. First, a random number r_1 in the interval of possible scattering angle is selected. In the case of the Klein-Nishina formula, the scattering angle can take any value in the interval $[0, \pi]$. The second random number r_2 takes a value in the interval of $[0, \max(\frac{d\sigma}{d\Omega})]$. If it is smaller than the Klein-Nishina cross section for r_1 , $\frac{d\sigma}{d\Omega}(r_1)$, then r_1 is accepted and becomes the scattering angle. Otherwise, the process is repeated until a scattering angle is found.

The process of simulating charged particles is similar as the one for photons. However, while photons interact at most a few times before being absorbed or exiting the medium, charged particles will undergo hundreds of thousands of Coulomb force interactions before coming to rest [30]. This makes it computationally challenging to simulate charged particle interactions in the same manner. Every MC code has its own methods of handling this problem. Electron Gamma Shower- National Research Council (EGSnrc), the code used for the work in this thesis, uses a combination of the continuously slowing down approximation (CSDA) and multiple scatterings theory (MST) to handle charged particle transport. CSDA is an approximation that assumes that charged particles lose energy at a constant rate. More details on EGSnrc's treatment of electrons and photons can be found in NRC Technical Report PIRS-701 [31]. This entire process of simulating both primary photon and subsequent secondary particles is repeated for a number of primary photon until a dose distribution with sufficiently small uncertainty is obtained.

2.3 The BC Cancer – Vancouver's EGSnrc Monte Carlo Model

The National Research Council's EGSnrc is a modular Monte Carlo simulation code that aims at calculating the dose delivered by radiotherapy treatments. Two modules are used to calculate the dose delivered by external photon beams. The first module is called BEAMnrc which is used to model radiation transport inside a linac. The output of a BEAMnrc simulation is a phase-space file containing data about the momentum and position of every photon crossing the

phase-space boundary. That output is then given to the second module, DOSXYZnrc which handles radiation transport inside patients to calculate the absorbed radiation dose.

A model of a Varian TrueBeam (Varian Medical Systems, Palo Alto, CA) linac treatment head with a high definition MLC (HDMLC) was made using the BEAMnrc and DOSXYZnrc modules of the EGSnrc MC code [32] and an IAEA-compliant photon/electron phase-space provided by Varian [33]. This phase-space is captured above the secondary collimator (jaws) at a distance of 26.7 cm from the radiation source (x-ray target). Any particle not crossing the vendor-supplied phase-space is assumed to have a null contribution to the patient dose, leading to an underestimation of the peripheral dose. This is due to the omission of leakage and part of the head scatter photon contributions that are not captured in the boundaries of the phase-space planes. This occurs because phase-space interfaces are finite surfaces. Figure 2-2 shows a diagram of a linac head and the position of the two above-mentioned phase-space.

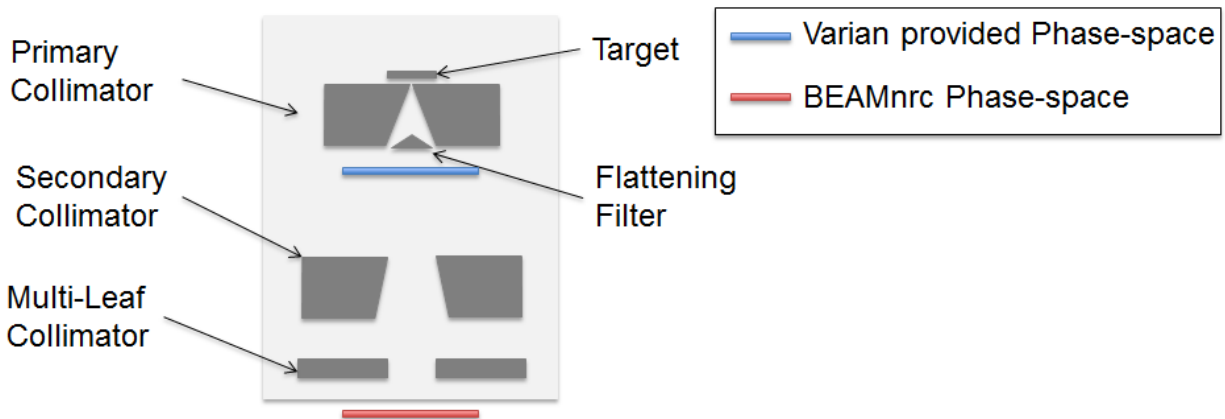


Figure 2-2 Representation of a linac head showing the position of the two phase-spaces used during a MC simulation. The phase-space provided by Varian is shown in blue and the phase-space outputted by BEAMnrc is shown in red.

The BEAMnrc “Source 20” [34] model of the TrueBeam accelerator and the DOSXYZnrc model for dose deposition in patient/phantom with absolute dose conversion code [35] used in this study were previously benchmarked [36] [37] [38] and are considered commissioned for clinical verification of radiotherapy plans for all energies used in this study. In order to lower the uncertainty in the low dose region, the BEAMnrc simulation of the accelerator and the DOSXYZnrc simulation of the patient dose uses 1.5 and 2 billion histories respectively. The default kinetic energy cut off of 0.010 MeV for photons and 0.7 MeV for electrons was used (AP = PCUT = 0.010 MeV, AE = ECUT = 0.7 MeV). All patient dose simulations were done using a 2.5x2.5x2.5 mm³ voxelized dataset created from a 3D computed tomography (CT) scan of the patient. The statistical uncertainty per voxel was < 3% for all voxels in every simulation

2.3.1 Benchmarking of the Monte Carlo Code

To ensure that dose calculations done by the MC model are accurate, it is important to benchmark the code. To do so, dose profiles at the depth of max dose (dmax) and percent depth dose (PDD) curves obtained by Monte Carlo were compared to those obtained by measurement in a water tank during the linac commissioning process. Figure 2-3, shows a comparison between the measured and MC calculated PDDs for 6 MV flattened, 6 MV FFF and 10 MV FFF 10x10 cm beams. Figure 2-4, Figure 2-5 and Figure 2-6 show the crossline and inline profile for 6 MV flattened, 6 MV FFF and 10 MV FFF respectively.

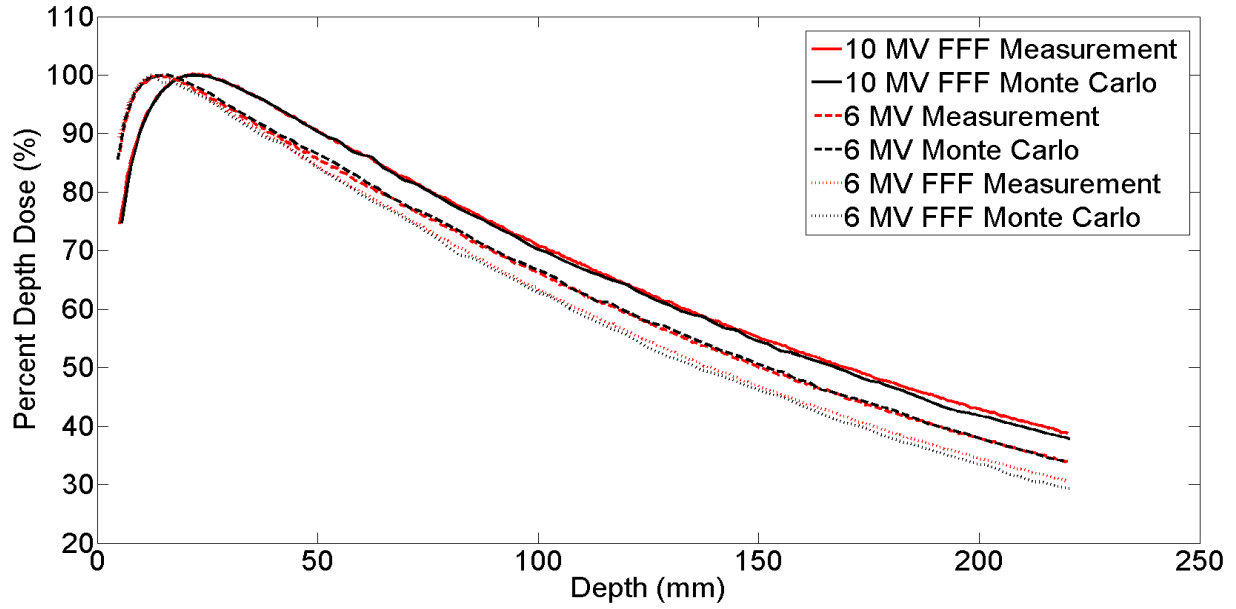


Figure 2-3 Comparison between measured (red) and MC calculated (black) PDD curves for a 10x10 field.

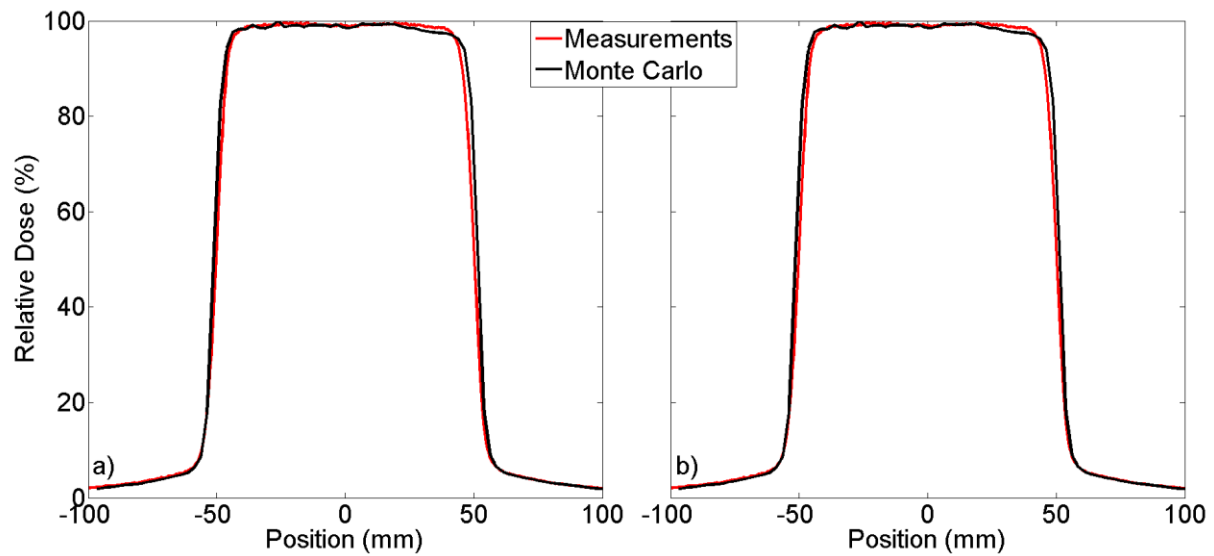


Figure 2-4 Crossline (a) and inline (b) profile of a 10x10 6 MV flattened beam at depth of 1.5 cm

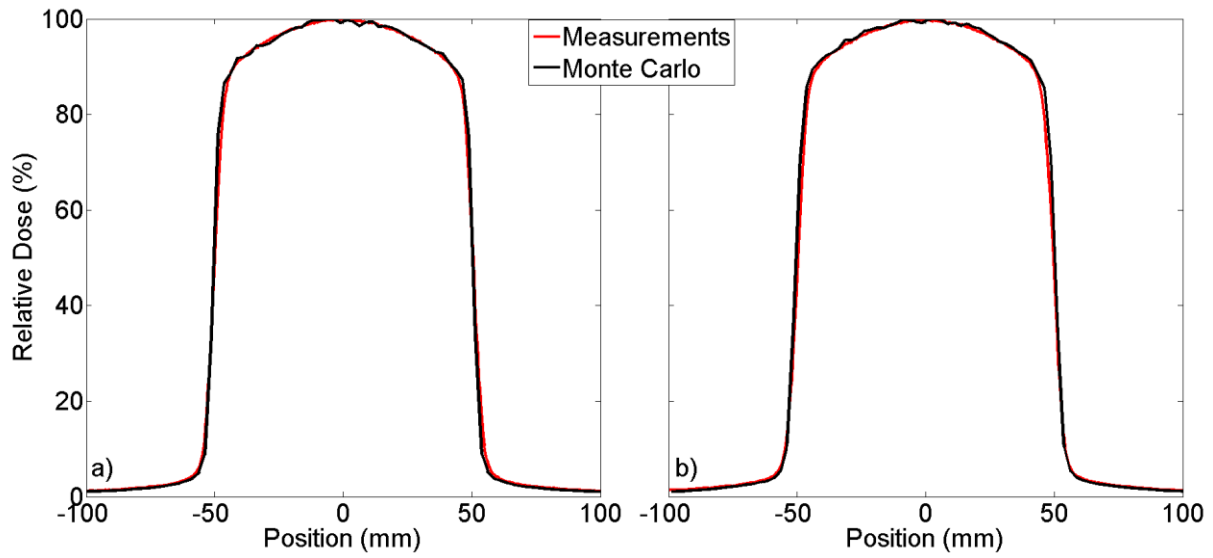


Figure 2-5 Crossline (a) and inline (b) profile of a 10x10 6 MV FFF beam at depth of 1.5 cm

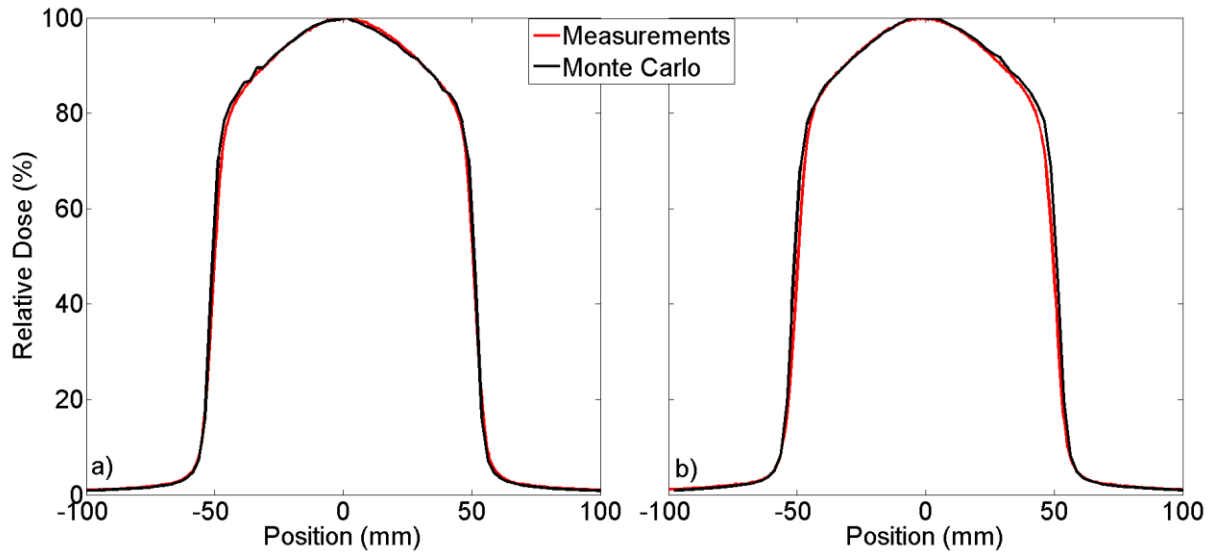


Figure 2-6 Crossline (a) and inline (b) profile of a 10x10 10 MV FFF beam at depth of 2.5 cm

Both PDDs and profiles showed a very high agreement between MC calculated dose and measurements. The maximum error in PDDs was < 2% which is within the expected value. The difference probably comes from positioning error both during the measurements and in matching the location between MC and measurements. While there was a good agreement between MC and measurements in the dose profiles in the infield region, MC calculated doses were lower in the low dose region (<10% of the maximum dose). This behavior is expected as the MC model underestimates out-of-field doses. To further verify the accuracy of our MC model, MC calculated dose distribution and DVHs were compared to those obtained by the Eclipse v.11 (Varian Medical Systems, Palo Alto, CA) treatment planning system, which employs the Analytical Anisotropic Algorithm (AAA) convolution algorithm with heterogeneity correction (v.11.0.31). The results of this comparison for a single patient are shown in Figure 2-7, which compared the MC obtained DVH with the Eclipse obtained DVH and in Figure 2-8, which compared the two dose distributions on an axial slice. This comparison shows very good agreement between the dose from MC and AAA. There is some discrepancy in the high dose gradient regions, but that is to be expected given that MC and Eclipse use different voxel size and boundaries. Another possible source of discrepancy between MC and Eclipse comes from the fact that MC reports dose to medium and Eclipse reports dose to water of different densities. For most tissues, this difference is negligible, however it can become substantial in tissues which interact with radiation in a way that is significantly different than water (e.g. bone)

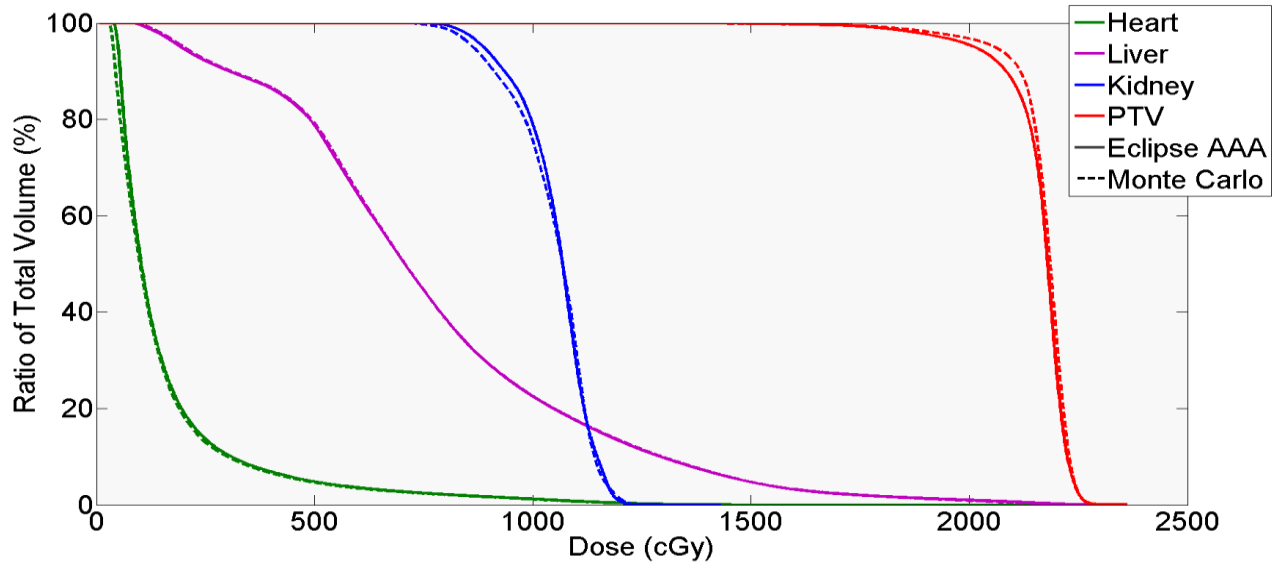


Figure 2-7 Comparison of Eclipse Calculated DVH (solid line) with the MC calculated DVH (dashed line) for a paediatric patient. Three OARs (heart, liver and kidney) and a PTV are shown.

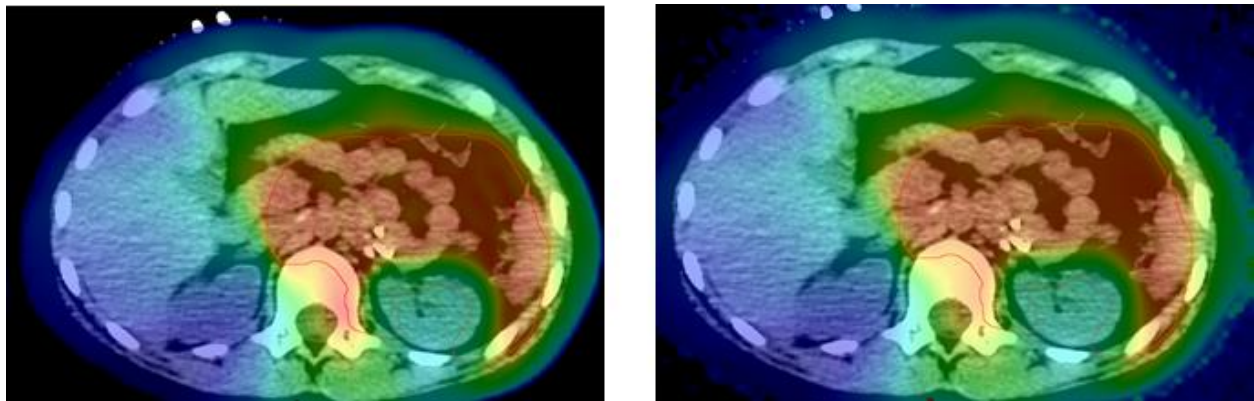


Figure 2-8 Axial slice comparing the Eclipse calculated dose distribution (left) with the MC calculated dose distribution (right)

Chapter 3 Combined Monte Carlo and Measurement Model for Peripheral Dose Calculation

3.1 Introduction

The MC model used for this study lacks the ability to properly assess peripheral doses because part of the head leakage and collimator scatter (Figure 1-18) are not captured in the two particle phase-spaces (Figure 2-2) used for the MC simulation. To assess peripheral doses in patients, a model that can accurately calculate peripheral doses from all sources of leakage and scatter needs to be constructed. This section introduces a new model based on a combination of measurements and MC simulations of a Varian TrueBeam linac located at BC Cancer - Vancouver.

3.2 Methods and Materials

There are four dose components to a photon beam from a linear accelerator: primary photons, patient scatter, head leakage and collimator scatter. Figure 1-18 shows the origin of these four components in the treatment head. It can be seen that the dose from the two components not simulated by our MC model (head leakage and collimator scatter) depend mainly on the

number of photons generated (i.e the number of MUs). As such, the model used in this study to assess peripheral dose assumed that the dose received by a voxel is given by Eq. 3-1 where D_{MC} is the dose calculated by our MC code, N_{MU} is the number of MUs delivered and $d_{L-S}(z,T)$ is the combined head leakage and collimator scatter dose per MU from a beam using delivery technique T at an axial distance z from isocenter. For simplicity, the correction to D_{MC} given by the second term of Eq. 3-1 will be referred to as “leakage correction”.

$$D_{Total} = D_{MC} + N_{MU} * d_{L-S}(z,T) \quad 3-1$$

The motivation of a using the simple model presented above to model head leakage and collimator scatter comes circular symmetry of VMAT treatments. Because the difference between the number of MUs delivered at each gantry angle is negligible, it is possible to approximate the source of head leakage and collimator scatter as a cylindrical shell along the path of the gantry. As such, it can be seen that the leakage correction along the gantry’s axis of rotation only depends on the axial distance from isocenter. Since patients are three dimensional, it is expected that some the leakage correction will have some dependence on the radial distance from isocenter but this is not accounted for in our model. Instead, the effect due to radial dependence was measured and included in the sources of uncertainty.

3.2.1 Measurement of the Head-Scatter and Leakage Correction

To measure $d_{L-S}(z,E)$ for the three beam modes used in this study (6 MV flattened, 6 MV FFF and 10 MV FFF), nine clinical plans (3 plans per beam mode) from three randomly selected patients were transferred onto a 23 x 30 x 60 cm³ slab phantom. The phantom was made of

“solid waterTM”, a plastic that interacts with radiation similarly to water. Two of the plans used 1 full VMAT arc and one plan used 2 full VMAT arc. Each radiotherapy plan was delivered to this phantom and the peripheral dose was measured at 10 different points in a coronal plane at the same depth in phantom as the isocenter (Figure 3-1). Measurements were taken at distances ranging from 17 to 45 cm from the isocenter. The exact position of each measurement points shown in Figure 3-1 is given in Table 3-1. The dose was measured using a 0.6 cc volume Farmer-type ion chamber (PTW-Freiburg, Freiburg, Germany). Measurement points A-G were used to determine the leakage correction while measurement points H-J were used to determine the uncertainty introduced by the small radial dependence of the leakage correction.

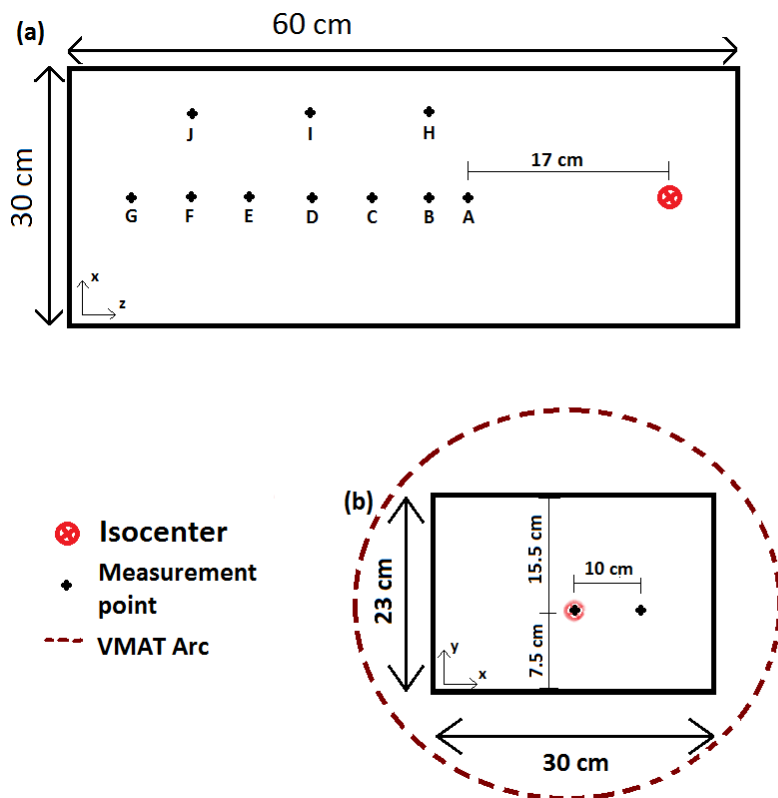


Figure 3-1 Top-view coronal (a) and an end-on axial (b) plane of the phantom showing the points of measurements and the position of the isocenter.

To lower uncertainty, multiple fractions were delivered for each treatment plans and the results were averaged. Measurements were converted to dose by performing a cross calibration at the linac calibration point and leakage current was measured to assess its effect on the results.

Measurement point	Longitudinal Distance from Isocenter (cm)	Lateral Distance from Isocenter (cm)
A	17	0
B	20	0
C	25	0
D	30	0
E	35	0
F	40	0
G	45	0
H	20	10
I	30	10
J	40	10

Table 3-1 Longitudinal and lateral distance from isocenter of each measurement point shown in Figure 3-1

The absolute dose difference per MU between MC and measurements as a function of the distance z from isocenter was calculated for all plans using Eq. 3-2.

$$d_{L-S}(z, E) = \frac{D_{Measured} - D_{MC}}{N_{MU}} \quad 3-2$$

From this data, an average energy-specific dose correction as a function of axial distance from the isocenter was established. In order to validate the “leakage correction” factor, the peripheral doses for 9 more plans (again, 3 plans for each of the 3 beam modes) were measured and compared to the corresponding leakage corrected MC dose simulation.

3.3 Results and Discussion

Prior to performing ion chamber measurements of peripheral dose, the electronic leakage current from the ion chamber/electrometer set-up was measured to be 10 ± 2 fA. This would lead to a maximum overestimation of measured doses at 35 cm and 45 cm from the isocenter of <1% and <2.5%, respectively. Measured peripheral doses ranged from approximately 10 cGy at 17 cm from isocenter to 5 mGy at 45 cm from the isocenter. The uncorrected MC and leakage corrected MC longitudinal dose profiles relative to the measured dose profiles for all 3 sets of validation plans are shown in Figure 3-2.

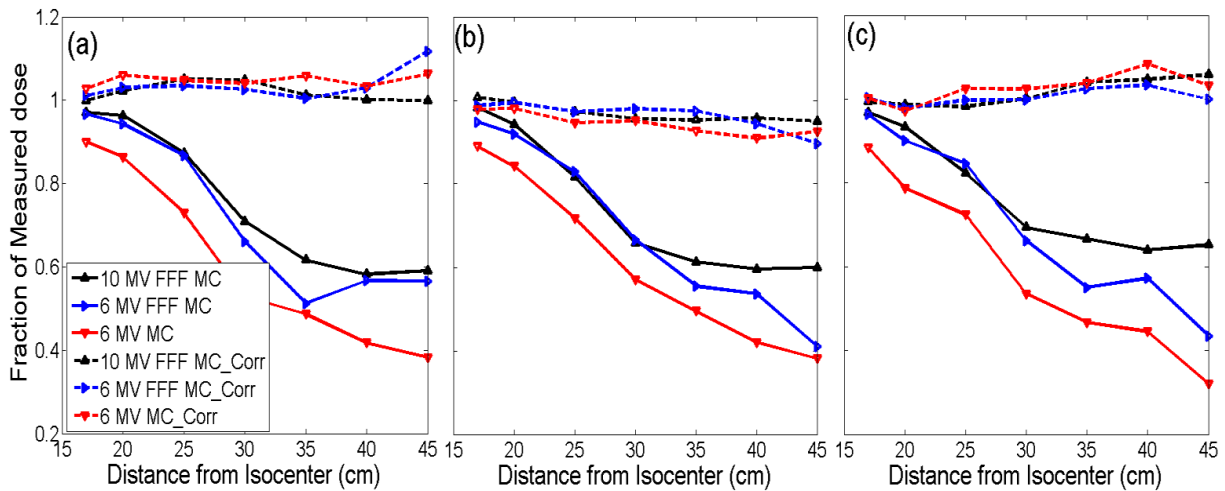


Figure 3-2 Uncorrected (solid line) and corrected MC (dashed line) dose profile along the longitudinal axis of the patient relative to the measured dose for three validation plans (a), (b), (c). Uncertainty was <3% for all points MC calculated points.

The mean relative difference between the corrected MC dose and measured dose for all 3 beam energies and all 9 plans combined was of 0.3% (95% Confidence interval (CI) [-0.8, 1.4]) where a positive value means that the corrected MC dose was higher than the measured dose. The energy specific mean relative difference was 0.6% [-1.7, 2.9], 0.2% [-1.7, 2.1] and 0.2% [-1.3, 1.7] for 6 MV-flattened, 6 MV FFF and 10 MV FFF respectively. Measurements done at points laterally distant from isocenter (point H, I and J in Figure 3-1) had a mean relative difference of -7.1% (95% CI [-4.9, -9.4]). This may be due to the model being based on measurements that were performed deeper in the phantom (points A to G in Figure 3-1) than the lateral points (points H to J on Figure 3-1). This would lead to our model underestimating the head scatter and leakage dose as it decreases slightly with depth [39]. The dose measurements at lateral points H, I and J were used to determine the uncertainty of our model due to the differences in patient size. This systematic underestimation was deemed acceptable as the goal was for this model to be used to determine if there was a relative peripheral dose reduction with 6 MV FFF and 10 MV FFF beam energies compared to the 6 MV-flattened beam energy in a clinical setting. An underestimation of leakage dose would not affect the validity of our findings as it would apply to all beam energies. Nevertheless, it was determined that an uncertainty of 9.4%, the upper bound of the mean relative difference between our prediction and measurements for points laterally distant to the isocenter, needed to be added to the modeled dose to account for this. The leakage and head scatter model used in this study assumes that the leakage dose and head scatter dose scales linearly with MUs. The small mean

relative difference (0.3%) between measured dose and corrected MC dose supports this assumption.

3.4 Conclusion

The BC Cancer – Vancouver’s Monte Carlo model of a Varian TrueBeam medical linear accelerator does not accurately simulate peripheral dose. A correction scaling linearly with the number of MUs delivered was created using ion chamber measurements. The corrected MC model was validated for 6 MV flattened, 6 MV FFF and 10 MV FFF. For all energies, the relative difference between the corrected MC model and measurements was $< 0.6\%$ for points along the longitudinal axis at the level of the isocenter. For points laterally distant to the isocenter, a mean relative dose difference of $< 9.4\%$ was found. Based on comparisons with measured peripheral dose, this model was found to be accurate enough to be used to calculate peripheral dose in patients.

Chapter 4

Effects of 10 MV and Flattening-Filter-Free Beams on Peripheral Dose in Paediatric Patients

4.1 Introduction

It has been shown that upwards of 60% of SMNs occur in the beam-bordering region and that 30% occur in regions very distant from the PTV [7] [40] [41]. Since peripheral dose is a major component of the dose in those regions, lowering it is a high value objective when it comes to reducing risk of SMNs. While many studies have tried to characterize peripheral doses for a variety of techniques, few studies have looked at patient specific peripheral dose. An even smaller number have looked at population-based dosimetry statistics for a group of patients. Cashmore et al. [19] found that Intensity Modulated Radiotherapy (IMRT) using 6 MV FFF beams reduced peripheral dose by up to 64% compared to conventional 6 MV flattened IMRT in a group of 5 paediatric patients treated with intracranial irradiation. Murray et al. [42] and Dobler et al. [43] found that FFF beams reduced the risk of SMN in out of field organs after prostate and right-sided breast irradiation respectively. There is a need for further data to determine the dosimetric effect of FFF beams and of beam energy in a large range of paediatric treatment cases and anatomical sites. A comprehensive study of peripheral dose in paediatric patients would offer guidance in deciding what beam modality to treat paediatric patients with.

This is important as paediatric patients often have very different body type compared to adults. The goal of this study is to determine how much of an effect FFF and high energy beams have on the mean peripheral dose received by a population of paediatric patients treated with VMAT. This was accomplished by retrospectively re-planning paediatric patient cases, originally treated with 6 MV-flattened VMAT, using 3 different beam modes, 6 MV-flattened, 6 MV FFF and 10 MV FFF. The population mean dose as a function of distance from PTV for each technique was calculated. To our knowledge this is the first study to perform a population-based dosimetric assessment of peripheral dose in paediatric patients treated with VMAT to various treatment sites.

4.2 Methods and Materials

4.2.1 Patient Selection and Planning

This study received approval by the institution Research Ethics Board (#H13-01632). 24 paediatric patients treated with volumetric modulated arc therapy (VMAT) at our center after 2012 were retrospectively reviewed and anonymized. If a patient had received treatment to more than one site, each site was evaluated and anonymized independently. Of the 24 selected patients, 22 had a single eligible PTV and 2 patients had two eligible treatment sites. This combined to a total of 26 PTVs. Cohort information can be found in Table 4-1.

A radiotherapy plan was created for each of the three beam modes (6 MV-flattened, 6 MV FFF and 10 MV FFF) for each of the 26 PTVs (78 plans in total). All plans met the same organ-at-risk

(OAR) dose constraints and PTV coverage objectives as defined in the physician approved dose constraint sheets for that particular treatment.

Treatment Sites	Number of Radiation Courses	Mean Prescription Dose (Gy) [min/max] ± SD	Mean PTV Volume (cc) [min/max] ± SD
Head & Neck	7	26.7 [12/45] ± 11.2	227.7 [57/363] ± 292.2
Thorax	5	24.9 [21/32] ± 4.8	350.2 [112/824] ± 113.7
Abdomen	14	24.5 [11/50] ± 10.8	520.5 [165/1492] ± 435.1
All Sites	26	25.1 [11/50] ± 9.7	408.9 [165/1492] ± 363.4

Table 4-1 Number of plans per treatment site, mean prescription dose, and PTV volume in paediatric cohort.

No clinically significant differences in PTV coverage were observed between the different beam modes as all plans met the PTV coverage objectives. The OAR dose constraints were cautiously derived from the QUANTEC publications [44]. These constraints were modified by the radiation oncologist based on the particular clinical situation (e.g. patient age, disease type and location, and antecedent clinical factors). Generally, the highest priority for abdominal treatments was to reduce spinal cord and kidney dose. For thoracic treatments, the highest priority was to reduce spinal cord and lung dose. For head and neck treatments, dose constraints to the optic structures, spinal cord and brain stem were given the highest priority. For all patients, once

OAR constraints were considered, the planning goal for the PTV was the same: $V_{95\%} \geq 98\%$ and $D_{\max} \leq 110\%$ of the prescription dose.

All plans were created using the Varian Eclipse treatment planning system v.11 and planned for a Varian TrueBeam equipped with HDMLC (2.5 mm wide leaves at centre of field). The dose calculation algorithm was the Varian AAA with heterogeneity correction (v.11.0.31). The three beam modes evaluated in this study were commissioned on the treatment linac as part of its clinical use. The mean energies of the FFF modes are unmatched, meaning that for a given beam energy specification (e.g. 6 MV) the mean energy is lower for the FFF beam than for the equivalently named flattened beam. For example, the mean energy of a 6 MV beam is ~ 1.30 MeV in FFF beams and ~ 1.6 MeV in flattened beams [11] [12].

4.2.2 Dose Analysis

4.2.2.1 Creation of Isodistant Dose Shells

Expressing the peripheral dose as a function of distance from the PTV edge requires splitting the patient CT volume in regions containing voxels that are equidistant from the PTV. To define these sub-volumes, shells were created around the PTV (Figure 4-1). Each shell had a thickness of 1 cm and each voxel in a shell had a distance to the PTV within 0.5 cm of the mean distance to the PTV of all voxels in that shell. Voxels in the path of the primary beam were excluded from all shells in order to focus on peripheral dose effects. For each patient, up to 30 shells were created with mean distance to the PTV of 0.5 cm to 29.5 cm. For patients with CT scans that

were too small to create 30 shells, shells were created until they contained less than 500 voxels. Shells with less than 500 voxels (partial shells towards the edge of the CT volume) were not included because of the increased uncertainty from stochastic effects inherent to MC simulations and from the lack of scatter equilibrium arising from missing patient CT data. This number of voxels was chosen as a cut-off because it was a small enough cut-off

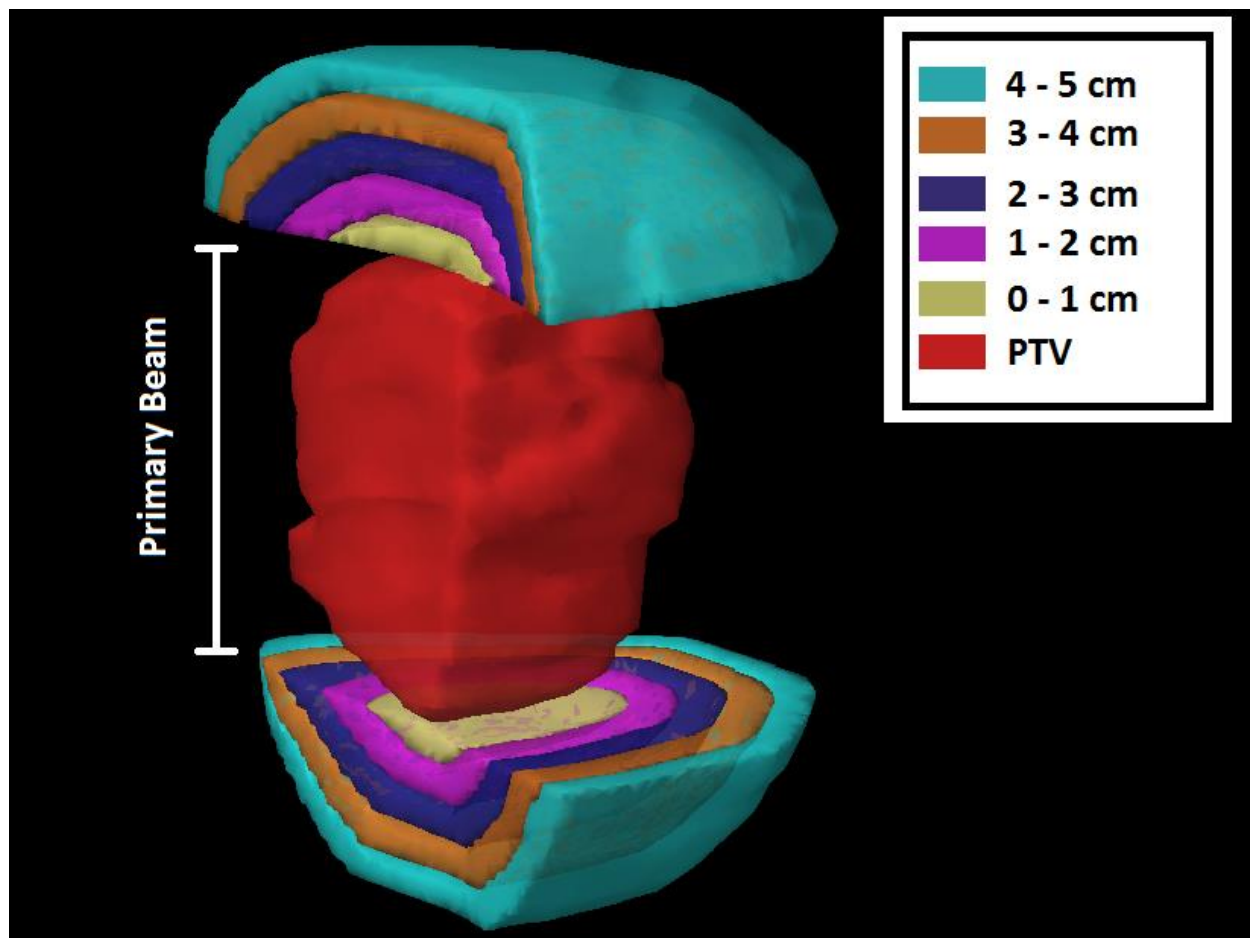


Figure 4-1 Illustration of the first 5 shells expanded around the PTV. The legends indicate the distance from the PTV of voxel within each shells and identifies the PTV.

to not exclude any full shells around small PTVs and large enough to exclude partial shells near the extreme geometric limits of the CT set.

For each of the shells, the mean dose was calculated using the “leakage corrected” MC model described and assessed in Chapter 3. In order to account for the different prescriptions received by patients in our study, the peripheral doses delivered by the 6 MV FFF and 10 MV FFF beams were normalized to the corresponding 6 MV-flattened dose. The resulting relative dose was averaged to find the population mean relative dose and a t-test was used to determine the 95% confidence interval. A source of uncertainty in the concentric dose shell analysis method is that the dose received by a voxel depends on both its distance from the PTV edge and on its position within the shell. A measurement of the variance between dose profiles taken in different directions in a coronal plane passing through isocenter was used to quantify this uncertainty.

4.2.2.2 Integral Relative Dose

The integral relative dose (IRD) was found for both FFF beams. It was calculated by integrating the peripheral dose relative to 6 MV-flattened with respect to distance from the PTV edge. This was used as a measure of total peripheral dose in a statistical analysis to determine whether or not various plan properties or clinical factors were associated with a relative change to peripheral dose. Factors assessed included MU, treatment site, PTV volume, and total prescription dose. For numerical variables (PTV volume and prescription) the Spearman’s rank

correlation coefficient was found and a t-test was used to determine the significance. For treatment site, an ANOVA was performed to determine if there was any association with IRD.

4.2.3 Neutron Measurements

One of the main concerns with using higher (e.g. > 8 MV) photon beam energies for paediatric treatments is the increased production of neutrons due to photo-nuclear interactions [28].

While neutron doses are lower by about 70% in FFF beams [26], a full comparison of 6 MV-flattened, 6 MV FFF and 10 MV FFF cannot be done without acknowledging the neutron dose contribution.

The Neutrak CR-39 Fast/Intermediate/Thermal neutron detector (Landauer, Inc., Glenwood, IL) was used for all neutron measurements. It is a solid state nuclear track etch detector. Only the 6 MV-flattened and 10 MV FFF beams were assessed as they were expected to result in the highest neutron doses. No radiation weighting factor was used as the Neutrak CR-39 detectors are calibrated to measure equivalent dose. These detectors are sensitive to neutrons with energy between 0.25 eV and 40 MeV and can measure doses in the 0.1 – 250 mSv range.

Because of the difficulty associated with low dose neutron measurements, it was not possible to obtain a full 3D neutron dose characterization. Instead, a few point doses were measured at representative locations. Each Neutrak detector was placed on a 5 cm slab of solid water at distances of 20 and 40 cm from the isocenter along the long axis and covered with a 1 cm thick water equivalent bolus. Each detector was irradiated with a representative paediatric VMAT

plan, delivered using the 6 MV-flattened and 10 MV FFF beams. The plan was redelivered until the estimated dose received by the detector was within the measurable dose range (as specified by the manufacturer). In order to verify that the measured neutron dose per MU delivered did not depend on the specific VMAT plan, we repeated these measurements for a second representative paediatric VMAT plan.

4.3 Results

4.3.1 Relative Photon Peripheral doses for FFF beams

4.3.1.1 Dose-Distance Relationship

To quantify the uncertainty from the use of dose shells in the analysis of our data, the variance between dose profiles taken in different radial directions in a coronal plane passing through isocenter was assessed. Figure 4-2 shows the dose profile as a function of distance from PTV edge for profiles taken at every 10° from -30° to 30° and from 150° to 210° for one of the patient in our cohort. The position of the angles relative to the patient's body is also shown in Figure 4-2.

The variation between profiles taken at different angles was assessed by dividing the difference between the minimum and the maximum profile dose value (range) by the mean value at each distance from the PTV. The profiles were maximally different at distances of less than 3 cm from the PTV. In that region the range could be up to 50% of the mean dose. However, the

variation in profile doses decreased with increasing distance from the PTV. At distances of 10-30 cm from the PTV the range of dose values was $15\% \pm 5\%$ of the mean dose

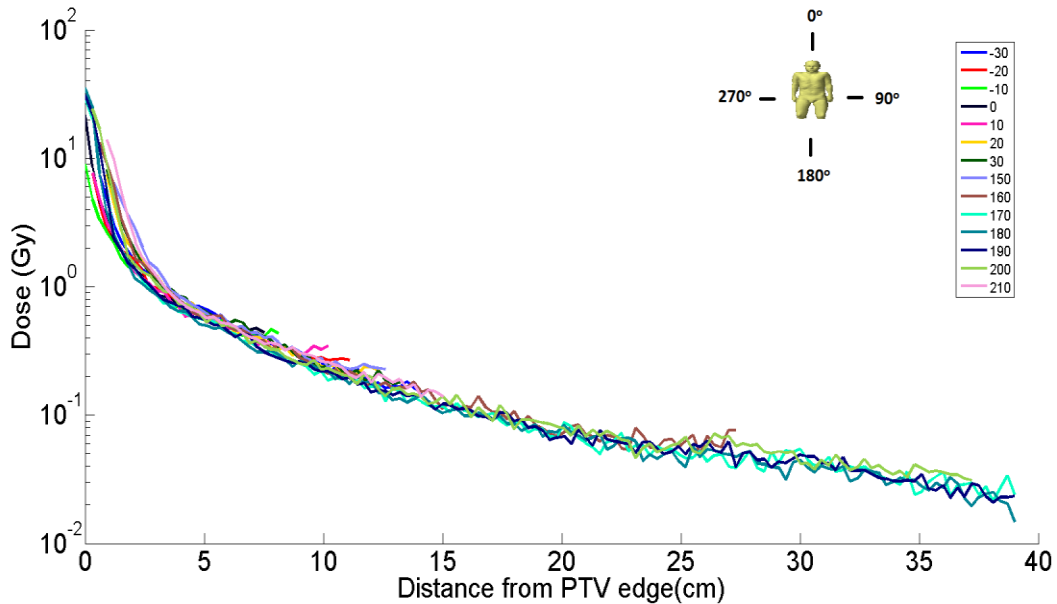


Figure 4-2 Dose as a function of distance from the PTV edge for a patient receiving 6 MV-flattened thoracic irradiation. Angle positions relative to the patient’s body are shown in the diagram next to the legend. Uncertainty was <3% for all MC calculated points.

Both 6 MV FFF and 10 MV FFF beams delivered lower peripheral doses relative to the 6 MV-flattened beam (

Figure 4-3). The dose reduction was of 9.8% (95% CI [8, 11.6]) and 3.9% (95% CI [2.1, 5.7]) at 5 cm from the PTV and 21.9% (95% CI [13.7, 30.1]) and 25.6% (95% CI [17.6, 33.6]) at 30 cm for 6 MV FFF and 10 MV FFF respectively. In absolute dose, this represents a reduction at 5 cm from the PTV edge of 4 mGy and 1.5 mGy per gray of prescribed dose. In the region < 2 cm from the PTV, 10 MV FFF delivered an increased dose of 2% (95% CI [0.6, 3.4]) or 3mGy/Gy of target dose

compared to the 6 MV-flattened beam. The uncertainty on the mean dose per shell from MC was lower than 1% due the high amount of voxels per shell. The uncertainty on the results shown in Figure 4-3 was determined by adding the uncertainty from MC and our model in quadrature with the 95% CI of the population mean dose. The absolute dose as a function of distance from the PTV edge for all three beam modes is shown in Figure 4-4.

Because using isodistant dose shells is a novel method, peripheral dose was also measured along longitudinal dose profiles (Figure 4-5). This allows for a comparison of the modelled peripheral dose to what is reported in the literature. The dose profiles agreed overall with the results from the shell dose analysis. There was some differences in dose close to the PTV between the shell model and the dose profiles but this is expected as dose close to the PTV is not uniform (Figure 4-2). At larger distance from the PTV, the difference between the results from the dose shells (Figure 4-3) and the profiles (Figure 4-5) was minimal.

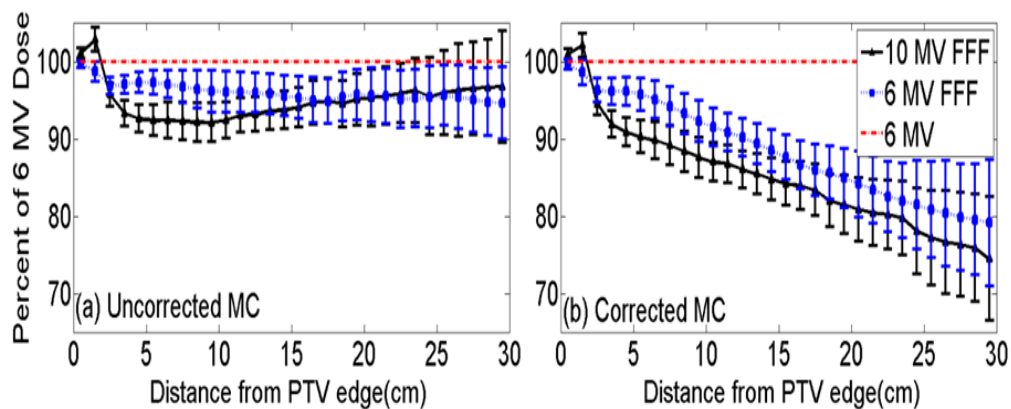


Figure 4-3 Uncorrected MC (a) and “leakage”-corrected MC (b) population mean peripheral dose as a function of radial distance from PTV edge determined by using concentric shells. 10 MV FFF (solid line) and 6 MV FFF (dotted line) beam relative to the 6 MV-flattened beam (horizontal dashed line) are shown.

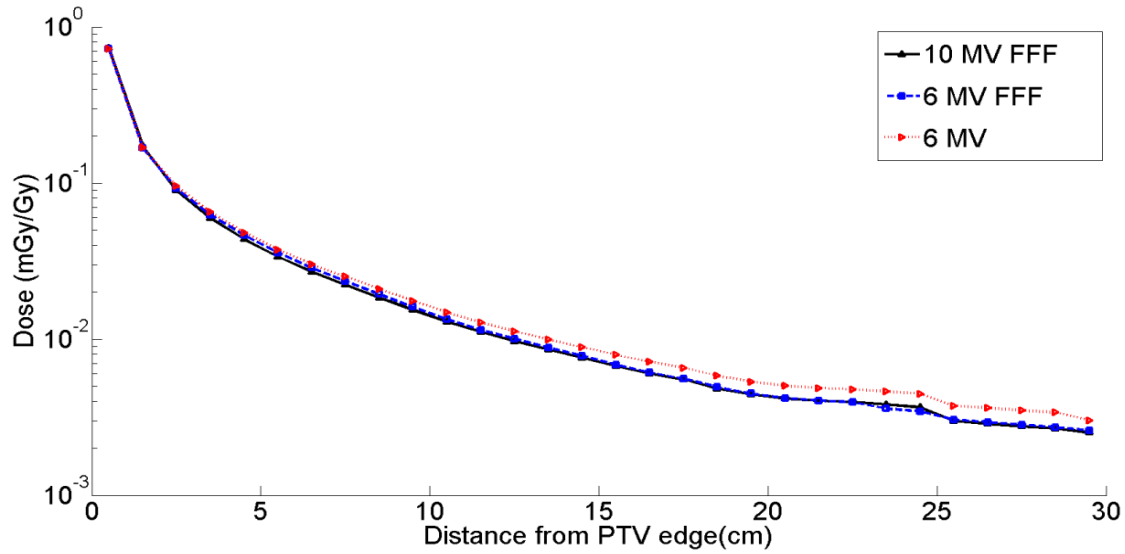


Figure 4-4 “Leakage”-Corrected MC calculated absolute population mean peripheral dose in mGy per Gy of prescription dose from the 10 MV FFF (solid line), 6 MV FFF (dashed line) and 6 MV flattened (dotted line) dose as a function of distance from PTV edge. Uncertainty was 0.5% close to the PTV edge and reaching a maximum of 8% at 30 cm from the PTV edge. The error bars are too small to show.

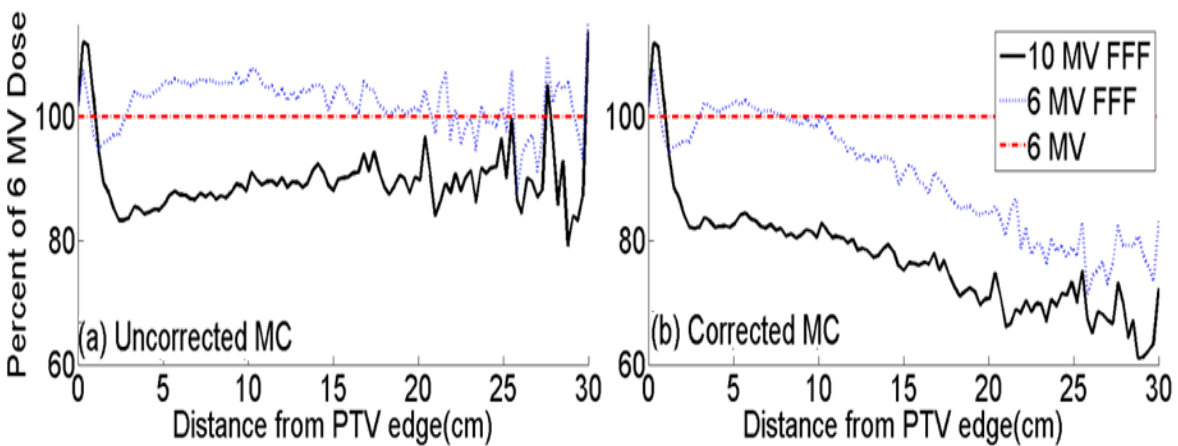


Figure 4-5 Uncorrected MC (a) and “leakage”-corrected MC (b) population mean peripheral dose profile as a function of longitudinal distance from PTV edge. 10 MV FFF (solid line) and 6 MV FFF (dotted line) beam relative to the 6 MV-flattened beam (horizontal dashed line) are shown.

4.3.1.2 Clinical Factors affecting Integral Relative Dose

Several clinical and plan factors were assessed for association with integral relative dose (IRD). The results of a multivariate analysis did not show an association between IRD and the site of the tumor, the prescription dose or the size of the PTV. However, this study was not powered to identify an association between these factors and IRD. As such, it should be noted that the possibility of such an association cannot be refuted based on the results of this study. The factor most associated with IRD was prescription dose with a p-value of $p=0.4$. Table 4-2 lists the significance of association between all clinical factors and IRD. FFF plans required significantly more MUs ($p < 0.001$) compared to 6 MV-flattened plans, however the IRD still shows that employing FFF beams reduced peripheral dose when compared to 6 MV-flattened beams. The 10 MV FFF beam was associated with lower IRD ($p = 0.002$) when compared with 6 MV FFF. Percent differences in IRD between the two FFF beams and the unflattened beam are shown in Figure 4-6.

Clinical Factor	Significance of Association with IRD
Treatment Site	$p = 0.8$
Prescription	$p = 0.38$
PTV size	$p = 0.77$
Beam mode(6 MV FFF, 10MV FFF)	$p = 0.002$

Table 4-2 Significance of association between several clinical factors and IRD.

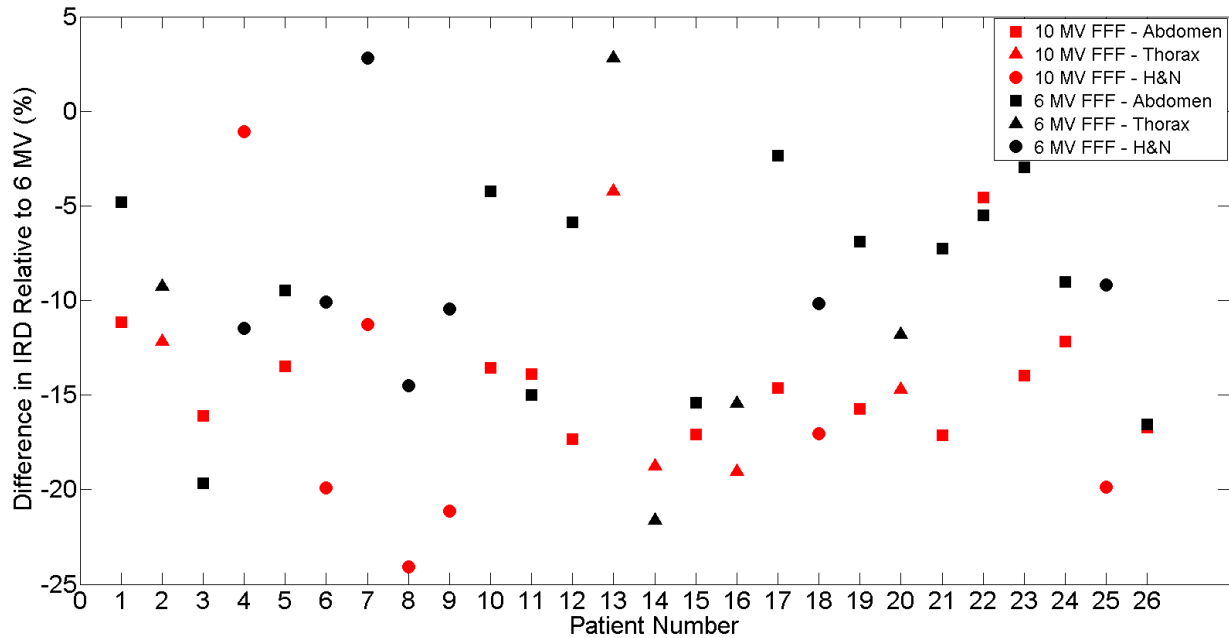


Figure 4-6 Percent difference in integral relative dose between the two flattening-filter-free beams and the flattened beam for all patients. 10 MV FFF is shown in red and 6 MV FFF is shown in black. Square, triangle and circle markers show treatments to the abdominal, thoracic and head & neck region respectively.

4.3.2 Neutron Doses

All Neutrak detectors received a dose below the minimum measurable dose of 100 μSv . While the Neutrak detector experiment did not allow us to provide an exact neutron dose per MU, we were still able to determine a maximum value. We found that the maximum possible neutron dose per MU was 0.019 $\mu\text{Sv}/\text{MU}$ and 0.042 $\mu\text{Sv}/\text{MU}$ for 6 MV-flattened and 10 MV FFF beams respectively. Using this limit, the maximum neutron dose received by a patient in our study was 522 μSv for the 10 MV FFF beam, and 203 μSv for the 6 MV-flattened beam (0.9% and 0.2% of the minimum photon dose received by that patient respectively). These upper neutron dose limits are orders of magnitude less than peripheral photon doses. Note that the 6 MV FFF

neutron doses were not measured, but are expected to be less than the 6 MV flattened beam because of the removal of the flattening filter.

4.4 Discussion

Dose was assessed using both concentric shells and longitudinal profiles. The use of concentric shells is subject to some uncertainty from the dependence of dose on the radial direction. This dependence adds some uncertainty to the results as it was found that the difference between minimum and maximum dose received by a shell could vary by up to 50% of the mean dose in the near-to-PTV region (< 3 cm), but drops to 15% in the peripheral regions >10cm. This effect will apply to all energies and is unlikely to have an impact on relative dose evaluations. While the use of concentric shells is subject to uncertainty from the dependence of dose on radial direction, it has the advantage of accounting for the full 3D distributions. This is something that cannot be accounted for with the use of longitudinal dose profiles. Despite the different methods, the results from using concentric shells and longitudinal profiles were similar.

The reduction in peripheral dose from removing the flattening filter and from increasing the beam energy in a cohort of 26 paediatric patients is consistent with the results reported for phantom and single patient studies [19] [20] [21] [45]. Flattening-filter-free plans required more MUs due to the increase fluence modulation needed, but still delivered a significantly lower integral relative dose ($p < 0.001$) compared to the 6 MV flattened beam. The 10 MV FFF beam delivered a significantly lower IRD ($p = 0.002$) than the 6 MV FFF. Compton scatter resulting

from a 10 MV beam is more forward directed relative to the scatter coming from a 6 MV beam [21]. Because of this effect, the 10 MV FFF beam resulted in a significantly lower dose in the “beam bordering” region (> 1 cm and < 5 cm from PTV edge) than both the 6 MV-flattened and 6 MV FFF beams (as shown in Figure 4-3). The dose reduction from 10 MV FFF beams was up to 10% in that region compared to 6 MV-flattened while the dose reduction from 6 MV FFF beams was up to 4%. This is an advantage as multiple studies have shown that a large fraction of SMN appear in this “beam bordering” region [40]. An exception to this occurs for tissue very close to the PTV < 2 cm. In that region, 10 MV FFF delivers a dose of up to 2% higher than 6 MV beam. This can be explained by the increased electron range associated with the higher photon energy and the fact that Compton electrons are scattered more laterally in higher energy beams. This results in a larger penumbra region in 10 MV beams than in 6 MV beams. The maximum dose increase in that region compared to 6 MV is 3 mGy/Gy of target dose which is smaller than the dose reduction of 4 mGy/Gy at 5 cm from the PTV edge. This increase in dose is therefore unlikely to negate the benefits of 10 MV FFF compared to 6 MV.

For tissues further from the field edge there is no significant difference between the two FFF beams, but the difference between the two FFF beams and the 6 MV-flattened beam continues to be significant and increases with increasing distance from the PTV edge. One source of uncertainty that could affect these results is that there is some non-uniformity in the dose received by the concentric shells.

While absolute neutron doses could not be estimated, upper limits on the neutron dose per MU for 6 MV-flattened and 10 MV FFF beams were established. The measured maximum neutron dose reported in the results section (0.042 $\mu\text{Sv}/\text{MU}$ and 0.019 $\mu\text{Sv}/\text{MU}$ for 10 MV FFF and 6 MV-flattened beams respectively) were lower than the 0.9 $\mu\text{Sv}/\text{MU}$ for 10 MV reported in TG-158 [45]. This difference can be explained by the difference in neutron production between flattened and FFF beams and by the fact that the TG-158 values are for neutron doses in air while our measurements were done in phantom. Our values are similar to organ dose estimates measured by Kry et al. [24] who reported neutron doses between 0.06 – 0.28 $\mu\text{Sv}/\text{MU}$ for 10 MV flattened beams. Using the limits that were measured, it was found that neutron doses were < 1% of the local photon dose in all patients and that the maximum neutron dose received by all patients was < 522 μSv .

The main limitation of our work is that we do not report organ absolute risk of SMNs for the different modalities. Some clinical studies have shown that risk of SMN is linear with dose for a wide range of doses and organs [46]. Under that assumption, relative dose and relative risk of SMNs have a directly proportional relationship. For the example of prostate radiotherapy, Kry et al. [47] demonstrated that the ratio of risk estimates between modalities can be useful under certain conditions.

4.5 Conclusion

Paediatric VMAT patients could benefit from reduced peripheral photon dose exposure when treated with FFF photon beams, particularly when combined with the higher 10 MV energy. 10 MV FFF beams reduced the peripheral dose by up to 9.8% (95% CI [8, 11.6]) in the beam-bordering region while the 6 MV FFF beams showed a smaller dose reduction of up to 3.9% (95% CI [2.1, 5.7]) in that region. At 30 cm from the PTV, the dose reductions were 21.9% (95% CI [13.7, 30.1]) and 25.6% (95% CI [17.6, 33.6]) for 6 MV FFF and 10 MV FFF respectively. While it is possible that using 10 MV FFF beams increased the neutron dose, the upper limit on neutron dose for the 10 MV FFF was found to be < 1 % of the minimum photon dose. Compared to 6 MV-flattened and 6 MV FFF beams, 10 MV FFF beams reduced peripheral photon doses more in the beam-bordering region (<5 cm from PTV), an area prone to develop SMN, and increased the neutron dose by a negligible amount. Assuming a linear relative risk model for SMN for low radiation doses, reducing peripheral doses will reduce the relative risk to organs exposed to peripheral radiation dose. 10 MV FFF should therefore be considered when treating VMAT paediatric patients.

Chapter 5

Reducing the Thyroid and Breast Dose

during Whole Lung Irradiation Using

Flattening-Filter-Free Beams

5.1 Introduction

Whole lung irradiation (WLI) is a treatment used to treat lung metastases in paediatric patients with a primary diagnosis of Ewing sarcoma (ES), Wilms' tumor and rhabdomyosarcoma [48] [49] [50]. It is an integral part in managing lung metastases for all three of these diseases and has been shown to increase 3-year progression-free (defined as the time from diagnosis of the metastatic disease to the diagnosis of subsequent metastases, or to the death of the patient) survival from 14% to 36% in patients with metastatic ES [51]. However, it is also associated with serious late side effects, some of which are life-threatening. Women who have received WLI during childhood for ES have an excess absolute risk (EAR) for breast cancer of 5.6 [52]. Breast Hypoplasia, a condition characterized by the underdevelopment of mammary tissues, has also been linked to doses of radiation similar to those received during WLI [53]. In a study of

childhood cancer survivors who received WLI for Wilms' tumor, Morgan et al. observed that WLI was associated with an increased risk of thyroid dysfunction [54]. Furthermore, it is well known from both the atomic cancer survivors study [55] and from cancer survivors follow up studies [56] [57] that the thyroid gland is susceptible to developing radiation-induced cancers. In view of these findings, it is important to lower the dose delivered to both the thyroid gland and female breasts during WLI. This study looks at how the peripheral dose reduction from FFF and 10 MV beams found in Chapter 4 affects the thyroid and female breast dose and risk of second cancer in paediatric patients receiving WLI.

5.2 Methods and Materials

5.2.1 Treatment Planning and Dose Assessment

Ten previously treated paediatric patients (6 males, 4 females) who had CT scans that included both the lungs and the thyroid were selected. On each patient's CT, the lung, heart and thyroid were contoured as well as the breasts for female patients. The PTV was determined by adding a 5 mm margin to the bilateral lungs contour. An example of those contours is shown in Figure 5-1. The prescription dose to the PTV was 14.4 Gy in 8 fractions for all patients. Three WLI treatment plans (one using each of 6 MV flattened, 6 MV FFF and 10 MV FFF) were created for every patient using a 3 arc VMAT technique. The same OAR and PTV dose constraints were used for all plans and are shown in Table 5-1.

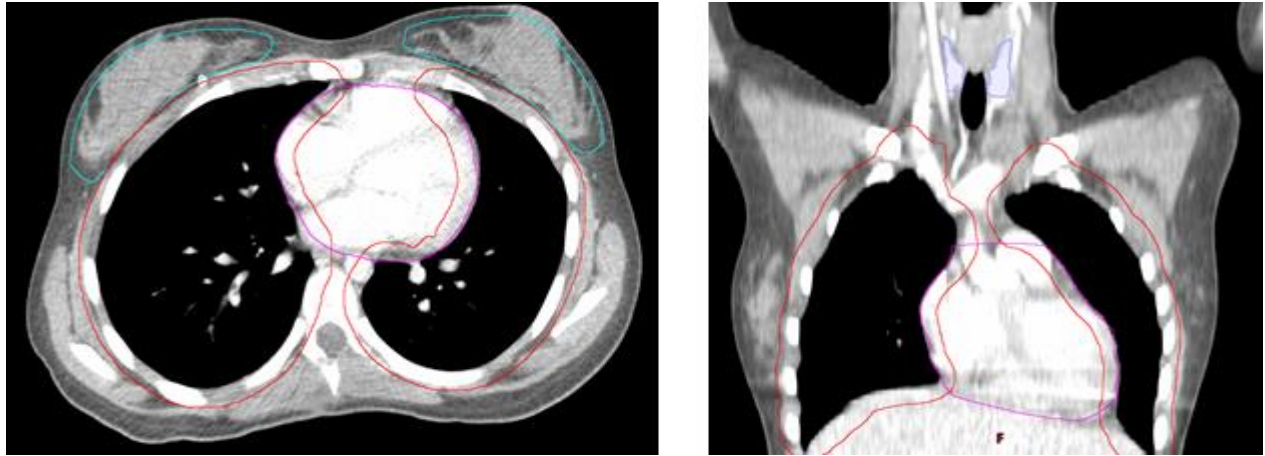


Figure 5-1 Axial (left) and coronal (right) CT slice of a female patient showing patients showing the different contours : PTV (red), breast (light blue), heart (magenta) and thyroid (lavender)

Structure	Dose Constraint
PTV	$V_{95\%} \geq 98\%$
PTV	$D_{\max} \leq 110\%$
Heart	$D_{\max} \leq 100\%$
Heart	$D_{\text{mean}} \leq 9 \text{ Gy}$
Thyroid	ALARA*

Table 5-1 List of OAR and PTV dose constraints used for the VMAT optimization. All dose constraints are given in either percent of prescribed dose or in Gy. * The dose to the thyroid was lowered as much as possible without compromising other optimization objectives.

Because patients who received WLI have often received prior radiotherapy, there are no standard clinical dose constraints. As such the OAR dose constraints used in this study were based on those used for a generic patient. All plans were planned using the Eclipse treatment

planning system v.11 which employs AAA convolution algorithm with heterogeneity correction (v.11.0.31) and planned for a Varian TrueBeam linac commissioned for 6 MV flattened, 6 MV FFF and 10 MV FFF treatments.

The dose calculation method used for the dose assessment done in this study was the Monte Carlo code presented in Chapter 2. However, the addition of the leakage model was not used as the distance between the thyroid (the most distant organ evaluated) and PTV is small enough that its addition would not have affected the results.

5.2.2 Secondary Cancer Risk

Organ absolute dose is a useful measure because it is a well-established physical quantity. However, it can be hard to interpret clinically as it is not a direct predictor for the risk of complications. For clinical purposes, it can be useful to use risk models to transform physical dosimetric data into quantities that are more clinically relevant like excess absolute risk (EAR), which is defined as the absolute difference in risk between a baseline population and the irradiated population. In this study, the risk of SMN in breast and thyroid following WLI was compared using a linear risk model and three non-linear risk models developed by Schneider et al. [58] [59] for the induction of secondary carcinoma. The non-linear models are based on the assumption that the EAR is proportional to the organ equivalent dose (OED). OED is a quantity which is defined such that if 2 treatments deliver the same OED, the risk of SMN would be identical. The OED in all three models is given by Eq. 5-1 where V_{Total} is the total organ volume,

V_i is the volume receiving a dose D_i , R is a parameter accounting for repopulation and α is a parameter accounting for the effect of fractionation.

$$OED_{Full} = \frac{1}{V_{Total}} \sum_i V_i D_i \frac{e^{-\alpha D_i}}{\alpha R} \left(1 - 2R + R^2 e^{\alpha D_i} - (1 - R)^2 e^{-\frac{\alpha R}{1-R} D_i} \right) \quad 5-1$$

The main difference between the three models is the value of the parameter R , the variable that quantifies the ability of cells to regenerate between fractions. In the first model, $R = 0$ which represents a model where there is no repair or repopulation (bell-shaped model). In the second model, R is found by fitting the mechanistic model of Eq. 5-1 to the incidence data obtained from Hodgkin's and atomic bomb survivors (full model). In the last model, $R = 1$ which represents a model with complete repair and repopulation of cells in between fractions (plateau model). For the bell shaped and plateau models, Eq 5-1 can be simplified to Eq. 5-2 and Eq 5-3 respectively.

$$OED_{B-S} = \frac{1}{V_{Total}} \sum_i V_i D_i e^{-\alpha D_i} \quad 5-2$$

$$OED_P = \frac{1}{V_{Total}} \sum_i V_i \frac{1 - e^{-\alpha D_i}}{\alpha} \quad 5-3$$

The values of the fitted parameters for each model are given in Table 5-2. All parameters were taken from Schneider et al. [58]. The thyroid specific parameters were not available for this model. Instead, the parameters for generic carcinomas were used to model the risk of second thyroid cancer. This approach was taken by Mazonakis et al. [60] and Cella et al. [61], although they limited their calculations to the bell-shaped model. Furthermore, it is important to note

that these parameters were not modelled for children but for a group of patients that included both children and adults.

Site	Mechanistic Model		Bell Shaped Model		Plateau Model	
	R	α	R	α	R	α
Thyroid	0.17	0.089	0	0.065	1	0.317
Breast	0.15	0.044	0	0.041	1	0.115

Table 5-2 Values of parameters used for the breasts and thyroid second cancer model.

Additionally, a linear model in which the OED is equal to the mean organ dose was used to assess relative risk of second cancer. This model was previously developed by Preston et al. [55] from the atomic bomb survivors data and used by Myers et al. [62] to estimate the risk of second malignancy after cranio-spinal irradiation. For all models, the fact that OED is proportional to EAR was used to derive Eq.5-4 which defines the risk ratio (RR_{12}) for radiation-induced cancer between treatment 1 and 2.

$$RR_{12} = \frac{EAR_1}{EAR_2} = \frac{OED_1}{OED_2} \quad 5-4$$

5.3 Results

5.3.1 Thyroid Dose and Risk of Secondary Malignancy

Both 6 MV FFF and 10 MV FFF beam energy plans significantly reduced doses received by the thyroid compared to the 6 MV flattened energy plan. The 6 MV FFF energy reduced the V_{1Gy} and V_{2Gy} by 11.6% (95% CI [7.7, 15.5]) and 2.5 (95% CI [1.4, 3.6]) respectively. The 10 MV FFF beam

energy reduced the V_{1Gy} and V_{2Gy} by 23.2% (95% CI [14.9, 31.5]) and 4.0% (95% CI [1.9, 6.1]) respectively. In addition, the 6 MV FFF and 10 MV FFF energy plans reduced the mean thyroid dose by 0.08 Gy (95% CI [0.01, 0.15]) and 0.29 Gy (95% CI [0.17, 0.41]) respectively compared to the 6 MV flattened beam. Figure 5-2 compares the spread in thyroid DVH for the three beam modalities. Table 5-3 gives dosimetric parameters for the different beam modalities. All significance values were calculated using a paired t-test. The calculated thyroid OED and mean doses for all patients are shown in Table 5-4. Risk ratios as calculated in Eq. 5-4 are shown in Table 5-5.

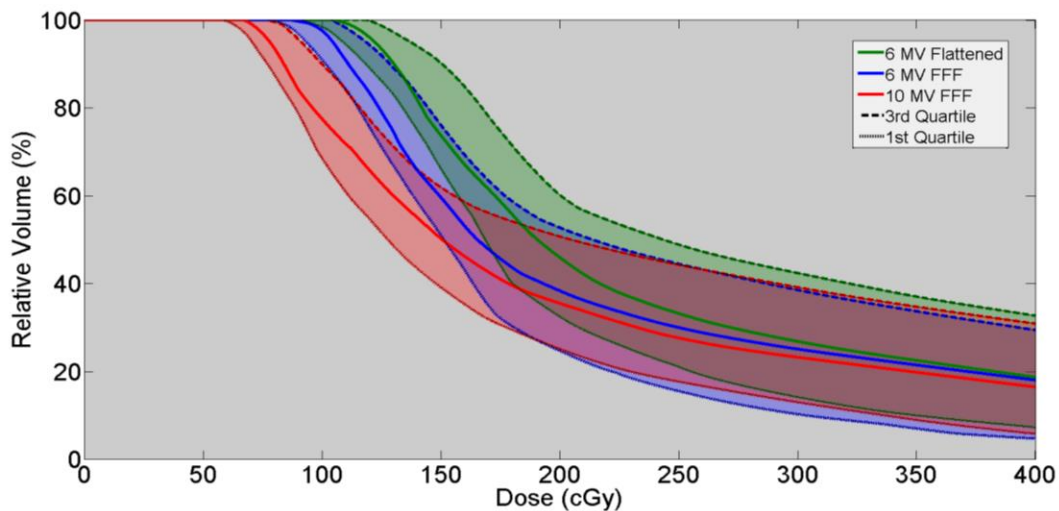


Figure 5-2 MC calculated thyroid DVH averaged over 10 patients for 6 MV Flattened, 6 MV FFF and 10 MV FFF beam energies. The shaded area shows the spread of DVHs in our datasets from the 25th percentile to the 75th percentile.

Dosimetric Properties	6 MV Flattened	6 MV FFF	10 MV FFF
D _{mean} (Gy)	2.7	2.6	2.4
V _{1Gy} (%)	83	72	60
V _{2Gy} (%)	41	39	37
V _{3Gy} (%)	28	28	26
V _{4Gy} (%)	20	20	19
V _{5Gy} (%)	15	16	15
V _{6Gy} (%)	12	13	11
V _{7Gy} (%)	10	10	9
V _{8Gy} (%)	7	7	6
V _{9Gy} (%)	4	5	3
V _{10Gy} (%)	2	2	1

Table 5-3 List of various thyroid specific dosimetric quantities averaged over 10 patients for each beam modality. Red bolded quantities are significantly ($p < 0.05$) different than their 6 MV flattened equivalent.

Patient No.	6 MV Flattened			6 MV FFF			10 MV FFF		
	OED _F	OED _{B-S}	OED _P	OED _F	OED _{B-S}	OED _P	OED _F	OED _{B-S}	OED _P
1	1.84	2.01	1.54	1.79	1.96	1.49	1.72	1.88	1.43
2	1.297	1.36	1.15	1.19	1.25	1.06	1.08	1.13	0.96
3	1.58	1.68	1.36	1.51	1.60	1.30	1.38	1.47	1.20
4	2.82	3.23	2.19	2.86	3.29	2.21	2.78	3.17	2.16
5	1.17	1.22	1.06	1.04	1.08	0.95	1.00	1.04	0.91
6	2.92	3.36	2.25	2.92	3.37	2.24	2.73	3.13	2.12
7	1.84	2.01	1.54	1.70	1.85	1.43	1.67	1.83	1.45
8	2.45	2.75	1.95	2.35	2.63	1.89	2.08	2.30	1.69
9	1.16	1.20	1.05	1.09	1.13	1.00	0.86	0.88	0.79
10	1.28	1.33	1.15	1.14	1.18	1.03	1.13	1.19	1.02
Mean	1.84	2.02	1.53	1.76	1.94	1.46	1.64	1.80	1.37

Table 5-4 Calculated thyroid OED in Gy for the full model (OED_F) (Eq. 5-1), bell shaped model (OED_{BS}) (Eq. 5-2) and plateau model (OED_P) (Eq. 5-3) for all patients and all modalities.

Patient No.	Linear Model		Full Model		Bell Shaped Model		Plateau Model	
	RR _{10MVFFF-6MV}	RR _{6MVFFF-6MV}						
1	0.94	0.99	0.93	0.97	0.93	0.97	0.92	0.97
2	0.83	0.92	0.83	0.92	0.83	0.92	0.84	0.92
3	0.88	0.96	0.88	0.95	0.88	0.95	0.88	0.95
4	0.97	1.04	0.99	1.01	0.98	1.02	0.98	1.01
5	0.84	0.87	0.85	0.89	0.85	0.88	0.86	0.90
6	0.93	1.03	0.94	1.00	0.93	1.00	0.94	0.99
7	0.93	0.92	0.91	0.92	0.91	0.92	0.94	0.93
8	0.81	0.94	0.85	0.96	0.84	0.96	0.86	0.97
9	0.72	0.95	0.74	0.94	0.74	0.94	0.75	0.94
10	0.90	0.88	0.89	0.89	0.89	0.89	0.89	0.90
Mean	0.88±0.05	0.95±0.05	0.88±0.05	0.95±0.03	0.88±0.05	0.95±0.03	0.89±0.05	0.95±0.03

Table 5-5 Calculated thyroid cancer risk ratios for all patients according to 4 risk models: The linear

model where OED = D_{mean} , the full model (Eq.5-1), the bell shaped model (Eq. 5-2) and the plateau model (Eq.

5-3). The error on the mean represents the 95% CI as calculated by a Student t-test.

In terms of secondary thyroid cancer risks, 6 MV FFF beams significantly reduced the risk according to all models used in this study. The risk ratio between 6 MV FFF and 6 MV flattened treatments was calculated to be 0.95 for all models. The 10 MV FFF beam also significantly reduced the risk of secondary thyroid cancer compared to 6 MV flattened with a calculated risk ratio lower than 0.88 (95% CI [0.83, 0.93]) for all models except the plateau model for which the risk ratio was 0.89 (95% CI [0.84, 0.94]).

5.3.2 Breast Dose and Risk of Secondary Malignancy

Because of the low number of female patients, it was not possible to compute significance values for doses or risk ratios. However, there was a trend ($p=0.1$) toward 10 MV FFF lowering

mean breast doses compared to 6 MV flattened. This can be seen in the Figure 5-3 which shows breast DVHs for the 4 female patients.

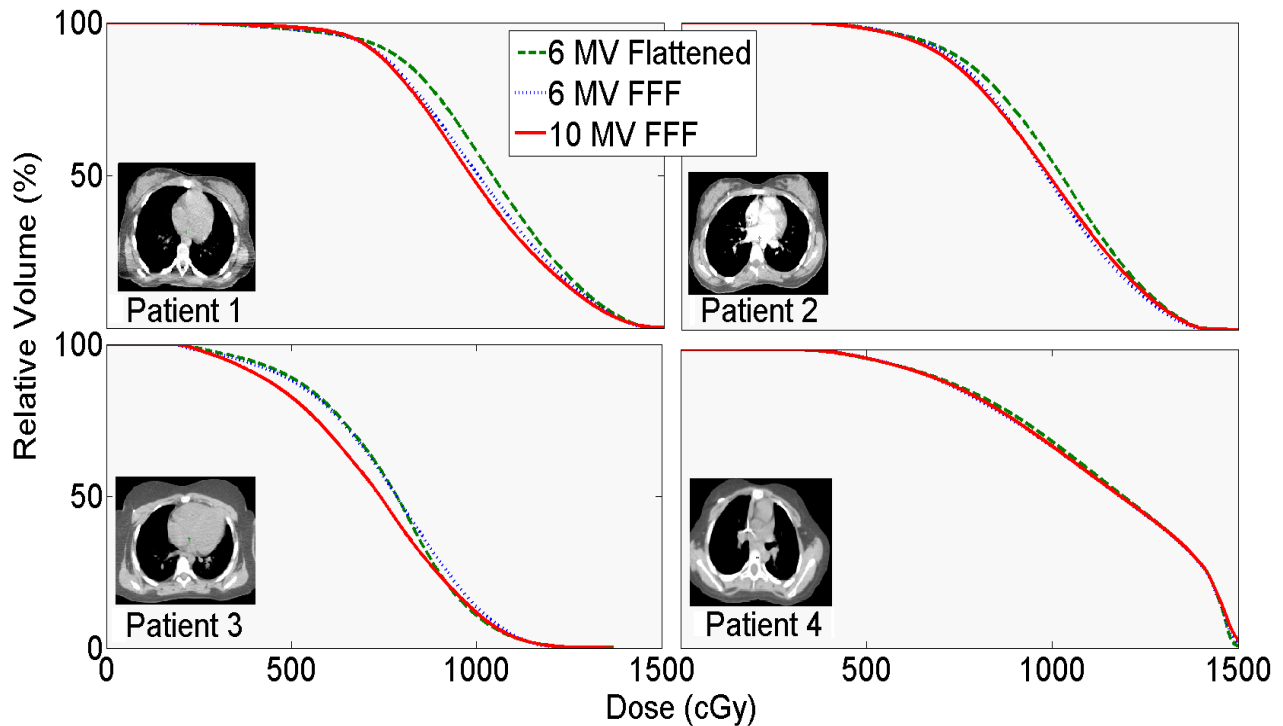


Figure 5-3 Breast DVH for all four female patients. The green dashed curve shows the 6 MV flattened DVH, the blue dotted curve shows the 6 MV FFF DVH and the red solid curve shows the 10 MV FFF DVH. An axial CT slice is also shown for each patient.

Various dosimetric quantities for all 4 female patients are shown in Table 5-6. There was also a trend ($p=0.06$) toward risk ratios below 1 for 10 MV FFF beams. OED as calculated by the linear, full mechanistic, bell shaped and plateau models are shown in Table 5-7 and the associated risk ratios are shown in Table 5-8.

	Patient 1			Patient 2			Patient 3			Patient 4		
	6MV	6MV FFF	10MV FFF	6MV	6MV FFF	10MV FFF	6MV	6MV FFF	10MV FFF	6 MV	6MV FFF	10MV FFF
D_{mean} (Gy)	10.3	10.0	9.9	10.1	9.8	9.8	7.6	7.7	7.3	11.4	11.3	11.3
$V_{3\text{Gy}}$	100	100	100	100	100	100	97	97	96	100	100	100
$V_{4\text{Gy}}$	99	99	99	99	100	99	94	93	90	99	99	99
$V_{5\text{Gy}}$	98	98	98	98	98	98	89	88	83	97	97	97
$V_{6\text{Gy}}$	96	96	97	96	96	95	80	79	71	94	94	94
$V_{7\text{Gy}}$	94	93	92	92	91	89	66	65	56	90	89	90
$V_{8\text{Gy}}$	87	82	81	84	81	79	46	47	39	85	83	84
$V_{9\text{Gy}}$	75	67	64	71	65	65	25	28	24	78	76	76
$V_{10\text{Gy}}$	57	50	46	54	47	48	11	13	12	69	67	68
$V_{11\text{Gy}}$	39	34	46	36	30	32	11	4	4	60	58	68
$V_{12\text{Gy}}$	23	20	31	19	16	18	3	0	1	50	49	58
$V_{13\text{Gy}}$	10	9	18	7	6	7	1	0	0	40	40	49

Table 5-6 List of various breast-specific dosimetric quantities for all four female patients who were planned with WLI in this study. The mean doses are given in cGy and the volumes in % of total volume

Patient No.	6 MV Flattened			6 MV FFF			10 MV FFF		
	OED _F	OED _{B-S}	OED _P	OED _F	OED _{B-S}	OED _P	OED _F	OED _{B-S}	OED _P
1	6.49	6.65	5.95	6.37	6.52	5.85	6.33	6.49	5.82
2	6.41	6.57	5.88	6.31	6.46	5.79	6.31	6.46	5.79
3	5.36	5.47	4.97	5.36	5.47	4.97	5.15	5.25	4.79
4	6.78	6.96	6.20	6.75	6.93	6.18	6.76	6.94	6.19
Mean	6.26	6.41	5.75	6.20	6.35	5.70	6.14	6.28	5.64

Table 5-7 Calculated breast OED in Gy for the full model (Eq. 5-1), bell shaped model (Eq. 5-2) and plateau model (Eq. 5-3) for all patients and all modalities.

Patient No.	Linear Model		Full Model		Bell Shaped Model		Plateau Model	
	RR _{10MVFFF-6MV}	RR _{6MVFFF-6MV}						
1	1.00	0.99	0.98	0.98	0.98	0.98	0.98	0.98
2	0.95	1.00	0.98	0.98	0.98	0.98	0.98	0.98
3	0.97	0.97	0.96	1.00	0.96	1.00	0.96	1.00
4	0.96	0.97	1.00	1.00	1.00	1.00	1.00	1.00
Mean	0.97	0.98	0.98	0.99	0.98	0.99	0.98	0.99

Table 5-8 Calculated breast cancer risk ratios for all patients according to 4 risk models models: The linear model

where $OED = D_{mean}$, the full model (Eq.5-1), the bell shaped model (Eq. 5-2) and the plateau model (Eq. 5-3).

5.4 Discussion

Thyroid and breast doses, plus cancer induction risk from WLI treatments with 6 MV FFF and 10 MV FFF were compared to those from 6 MV flattened beams. Thyroid doses were found to be significantly lowered in FFF beams compared to 6 MV flattened beams. 6 MV FFF and 10 MV FFF significantly reduced the thyroid volume that received more than 1 Gy by 11.6% (95% CI [7.7, 15.5]) and 23.2% (95% CI [14.9, 31.5]) respectively and the volume that received more than 2 Gy by 2.5 (95% CI [1.4, 3.6]) and 4.0% (95% CI [1.9, 6.1]) respectively. A mean thyroid dose reduction of 0.29 Gy (95% CI [0.17, 0.41]) was also observed in 10 MV FFF beams compared to 6 MV flattened beams. The dose reduction is higher in the lower dose regions of the DVH curve, which is predicted as FFF beams primarily reduce peripheral doses. Three non-linear models developed by Schneider et al. [63] and a linear model were used to predict the radiation-induced thyroid cancer risk ratio between FFF and flattened modalities. The three non-linear models all predicted similar risk ratios. For 10 MV FFF compared to 6 MV flattened, the full mechanistic and bell-shaped model predicted a risk ratio of 0.88 (95% CI [0.83, 0.93])

and the plateau model predicted a risk ratio of (0.89 (95% CI [0.84, 0.94])). For 6 MV FFF compared to 6 MV flattened, all three non-linear model predicted the same risk ratio of 0.95 (95% CI [0.92, 0.98]). The linear model predicted a risk ratio of 0.88 (95% CI [0.83, 0.93]) in favor of 10 MV FFF but found no significant difference between the 6 MV flattened and unflattened beams. The models used to calculate the risk of radiation-induced thyroid cancer made use of parameters fitted to a general carcinoma model. This had to be done since data from the Hodgkin lymphoma and atomic bomb survivors could not be fitted with a thyroid specific risk model [58]. However, it is unlikely that this assumption impacted our results as the general carcinoma model agreed with the linear model which simply assumes that risk is linear with mean dose and does not depend on any fitted parameter. The agreement between the linear and non-linear model is likely to be due to the fact that mean thyroid doses are low (mean thyroid dose \sim 2.5 Gy) in patients treated with WLI. It is generally agreed that at low doses, the risk of second cancer is proportional to dose [60] and as such all three non-linear models predict a linear risk increase at low doses. The effect of sex on thyroid dose was not considered in this study but it would be of interest to pursue this in future research.

While the number of female patients in our cohort was too small to be able to extract useful statistics, there seems to be a trend ($p=0.1$) to lower mean breast doses during WLI with 10 MV FFF compared to 6 MV flattened. This can be seen in Figure 5-3 where the breast DVHs for all four female patients in this cohort are shown. 10 MV FFF lead to a mean breast dose reduction for all patients (42 cGy for patient 1, 26 cGy for patient 2, 37 cGy for patient 3, and 5 cGy for

patient 4). The same models used to determine the risk of radiation-induced thyroid cancers were used to calculate the risk of secondary breast cancer in these 4 patients. The parameters of the non-linear breast cancer models were obtained from a fit of breast cancer risk in Hodgkin and atomic bomb survivors. All models predicted that both FFF beams would lower the secondary cancer risk by a few percentage points. However, due to the low number of patients, the data is not statistically significant ($p=0.06$) and further investigation with a larger patient cohort is necessary to determine if there is a measurable difference.

Overall, there seems to be benefits to using FFF beams, and specifically 10 MV FFF, in terms of lowering the risk of late complications following WLI. Both FFF beams have been shown to reduce the risk of radiotherapy induced thyroid cancer after WLI. Furthermore, 10 MV FFF seems to have the effect of reducing mean doses to both breast tissue and the thyroid which could reduce the risks of other long term toxicity associated with low doses to these organs.

5.5 Conclusion

Paediatric patients receiving WLI would benefit from being treated with FFF beams in conjunction with increasing the beam energy from 6 MV to 10 MV. 10 MV FFF beams reduced the mean dose to the thyroid by 0.29 Gy (95% CI [0.17, 0.41]) or 11% of the mean thyroid dose delivered by the 6 MV flattened beam. This reduction in thyroid dose can be associated with a lower risk of second thyroid cancer. The risk ratio for radiation-induced thyroid cancer between 10 MV FFF and 6 MV flattened was 0.88 (95% CI [0.83, 0.93]). Similarly, 6 MV FFF was also

associated with a lower risk of thyroid cancer compared to 6 MV flattened, although in the case of the linear risk model, the difference was not significant. The risk ratio between 6 MV FFF and 6 MV flattened was 0.95 (95% CI [0.92, 0.98]) for the three non-linear models. While the number of female patients in this study was small, a trend towards 10 MV FFF delivering lower doses than the 6 MV flattened beam was seen. Overall, using 10 MV FFF could reduce the risk of radiation-induced cancers and other late complications such as thyroid dysfunction and breast hypoplasia in paediatric patients receiving WLI.

Chapter 6

Conclusion and Future Work

6.1 Conclusion

This thesis aimed at assessing and comparing peripheral doses and radiotherapy-induced cancer risk associated with the different beam modes commonly available on medical linacs. A VMAT technique was studied using 6 MV flattened, 6 MV FFF and 10 MV FFF beam modes. A Monte Carlo model of a Varian TrueBeam medical linear accelerator was validated for in-field and out-of-field (peripheral) photon doses. Leakage correction factors were measured and applied to the Monte Carlo dose model to compensate for linac treatment head leakage and scatter not included in the simulations. Before this thesis was presented, radiotherapy delivery with a 6 MV flattened beam energy was the standard of care for treating all paediatric VMAT plans at BC Cancer - Vancouver. The 6 MV FFF and 10 MV FFF beam modes were mainly used for advanced, hypofractionated stereotactic treatments, as the much higher dose rates achievable with FFF beams significantly reduce the VMAT arc delivery treatment time required (e.g. from 8 min to 2 min). While several papers have reported results indicating that 10 MV FFF beam would be advantageous in terms of reducing peripheral dose, there was a lack of patient-specific dosimetric data, especially for VMAT treatments. The data presented in this thesis can be used to guide the clinical decision making process with respect to paediatric radiotherapy planning. As of January, 2019 a change in practice was introduced at BC Cancer- Vancouver

radiotherapy department; all paediatric patients will be treated with FFF beams (preferably 10 MV FFF).

A model of peripheral dose using a combination of MC simulations and measurements in-phantom was built and is presented in Chapter 2 of this thesis. This model was purposefully built to allow for the collecting of patient specific dosimetric data. The accuracy of this model was validated and good agreement was shown between the model and measurements. This model was subsequently used in a retrospective dosimetric study of 26 paediatric patients comparing the peripheral dose delivered by 6 MV flattened, 6 MV FFF and 10 MV FFF beam modes. It was shown that significant advantages could be obtained with the use of FFF beams. A peripheral dose reduction of 10 to 26% was found in 10 MV FFF compared to 6 MV flattened. 6 MV FFF also lowered peripheral doses compared to the flattened 6 MV beam, but not to the same extent as the 10 MV FFF beam. Additionally, neutron doses were measured, as a common concern amongst clinicians is the higher neutron doses associated with 10 MV beams compared to 6 MV beams. It was found that the neutron doses accounted for a negligible amount (<1%) of the total peripheral dose. The dosimetric analysis of clinical treatment plans is presented in Chapter 4 of this thesis.

The effect of the peripheral dose reduction from FFF beams on the thyroid and breast doses received by paediatric patients treated with Whole Lung Irradiation (WLI) was investigated and presents concrete data showing the clinical relevance of the work presented in this thesis. The

dosimetric data was obtained using the MC model presented in Chapter 2 without the addition of the leakage correction. This was done as both the thyroid and breasts are within 10 cm of the PTV which is close enough to ensure that the MC only dose distributions are accurate. Risk ratios were computed using four different risk models: a linear model, a bell shape model, a plateau model and a mechanistic model. Agreeing with the results of Chapter 4, it was found that 6 MV FFF and 10 MV FFF reduced the peripheral dose received by the thyroid. This translated into a secondary thyroid cancer risk ratio of 0.95 and 0.88 respectively compared to the 6 MV flattened beams. Breast dose also was reduced in 10 MV FFF treatments compared to treatments using 6 MV flattened beams.

This thesis brings clear evidence that peripheral doses can be reduced in patients with the use of the 10 MV FFF beam mode compared to the flattened 6 MV beam. The 6 MV FFF beam mode also reduces peripheral doses but not to the same extent as 10 MV FFF. The mixed MC and measurement model allowed for complete and accurate patient-specific dosimetric data to be obtained. This data shows that there are no indications that clinical parameters such as PTV size and treatment location are associated with different peripheral dose reductions. This suggests that all paediatric patients are likely to benefit from the use of FFF beams. These results, which were obtained in a study that analysed patient-specific dosimetric data, have influenced the care team at BC Cancer - Vancouver and the FFF beams are now routinely used to treat paediatric patients. The work on WLI presented in Chapter 5 shows the impact of this dose reduction on radiation induced cancer risk and provides more reasons for the clinical implementation of 10 MV FFF.

One of the main limitations of the work presented in this study is that it will be very difficult to measure the long-term clinical impact of a shift in radiotherapy treatment practice on the incidence and severity of late side effects. As such, a quantification of the impact can only be estimated based on the current risk models for late side effects which are not without uncertainties. Furthermore, it is unclear whether clinically significant results such as the ones presented in Chapter 5 can be replicated to other treatment sites.

6.2 Future Work

With the improvement in cancer survival rates and life expectancy of previously treated patients, addressing radiation-induced second cancers will become increasingly important. There is still much work that needs to be done to determine how we can lower that risk as much as possible. The work done in this thesis has opened the door to modelling patient specific risk of SMN for various treatment sites and it would be interesting to see what benefits if any can be gained with 10 MV FFF radiotherapy beam modes. It would also be of interest to develop techniques that specifically address the problem of peripheral dose. One such technique that has been a competing technology in the field of radiotherapy is the use of proton beams. These beams deliver dose distributions that are very conformal and have very low exit doses. However, the persisting uncertainty about the radiobiological effects of protons and of the neutron fields associated with proton accelerators makes it difficult to gauge the effect of protons beams on the incidence of radiotherapy-induced second malignant

neoplasms. Furthermore, proton accelerators are still very costly and relatively few (none in Canada) are currently in use compared to medical electron particle accelerators (conventional linacs). As such it is important to continue developing means of reducing the risk of radiotherapy-induced second cancer for the medical linacs currently available in cancer centers across the world.

References

- [1] S. Tyldesley, G. Delaney, F. Foroudi, L. Barbera, M. Kerba and W. Mackillop, "Estimating the Need for Radiotherapy for Patients with Prostate, Breast, and Lung Cancers: Verification of Model Estimates of Need with Radiotherapy Utilization Data from British Columbia," *International Journal of Radiation Oncology Biology Physics*, vol. 79, no. 5, pp. 1507-1515, APR 1 2011.
- [2] G. M. Jaffray DA, "Radiation Therapy for Cancer," in *Cancer: Disease Control Priorities, Third Edition (Volume 3)*, Washington (DC), World Bank, 2015.
- [3] R. Shaffer, E. Vollans, R. Vellani, M. Welsh, V. Moiseenko and K. Goddard, "A Radiotherapy Planning Study of RapidArc, Intensity Modulated Radiotherapy, Three-Dimensional Conformal Radiotherapy, and Parallel Opposed Beams in the Treatment of Pediatric Retroperitoneal Tumors," *Pediatric Blood & Cancer*, vol. 56, no. 1, pp. 16-23, JAN 2011.
- [4] M. M. Hudson, K. K. Ness, J. G. Gurney, D. A. Mulrooney, W. Chemaitilly, K. R. Krull, D. M. Green, G. T. Armstrong, K. A. Nottage, K. E. Jones, C. A. Sklar, D. Kumar and L. L. Robison, "Clinical Ascertainment of Health Outcomes Among Adults Treated for Childhood Cancer," *Jama-Journal of the American Medical Association*, vol. 309, no. 22, pp. 2371-2381, JUN 12 2013.
- [5] P. D. Inskip and R. E. Curtis, "New malignancies following childhood cancer in the United

- States, 1973-2002," *International Journal of Cancer*, vol. 121, no. 10, pp. 2233-2240, NOV 15 2007.
- [6] M. M. Fidler, R. C. Reulen, D. L. Winter, J. Kelly, H. C. Jenkinson, R. Skinner, C. Frobisher, M. M. Hawkins and B. Childhood, "Long term cause specific mortality among 34489 five year survivors of childhood cancer in Great Britain: population based cohort study," *Bmj-British Medical Journal*, vol. 354, p. i4351, SEP 1 2016.
- [7] R. W. Harbron, R. G. Feltbower, A. Glaser, J. Lilley and M. S. Pearce, "Secondary Malignant Neoplasms Following Radiotherapy for Primary Cancer in Children and Young Adults," *Pediatric hematology and oncology*, vol. 31, no. 3, pp. 259-267, APR 2014.
- [8] R. M. Howell, S. B. Scarboro, S. F and D. Z. Yaldo, "Accuracy of out-of-field dose calculations by a commercial treatment planning system," *Physics in Medicine and Biology*, vol. 55, no. 23, pp. 6999-7008, DEC 7 2010.
- [9] J. Y. Huang, D. S. Followill, X. A. Wang and S. F. Kry, "Accuracy and sources of error of out-of field dose calculations by a commercial treatment planning system for intensity-modulated radiation therapy treatments," *Journal of Applied Clinical Medical Physics*, vol. 14, no. 2, pp. 186-197, 2013.
- [10] S. M. Seltzer, D. T. Bartlett, D. T. Burns, G. Dietze, H.-G. Menzel, H. G. Paretzke and A. Wambersie, "Report 85: Fundamental quantities and units for ionizing radiation.," *Journal of the ICRU*, vol. 11, no. 1, pp. 1-31.
- [11] W. Cho, K. N. Kielar, E. Mok, L. Xing, J.-H. Park, W.-G. Jung and T.-S. Suh, "Multisource

- modeling of flattening filter free (FFF) beam and the optimization of model parameters," *Medical physics*, vol. 38, no. 4, pp. 1931-1942, 04 2011.
- [12] O. Vassiliev, U. Titt, S. Kry, F. Ponisch, M. Gillin and R. Mohan, "Monte Carlo study of photon fields from a flattening filter-free clinical accelerator," *Medical physics*, vol. 33, no. 4, pp. 820-827, APR 2006.
- [13] P. Almond, P. Biggs, B. Coursey, W. Hanson, M. Huq, R. Nath and D. Rogers, "AAPM's TG-51 protocol for clinical reference dosimetry of high-energy photon and electron beams," *Medical physics*, vol. 26, no. 9, pp. 1847-1870, SEP 1999.
- [14] "ICRU Report 83: Prescribing, Recording, and Reporting Photon-Beam Intensity-Modulated Radiotherapy," *Journal of the ICRU*, vol. 10, no. 1, pp. NP-NP, 04/01 2010.
- [15] W. Bar, M. Schwarz, M. Alber, L. Bos, B. Mijnheer, C. Rasch, C. Schneider, F. Nusslin and E. Damen, "A comparison of forward and inverse treatment planning for intensity-modulated radiotherapy of head and neck cancer," *Radiotherapy and Oncology*, vol. 69, no. 3, pp. 251-258, DEC 2003.
- [16] F. Pajonk, E. Vlashi and W. H. McBride, "Radiation Resistance of Cancer Stem Cells: The 4 R's of Radiobiology Revisited," *Stem cells*, vol. 28, no. 4, pp. 639-648, APR 2010.
- [17] S. Rockwell, I. T. Dobrucki, E. Y. Kim, S. Tucker Marrison and V. Thuc, "Hypoxia and Radiation Therapy: Past History, Ongoing Research, and Future Promise," *Current Molecular Medicine*, vol. 9, no. 4, pp. 442-458, MAY 2009.
- [18] Y. Xiao, S. F. Kry, R. Popple, E. Yorke, N. Papanikolaou, S. Stathakis, P. Xia, S. Huq, J.

- Bayouth, J. Galvin and F.-F. Yin, "Flattening filter-free accelerators: a report from the AAPM Therapy Emerging Technology Assessment Work Group," *Journal of Applied Clinical Medical Physics*, vol. 16, no. 3, pp. 12-29, 2015.
- [19] J. Cashmore, M. Ramtohul and D. Ford, "Lowering Whole-Body Radiation Doses in Pediatric Intensity-Modulated Radiotherapy through the use of Unflattened Photon Beams," *International Journal of Radiation Oncology Biology Physics*, vol. 80, no. 4, pp. 1220-1227, JUL 15 2011.
- [20] R. A. Haelg, J. Besserer and U. Schneider, "Systematic measurements of whole-body dose distributions for various treatment machines and delivery techniques in radiation therapy," *Medical physics*, vol. 39, no. 12, pp. 7662-7676, DEC 2012.
- [21] S. F. Kry, O. N. Vassiliev and R. Mohan, "Out-of-field photon dose following removal of the flattening filter from a medical accelerator," *Physics in Medicine and Biology*, vol. 55, no. 8, pp. 2155-2166, APR 21 2010.
- [22] A. Mesbahi, "Dosimetric characteristics of unflattened 6 MV photon beams of a clinical linear accelerator: A Monte Carlo study," *Applied Radiation and Isotopes*, vol. 65, no. 9, pp. 1029-1036, SEP 2007.
- [23] J. Bordy, I. Bessieres, E. d'Agostino, C. Domingo, F. d'Errico, A. di Fulvio, Z. Knezevic, S. Miljanic, P. Olko, A. Ostrowsky, B. Poumarede, S. Sorel, L. Stolarczyk and D. Vermesse, "Radiotherapy out-of-field dosimetry: Experimental and computational results for photons in a water tank," *Radiation Measurements*, vol. 57, pp. 29-34, OCT 2013.

- [24] S. Kry, M. Salehpour, D. Followill, M. Stovall, D. Kuban, R. White and I. Rosen, "Out-of-field photon and neutron dose equivalents from step-and-shoot intensity-modulated radiation therapy," *International Journal of Radiation Oncology Biology Physics*, vol. 62, no. 4, pp. 1204-1216, JUL 15 2005.
- [25] A. Naseri and A. Mesbahi, "A review on photoneutrons characteristics in radiation therapy with high-energy photon beams", " *Reports of Practical Oncology & Radiotherapy*", vol. "15", no. "5", pp. "138 - 144", "2010".
- [26] S. F. Kry, U. Titt, F. Poenisch, O. N. Vassiliev, M. Salehpour, M. Gillin and R. Mohan, "Reduced neutron production through use of a flattening-filter-free accelerator," *International Journal of Radiation Oncology Biology Physics*, vol. 68, no. 4, pp. 1260-1264, JUL 15 2007.
- [27] M. Najem, F. Abolaban, Z. Podolyak and M. Spyrou, "Neutron production from flattening filter free high energy medical linac: A Monte Carlo study," *Radiation Physics and Chemistry*, vol. 116, pp. 176-180, NOV 2015.
- [28] R. M. Howell, S. F. Kry, E. Burgett, N. E. Hertel and D. S. Followill, "Secondary neutron spectra from modern Varian, Siemens, and Elekta linacs with multileaf collimators," *Medical physics*, vol. 36, no. 9, pp. 4027-4038, SEP 2009.
- [29] W.-Z. Chen, Y. Xiao and J. Li, "Impact of dose calculation algorithm on radiation therapy," *World journal of radiology*, vol. 6, pp. 874-880, 11 2014.
- [30] T. Teke, "Monte Carlo techniques for patient specific verification of complex radiation

- therapy treatments including TBI, VMAT and SBRT lung," *University Of British Columbia*, 2012.
- [31] I. Kawrakow, E. Mainegra-Hing, D. Rogers, F. Tessier and B. Walters, "NRCC Report PIRS-701: The EGSnrc code system: Monte Carlo simulation of electron and photon transport," 2018.
- [32] D. W. O. Rogers, B. A. Faddegon, G. X. Ding, C. Ma, J. We and T. R. Mackie, "BEAM: A Monte Carlo code to simulate radiotherapy treatment units," *Medical physics*, vol. 22, no. 5, pp. 503-524, 1995.
- [33] M. Constantin, J. Perl, T. LoSasso, A. Salop, D. Whittum, A. Narula, M. Svatos and P. J. Keall, "Modeling the TrueBeam linac using a CAD to Geant4 geometry implementation: Dose and IAEA-compliant phase space calculations," *Medical physics*, vol. 38, no. 7, pp. 4018-4024, 2011.
- [34] J. Lobo and I. Antoniu Popescu, "Two new DOSXYZnrc sources for 4D Monte Carlo simulations of continuously variable beam configurations, with applications to RapidArc, VMAT, TomoTherapy and CyberKnife," *Physics in Medicine and Biology*, vol. 55, no. 16, pp. 4431-4443, AUG 21 2010.
- [35] I. Popescu, C. Shaw, S. Zavgorodni and W. Beckham, "Absolute dose calculations for Monte Carlo simulations of radiotherapy beams," *Physics in Medicine and Biology*, vol. 50, no. 14, pp. 3375-3392, JUL 21 2005.
- [36] A. M. Bergman, E. Gete, C. Duzenli and T. Teke, "Monte Carlo modeling of HD120 multileaf

- collimator on Varian TrueBeam linear accelerator for verification of 6X and 6X FFF VMAT SABR treatment plans," *Journal of Applied Clinical Medical Physics*, vol. 15, no. 3, pp. 148-163, 2014.
- [37] E. Gete, C. Duzenli, M.-P. Milette, A. Mestrovic, D. Hyde, A. Mary and T. Teke, "A Monte Carlo approach to validation of FFF VMAT treatment plans for the TrueBeam linac," *Medical physics*, vol. 40, no. 2, p. 021707, FEB 2013.
- [38] T. Teke, C. Duzenli, A. Bergman, F. Viel, P. Atwal and E. Gete, "Monte Carlo validation of the TrueBeam 10XFFF phase-space files for applications in lung SABR," *Medical physics*, vol. 42, no. 12, pp. 6863-6874, DEC 2015.
- [39] S. F. Kry, U. Titt, F. Ponisch, D. Followill, O. N. Vassiliev, R. Allen White, R. Mohan and M. Salehpour, "A Monte Carlo model for calculating out-of-field dose from a Varian 6 MV beam," *Medical physics*, vol. 33, no. 11, pp. 4405-4413, NOV 2006.
- [40] I. Diallo, N. Haddy, E. Adjadj, A. Samand, E. Quiniou, J. Chavaudra, I. Alziar, N. Perret, S. Guerin, D. Lefkopoulos and F. de, "Frequency Distribution of Second Solid Cancer Locations in Relation to the Irradiated Volume among 115 Patients Treated for Childhood Cancer," *International Journal of Radiation Oncology Biology Physics*, vol. 74, no. 3, pp. 876-883, JUL 1 2009.
- [41] W. Dorr and T. Herrmann, "Cancer induction by radiotherapy: dose dependence and spatial relationship to irradiated volume.," *Journal of radiological protection : official journal of the Society for Radiological Protection*, vol. 22, no. 3A, pp. A117-21, 2002 Sep 2002.

- [42] L. J. Murray, C. M. Thompson, J. Lilley, V. Cosgrove, K. Franks, D. Sebag-Montefiore and A. M. Henry, "Radiation-induced second primary cancer risks from modern external beam radiotherapy for early prostate cancer: impact of stereotactic ablative radiotherapy (SABR), volumetric modulated arc therapy (VMAT) and flattening filter free (FFF) radiotherapy," *Physics in Medicine and Biology*, vol. 60, no. 3, pp. 1237-1257, FEB 7 2015.
- [43] B. Dobler, J. Maier, B. Knott, M. Maerz, R. Loeschel and O. Koelbl, "Second Cancer Risk after simultaneous integrated boost radiation therapy of right sided breast cancer with and without flattening filter," *Strahlentherapie Und Onkologie*, vol. 192, no. 10, pp. 687-695, OCT 2016.
- [44] L. B. Marks, E. D. Yorke, A. Jackson, R. K. Ten Haken, L. S. Constine, A. Eisbruch, S. M. Bentzen, J. Nam and J. O. Deasy, "Use of Normal Tissue Complication Probability Models in the Clinic," *International Journal of Radiation Oncology Biology Physics*, vol. 76, no. 3, pp. S10-S19, 2010.
- [45] S. F. Kry, B. Bednarz, R. M. Howell, L. Dauer, D. Followill, E. Klein, H. Paganetti, B. Wang, C.-S. Wu and X. George Xu, "AAPM TG 158: Measurement and calculation of doses outside the treated volume from external-beam radiation therapy," *Medical physics*, vol. 44, no. 10, pp. e391-e429, OCT 2017.
- [46] A. Berrington, E. Gilbert, R. Curtis, P. Inskip, R. Kleinerman, L. Morton, P. Rajaraman and M. P. Little, "Second Solid Cancers After Radiation Therapy: A Systematic Review of the Epidemiologic Studies of the Radiation Dose-Response Relationship," *International Journal*

of Radiation Oncology Biology Physics, vol. 86, no. 2, pp. 224-233, JUN 1 2013.

- [47] S. F. Kry, D. Followill, R. Allen White, M. Stovall, D. A. Kuban and M. Salehpour, "Uncertainty of calculated risk estimates for secondary malignancies after radiotherapy," *International Journal of Radiation Oncology Biology Physics*, vol. 68, no. 4, pp. 1265-1271, JUL 15 2007.
- [48] R. Benoist, J. Lemerle, R. Jean, P. Rufin, P. Scheinmann and J. Paupe, "Effects of pulmonary function of whole lung irradiation for Wilm's tumour in children," *Thorax*, vol. 37, no. 3, pp. 175-180, 03 1982.
- [49] S. L. Spunt, M. B. L. E. Kun, C. A. Poquette, A. M. Cain, L. Brandao and A. S. Pappo, "Selective Use of Whole-Lung Irradiation for Patients With Ewing Sarcoma Family Tumors and Pulmonary Metastases at the Time of Diagnosis," *Journal of Pediatric Hematology/Oncology*, vol. 23, no. 2, 2001.
- [50] S. Skamene, S. Abish, D. Mitchell and C. Freeman, "Radiotherapy is Important for Local Control at Primary and Metastatic Sites in Pediatric Rhabdomyosarcoma," *Cureus*, vol. 7, no. 11, pp. e388; e388-e388, 11/23 2015.
- [51] S. Scobioala, A. Ranft, H. Wolters, S. Jabar, M. Paulussen, B. Timmermann, H. Juergens, W. Hassenpflug, T. Klingebiel, K. Elsayad, H. Theodor and U. Dirksen, "Impact of Whole Lung Irradiation on Survival Outcome in Patients With Lung Relapsed Ewing Sarcoma," *International Journal of Radiation Oncology Biology Physics*, vol. 102, no. 3, pp. 584-592, NOV 1 2018.

- [52] J. P. Ginsberg, P. Goodman, W. Leisenring, K. K. Ness, P. A. Meyers, S. L. Wolden, S. M. Smith, M. Stovall, S. Hammond, L. L. Robison and K. C. Oeffinger, "Long-term survivors of childhood Ewing sarcoma: report from the childhood cancer survivor study," *Journal of the National Cancer Institute*, vol. 102, no. 16, pp. 1272-1283, 08/18 2010.
- [53] C. Furst, M. Lundell, S. Ahlback and L. Holm, "Breast Hypoplasia Following Irradiation of the Female Breast in Infancy and Early-Childhood," *Acta Oncologica*, vol. 28, no. 4, pp. 519-523, 1989.
- [54] T. M. Morgan, H. Danish, R. H. Nanda, N. Esiashvili and L. R. Meacham, "Whole lung irradiation in stage IV Wilms tumor patients: Thyroid dosimetry and outcomes," *Pediatric Blood & Cancer*, vol. 65, no. 2, p. e26843, FEB 2018.
- [55] D. Preston, E. Ron, S. Tokuoka, S. Funamoto, N. Nishi, M. Soda, K. Mabuchi and K. Kodama, "Solid cancer incidence in atomic bomb survivors: 1958-1998," *Radiation research*, vol. 168, no. 1, pp. 1-64, JUL 2007.
- [56] A. T. Meadows, D. L. Friedman, J. P. Neglia, A. C. Mertens, S. S. Donaldson, M. Stovall, S. Hammond, Y. Yasui and P. D. Inskip, "Second Neoplasms in Survivors of Childhood Cancer: Findings From the Childhood Cancer Survivor Study Cohort," *Journal of Clinical Oncology*, vol. 27, no. 14, pp. 2356-2362, MAY 10 2009.
- [57] B. A. Jereczek-Fossa, D. Alterio, J. Jassem, B. Gibelli, N. Tradati and R. Orecchia, "Radiotherapy-induced thyroid disorders," *Cancer Treatment Reviews*, vol. 30, no. 4, pp. 369-384, June 2004 2004.

- [58] U. Schneider, M. Sumila and J. Robotka, "Site-specific dose-response relationships for cancer induction from the combined Japanese A-bomb and Hodgkin cohorts for doses relevant to radiotherapy," *Theoretical Biology and Medical Modelling*, vol. 8, p. 27, JUL 26 2011.
- [59] U. Schneider, "Mechanistic model of radiation-induced cancer after fractionated radiotherapy using the linear-quadratic formula," *Medical Physics*, vol. 36, no. 4, pp. 1138-1143, APR 2009.
- [60] M. Mazonakis, A. Tzedakis, E. Lyraraki and J. Damilakis, "Radiation dose and cancer risk to out-of-field and partially in-field organs from radiotherapy for symptomatic vertebral hemangiomas," *Medical physics*, vol. 43, no. 4, pp. 1841-1848, APR 2016.
- [61] L. Cella, M. Conson, M. Cristina, S. Molinelli, U. Schneider, V. Donato, R. Orecchia, M. Salvatore and R. Pacelli, "Hodgkin's lymphoma emerging radiation treatment techniques: trade-offs between late radio-induced toxicities and secondary malignant neoplasms," *Radiation oncology (London, England)*, vol. 8, pp. 22-22, 01/30 2013.
- [62] P. Myers, P. Mavroidis, G. Komisopoulos, N. Papanikolaou and S. Stathakis, "Pediatric Cranio-spinal Axis Irradiation: Comparison of Radiation-induced Secondary Malignancy Estimations Based on Three Methods of Analysis for Three Different Treatment Modalities," *Technology in Cancer Research & Treatment*, vol. 14, no. 2, pp. 169-180, APR 2015.
- [63] U. Schneider, D. Zwahlen, D. Ross and B. Kaser-Hotz, "Estimation of radiation-induced

- cancer from three-dimensional dose distributions: Concept of organ equivalent dose," *International Journal of Radiation Oncology Biology Physics*, vol. 61, no. 5, pp. 1510-1515, APR 1 2005.
- [64] S. F. Kry, R. M. Howell, M. Salehpour and D. S. Followill, "Neutron spectra and dose equivalents calculated in tissue for high-energy radiation therapy," *Medical physics*, vol. 36, no. 4, pp. 1244-1250, APR 2009.
- [65] X. George Xu, B. Bednarz and H. Paganetti, "A review of dosimetry studies on external-beam radiation treatment with respect to second cancer induction," *Physics in Medicine and Biology*, vol. 53, no. 13, pp. R193-R241, JUL 7 2008.
- [66] K. Nottage, J. McFarlane, M. J. Krasin, C. Li, D. Srivastava, L. L. Robison and M. M. Hudson, "Secondary Colorectal Carcinoma After Childhood Cancer," *Journal of Clinical Oncology*, vol. 30, no. 20, pp. 2552-2558, JUL 10 2012.
- [67] S. Miljanic, J.-M. Bordy, F. d'Errico, R. Harrison and P. Olko, "Out-of-field dose measurements in radiotherapy - An overview of activity of EURADOS Working Group 9: Radiation protection in medicine," *Radiation Measurements*, vol. 71, pp. 270-275, DEC 2014.